ALLELE-SPECIFIC SIRNA CORRECTS ABERRANT CELLULAR PHENOTYPE IN KERATITIS-ICHTHYOSIS-DEAFNESS SYNDROME KERATINOCYTES

Ming Yang Lee[1], Hong-Zhan Wang[2], Thomas W. White[2], Tony Brooks[3], Alan Pittman[6,7], Heerni Halai[1], Anastasia Petrova[1], Diane Xu[1], Stephen L. Hart[4], Veronica A. Kinsler[4,5] and Wei-Li Di[1]

ORCiD:

Ming Yang Lee: 0000-0003-3135-3928

Hong-Zhan Wang: 0000-0002-3371-2309

Thomas W. White: 0000-0002-3285-7434

Tony Brooks: 0000-0002-3494-3045

Alan Pittman: 0000-0002-8112-2987

Heerni Halai: 0000-0003-1798-4600

Anastasia Petrova: 0000-0001-5294-399X

Diane Xu 0000-0002-1153-0352

Stephan L. Hart: 0000-0001-8254-376X

Veronica A. Kinsler: 0000-0001-6256-327X

Wei-Li Di: 0000-0002-4851-1649

1. Infection, Immunity and Inflammation Programme/Immunobiology Section, UCL Great Ormond Street Institute of Child Health, 30 Guilford St., London WC1N 1EH, United Kingdom
2. Department of Physiology and Biophysics, Basic Science Tower, T-5, Room 147, Stony Brook University, Stony Brook, NY, 11794-8661, USA

3. UCL Genomics, UCL Great Ormond Street Institute of Child Health, 30 Guilford St., London WC1N 1EH, United Kingdom
4. Department of Genetics and Genomic Medicine, UCL Great Ormond Street Institute of Child Health, 30 Guilford St., London WC1N 1EH, United Kingdom.
5. Paediatric Dermatology, Great Ormond Street Hospital for Children, London WC1N 3JH
6. Molecular Neuroscience, UCL Institute of Neurology, Queen Square, London WC1N 3BG, United Kingdom
7. Genetics Research Centre, St George's, University of London, Cranmer Terrace, London SW17 0RE, United Kingdom

Corresponding author:

Wei-Li Di

Infection, Immunity and Inflammation Programme/Immunobiology Section

UCL Great Ormond Street Institute of Child Health, 30 Guilford St., London WC1N 1EH, United Kingdom;

Tel: +44(0)2079052369;

email: w.di@ucl.ac.uk.

Short title:

Allele-specific siRNA for KID syndrome

Abbreviations:

KID: Keratitis-ichthyosis-deafness

KID-KC: KID syndrome patient-derived keratinocytes

control-KC: Healthy donor-derived keratinocytes

AS-siRNA: Allele-specific small interference RNA

SLDT: Scrape-loading dye transfer

RNA-Seq: RNA sequencing

GESS: Genome-wide enrichment of seed sequences

Author contributions:

	Study design	**Experiment conducting**	**Data collection**	**Data analysis**	**Patient management and ethics application**	**Paper writing**	**Paper commenting**
MYL		√	√	√		√	√
HZW		√	√	√			√
TWW	√	√	√	√			√
TB				√			√
AP[6,7]				√			
HH		√	√	√			
AP[1]		√					√
DX				√			
SLH	√						√
VAK	√				√	√	√
WLD	√	√	√	√		√	√

ABSTRACT

Keratitis-ichthyosis-deafness (KID) syndrome is a severe, untreatable condition characterized by ocular, auditory and cutaneous abnormalities, with major complications of infection and skin cancer. 86% of cases are caused by a heterozygous missense mutation (c.148G>A, p.D50N) in the *GJB2* gene, encoding gap junction protein connexin 26 (Cx26), which alters gating properties of Cx26 channels in a dominant manner. We hypothesized that a mutant-allele-specific siRNA (AS-siRNA) could rescue the cellular phenotype in patient keratinocytes. A KID syndrome cell line (KID-KC) was established from primary patient keratinocytes with a heterozygous p.D50N mutation. This displayed impaired gap junction communication and hyperactive hemichannels, confirmed by dye transfer, patch clamp and neurobiotin uptake assays. A human-murine chimeric skin graft model constructed with KID-KC mimicked patient skin *in vivo,* further confirming the validity of these cells as a model. *In vitro* treatment with AS-siRNA led to robust inhibition of the mutant *GJB2* allele without altering expression of the wildtype. This corrected both gap junction and hemichannel activity. Notably, AS-siRNA treatment caused only low-level off-target effects in KID-KC, as detected by genome-wide RNA sequencing. Our data provide an important proof-of-concept and model system for the potential use of AS-siRNA in treating KID syndrome, and other dominant genetic conditions.

INTRODUCTION

Keratitis-Ichthyosis-Deafness syndrome (KID syndrome, [MIM 148210]) is a rare, autosomal-dominant condition characterized by ocular and auditory impairment and hyperkeratotic skin lesions (Burns, 1915). Ocular involvement includes photophobia and neovascularization, progressively reducing visual acuity (Caceres-Rios et al., 1996), and auditory impairment features sensorineural hearing loss (Patel et al., 2015). Skin involvement consists of erythrokeratodermic or verrucous plaques, and palmoplantar keratoderma with alopecia and/or onychodystrophy (Caceres-Rios et al., 1996, Coggshall et al., 2013). Moreover, KID syndrome is frequently complicated with chronic, opportunistic cutaneous infection, resulting in failure to thrive and, in severe cases, septicemia (Coggshall et al., 2013). Patients are at increased risk of developing skin malignancies, particularly squamous cell carcinoma (Coggshall et al., 2013). These complications can have a significant impact on life expectancy. Current cutaneous treatment is limited to symptomatic management, including retinoids to attempt to improve the skin barrier, antifungal and antibacterial agents for infection control (Coggshall et al., 2013). There is an unmet need for targeted treatment of this condition.

The cause of KID syndrome was identified as heterozygous missense mutations in the *GJB2* gene (van Steensel et al., 2002, Richard et al., 2002), which encodes a transmembrane, gap junction (GJ) channel-forming protein, connexin 26 (Cx26). GJs are clustered intercellular structures found in virtually all contacting cell types, enabling direct cell-cell communication via the exchange of ions, nutrients and signaling molecules with a molecular weight < 1 kDa (Levit et al., 2015, Elfgang et al., 1995). Connexin proteins, the constituents of GJs, can oligomerize to form hexameric structure known as connexons. On the plasma membrane, connexons can either function alone as hemichannels, or ‘dock’ with a compatible connexon from the adjacent cell membrane to form a

GJ (Laird, 2006). Undocked hemichannels serve as a conduit between the cytoplasm and the extracellular space of the cell, while GJs couple the cytoplasm of adjacent cells electrically and biochemically (Garcia et al., 2016).

To date, twelve missense *GJB2* mutations have been reported in KID syndrome, among which the mutation c.148G>A, resulting in the substitution of aspartic acid for asparagine at codon 50 (p.D50N), is by far the most common mutation, accounting for 86% of cases in the largest European cohort (Mazereeuw-Hautier et al., 2007). At least 10 out of the 12 identified mutations, including p.D50N, have been associated with aberrant hemichannel behavior (Lee et al., 2009, Garcia et al., 2016, Donnelly et al., 2012, Mese et al., 2011), presented as elevated membrane currents (Lee et al., 2009), enhanced permeability to small-molecule tracers (Mese et al., 2011), and/or enhanced ATP release in response to a specific stimuli (Garcia et al., 2016, Donnelly et al., 2012). Therefore, hemichannels have been considered a potential therapeutic target when developing new KID syndrome treatment (Levit et al., 2015, Xu et al., 2017). Recent work has shown that mefloquine, an FDA-approved anti-malarial drug, potently suppresses aberrant hemichannels in primary keratinocytes from a transgenic mouse model with heterozygous p.G45E mutation in *GJB2* (Levit et al., 2015). Very recently, the monoclonal antibody abEC1.1 was developed, which specifically suppressed hemichannels formed by Cx26-wildtype (WT), p.G45E or p.D50N mutants (Xu et al., 2017). However, it is unclear whether those strategies can discriminate mutant *GJB2* allele from the WT. This concern is particularly important given the context that most KID syndrome mutants exert dominant effects on co-expressed WT connexins (Di et al., 2005, Garcia et al., 2015). In the last decade, allele-specific small interference RNA (AS-siRNA) technology has shown strong therapeutic potential in treatment of dominant genetic

disorders and brought clinical benefits to a patient with pachyonychia congenita (Trochet et al., 2015).

We present a specific and effective AS-siRNA against the *GJB2* c.148G>A (p.D50N) mutation, which successfully rescues the abnormal cellular phenotype in patient-derived keratinocytes. Our approach could potentially be a novel future therapy for this debilitating and life-limiting condition.

RESULTS

Patient-derived keratinocytes with heterozygous c.148G>A (p.D50N) mutation had aberrant gap junction and hemichannel behavior and caused hyperkeratotic skin morphology

Previous studies on mutant *GJB2* expression, distribution and function have largely relied on ectopic expression of homozygous *GJB2* mutations in *Xenopus* oocytes (Lopez et al., 2013) and HeLa cells (Press et al., 2017b). These models, however, do not accurately represent the genetic state in KID syndrome patients who are heterozygotes for *GJB2* mutations, and therefore have limitations when used in preclinical evaluation for new therapeutic strategies. To overcome this, primary keratinocytes isolated from a fresh skin biopsy of the KID syndrome patient heterozygous for c.148G>A (p.D50N) mutation in *GJB2* were immortalized using the lentiviral vector encoding HPV type 16 E6/E7 cDNA.

The mutation *GJB2* c.148G>A was confirmed in the immortalized cells (KID-KCs) **(Figure 1a)**. Keratinocytes obtained from a healthy donor and immortalized with the same protocol were used as a control (control-KCs). Both immortalized cell lines showed polygonal morphology with various sizes in early passages but were more uniformly shaped in later passages **(Figure 1b)**. The cell morphology and genotype were monitored over a propagation period up to 45 passages. There was no apparent change in morphology and the mutation in KID-KCs was expressed stably. The

expression of endogenous *GJB2* mRNA in KID-KCs and control-KCs was examined by quantitative reverse transcriptase-PCR (qRT-PCR) using specific primers for total *GJB2*. A reduction of 44% in total *GJB2* mRNA in KID-KCs was seen compared to that in control-KCs (n = 4, $p = 0.24$) **(Figure 1c)**. The PCR amplicon of KID-KCs was sequenced, and the chromatogram exhibited a 1:1 ratio for WT : mutant allele peaks at c.148 locus **(Figure 1a)**, suggesting similar mRNA expression levels for both WT and mutant alleles in KID-KCs.

The expression of the Cx26 protein was also examined by immunoblotting. Several anti-Cx26 antibodies have been used in immunoblotting previously (Yum et al., 2007, Press et al., 2017a), but the majority was used to detect Cx26 in rodent cells or tissues or in HeLa cells ectopically expressing Cx26, and only few were able to detect endogenous Cx26 in cultured human keratinocytes. This is possibly due to low endogenous Cx26 level or a lack of anti-Cx26 antibodies with sufficient affinity/specificity. We tested six antibodies and found that the pair of a rabbit polyclonal antibody (Thermo Fisher Scientific, 13-8100) and a mouse monoclonal antibody (Merck Millipore, MABT198) gave a clear band at 26 kDa when used for immunoprecipitation experiments **(Figure 1d)**. Immunoprecipitation using these pair of antibodies showed a reduction in Cx26 protein expression in KID-KCs compared to control-KCs, which was consistent with the qRT-PCR results.

The distribution of Cx26 in the cells was determined using immunostaining. In control-KCs, punctate or plaque-like Cx26 staining was observed at cell-cell contact sites **(Figure 1e)**, which were indicated by membranous staining of E-cadherin, suggesting that WT Cx26 was able to traffic to the plasma membrane and formed GJ plaques. By contrast, Cx26 in KID-KCs failed to accumulate at membrane regions but showed a primarily discrete punctate staining pattern in the cytoplasm **(Figure 1e)**. Although a small portion of GJ plaques overlaid with E-cadherin at the

plasma membrane, they were smaller in size compared to those observed in control-KCs. Interestingly, the immunostaining pattern of the patient skin did not show striking reduction or mis-localization of Cx26 expression **(Figure 1f)**. This could be, in part, explained by the *in vitro* culture condition which rendered keratinocytes more proliferative and less differentiative, given that Cx26 is predominantly expressed in differentiated keratinocytes (Churko and Laird, 2013, Martin et al., 2014).

The function of GJ intercellular communication in KID-KCs was assessed by scrape-loading dye transfer (SLDT) using the neurobiotin tracer and compared to control-KCs. Neurobiotin diffused extensively from initially scrape-loaded cells to neighboring cells in control-KCs **(Figure 2a)**. In contrast, the diffusion of neurobiotin in KID-KCs reduced markedly and was almost confined to the first line of the scrape-wounded cells. Quantification of the images revealed a reduction of 58% in diffusion area in KID-KCs, compared to that in control-KCs (n = 3 each, $p < 0.01$), suggesting that the GJ channels formed in KID-KCs were defective **(Figure 2b)**.

Next, the activity of hemichannels in KID-KCs was measured using whole-cell patch clamp and neurobiotin uptake assay. Moderate membrane currents were recorded from control-KCs at both depolarizing and hyperpolarizing membrane voltages, whereas large currents were elicited from KID-KCs at all tested membrane voltages, more prominently at depolarizing voltages between +30 mV and +110 mV **(Figure 2c)**. The maximum current density recorded from KID-KCs was 80% greater than that in control-KCs (9.0 ± 1.3 pA/pF, n = 21 cells vs. 5.0 ± 0.6 pA/pF, n = 14 cells, measured at +110 mV, $p < 0.05$) **(Figure 2d)**. Consistent with the patch clamp results, KID-KCs showed a marked increase in uptake of neurobiotin tracer compared to control-KCs (n = 29 and 34 cells, respectively, $p < 0.001$) **(Figure 2e)**. These results suggested enhanced membrane conductivity and neurobiotin permeability in KID-KCs, indicating hyperactive hemichannel

behavior conferred by the mutation. Our *in vitro* findings indicated that, despite expressing Cx26 at a relatively low level in culture, the KID-KCs displayed an aberrant cellular phenotype that has been reported previously in other KID syndrome disease models (Arita et al., 2006, Lee et al., 2009, Garcia et al., 2016).

To confirm that the immortalized KID-KCs remained capable of proliferation and differentiation, i.e. characteristics of primary keratinocytes *in vivo*, these cells were tested in a human-murine chimeric skin graft model (Di et al., 2011). Histological examination of the skin graft regenerated from immortalized KID-KCs showed similar features seen in the KID syndrome patient skin, including hyperkeratosis and spongiosis **(Figure 3)**. Collectively, the immortalized KID-KCs are a suitable model for evaluating therapeutic efficacy of AS-siRNA for KID syndrome.

AS-siRNA selectively inhibited the c.148G>A mutation in KID-KCs

Nineteen candidate AS-siRNAs with a targeting sequence complementary to the c.148G>A mutation (S1−S19) were screened at a concentration of 50 nM in Hela cell lines stably expressing WT or mutant *GJB2* fused with the *GFP* reporter gene. Both cell lines were transfected with each of 19 AS-siRNAs, followed by flow cytometry analysis for reduction of GFP intensity **(Supplementary Figure S1b)**. The knockdown efficiency of S7 and S10 in cells expressing the mutant *GJB2-GFP* was approximately 50%. Since S7 inhibited mutant *GJB2* specifically and reproducibly from three independent screening experiments **(Supplementary Figure S2)**, this siRNA was selected for further study.

The allele-specific action of S7 at 50 nM was tested in the KID-KCs harboring the heterozygous mutation. KID-KCs and control-KCs were treated with S7 and the mRNA expression of *GJB2* in treated cells was examined 24 hrs post-treatment by qRT-PCR. The treatment resulted in a

significant decrease of 63% in total *GJB2* mRNA in KID-KCs compared to untreated cells (n = 3, $p = 0.0065$), but the decrease was not detected in control-KCs with the same treatment (n = 3, $p = 0.84$) **(Figure 4a)**. Further investigation using allele-specific primers showed no difference in mRNA expression of the WT allele between untreated and S7-treated cells (n = 3, $p = 0.51$ for KID-KCs and $p = 0.60$ for control-KCs), whereas mRNA expression of the mutant allele in KID-KCs was significantly inhibited by 43% following S7 treatment (n = 3, $p = 0.0065$). At protein level, Cx26 expression showed an average decrease of 56% (range 52−64%, n = 3) in total endogenous Cx26 expression in KID-KCs following S7 treatment, compared to those treated with an irrelevant siRNA, si-cont **(Figure 4b-c)**. This change was not detected in S7-treated control-KCs, which showed a slight increase in Cx26 expression (range 5−16%, n = 3). All these results indicated that S7 had strong selectivity for the mutant *GJB2* c.148G>A allele over the WT allele in the patient keratinocytes, and it had little effect on the normal keratinocytes where only the WT allele was present.

AS-siRNA treatment reversed aberrant gap junction and hemichannel functions in KID-KCs

KID-KCs treated with S7 or si-cont at 50 nM were further analyzed for GJ intercellular communication and hemichannel activity. GJ-mediated intercellular diffusion of neurobiotin tracer was analyzed 24 hrs post-treatment using the SLDT assay. The results showed a 24% increase in neurobiotin diffusion in KID-KCs treated with S7 compared to those treated with si-cont (n = 34 and 37 images, respectively, $p < 0.01$) **(Figure 5b, d)**, whereas no significant difference in neurobiotin transfer was observed in control-KCs treated with either S7 or si-cont (n = 30 and 35 images, respectively, $p > 0.05$) **(Figure 5a, c)**. The hemichannel activity in the treated cells was assessed by whole-cell patch clamp. The results showed a decrease of 35% in membrane current

density in KID-KCs treated with S7, compared to those treated with si-cont (9.02 ± 1.16 pA/pF, n = 20 cells vs. 5.86 ± 0.43 pA/pF, n = 22 cells, measured at +110 mV, $p < 0.05$), while no statistical differences were found in control-KCs following S7 or si-cont treatment (n =10 cells each group, $p > 0.05$) **(Figure 5f-h)**. Notably, the current density level in S7-treated KID-KCs was comparable to that in control-KCs**.** The activity of hemichannels was further examined by neurobiotin uptake assay, which showed a significant decrease in neurobiotin uptake in KID-KCs after S7 treatment (n = 21 and 27 images, $p < 0.001$), in line with the patch clamp results **(Figure 5i-j)**.

These findings suggested functional recovery following the inhibition of mutant *GJB2* allele by S7, namely improvement of the defective GJ-mediated cell coupling and reversal of the aberrant non-junctional hemichannel behavior, including electrical conduction and permeability.

Low-level off-target effects of AS-siRNA, S7

Despite promising efficacy data obtained from S7, a general concern in preclinical AS-siRNA studies is off-target effects that may cause unintended alteration in unrelated gene expression (Trochet et al., 2018). To explore comprehensively the specificity of S7, RNA-Seq was carried out S7-treated or non-treated KID-KCs. 26485 genes from the libraries were mapped to the reference human genome (with 15,802 null- or low-expressed genes), among which only 6 genes were found to be differentially expressed in S7-treated KID-KCs compared to the non-treated cells (range of fold change: 2.01−2.32), indicating that S7 resulted in mild global effects on the KID-KC transcriptome. To validate the results, the top 5 upregulated (*MMP1*, *MMP10*, *MMP9*, *ANGPTL4*, *CXCL5*) and downregulated genes (*GLB1L2*, *NSA2*, *AFAP1L1*, *GPR137*, *TMEM109*) were further analyzed by qRT-PCR **(Table 1)**. Control-KCs with or without S7 treatment were run in parallel as additional controls. The results confirmed the upregulation of the *MMPs* and the downregulation

of *GPR137* in KID-KCs with comparable levels of fold change **(Supplementary Figure S4)**; however, the *MMPs* were also found upregulated in S7-treated control-KCs.

A common cause of siRNA-mediated gene alteration is sequence matching between the seed region of siRNA and the target mRNA (Yilmazel et al., 2014, Jackson and Linsley, 2010). To investigate whether this was an underlying mechanism for the differential expression of the above genes, we employed the online tool, genome-wide enrichment of seed sequences (GESS), to analyze the sequence of S7. A total of 180 genes were found to have sequence match(es) with S7 **(Supplementary Table S2)**, among which only *GPR137* was found, with its 3'-untranslated region and coding sequence complementary to the seed region of either of the S7 strands. This implied that downregulation of *GPR137* may have resulted from seed region-dependent off-target effects. The mechanism of alteration of the other genes remains to be clarified.

DISCUSSION

We study AS-siRNA using KID-KC, an immortalized, patient-derived keratinocyte cell line which harbors a heterozygous c.148G>A mutation, representing the genetic state in KID syndrome patients. Although use of primary keratinocytes from patient skin biopsy would have been ideal for this study, these cells have a limited lifespan which restricts us from performing multiple experiments. To bypass the restrictions, we used immortalized patient keratinocytes due to their indefinite lifespan and capability of proliferation and differentiation, i.e. features of primary keratinocytes (Choi et al., 2017). This was further confirmed in our *in vivo* skin graft experiments, where regenerated skin grafts from immortalized KID-KCs recapitulated the epidermal architecture of the KID syndrome patient skin.

Our immunostaining found lower Cx26 expression level in cultured immortalized cells compared to that in skin tissues. This is not surprising, as monolayer culture contains a dominating proportion of proliferating keratinocytes with low-level Cx26 expression (Martin et al., 2014). Despite the lower expression, we were able to show aberrant hemichannel and GJ behavior in KID-KCs, which is in line with data generated from previous *in vitro* models such as *Xenopus* oocytes (Lee et al., 2009, Sanchez et al., 2013), HeLa cells (Di et al., 2005) and corneal epithelial cells (Shurman et al., 2005) ectopically expressing the c.148G>A mutant. This suggested that the reduced Cx26 expression *in vitro* is unlikely to influence the interpretation of our results. Collectively, the immortalized, patient-derived model, which recapitulates the genetics, cellular and histological phenotypes of the condition, has significant advantages over the previous models and hence can serve as a good preclinical model for translational development of new therapeutic approaches.

The action of previously reported approaches to inhibit connexins, including monoclonal antibodies (Xu et al., 2017) and synthetic peptide mimetics (Becker et al., 2012), is mediated by either altering the biophysical property of target connexin channels or modulating interaction between target connexins and their binding partners. In contrast to those approaches, AS-siRNA silences target gene expression by degrading mRNA based on perfect sequence matching, thereby blocking the translation of target protein (Jackson and Linsley, 2010). As AS-siRNA is able to discriminate mutant and WT mRNA sequences differing by even a single base, we harness this technology to develop a targeted therapy for KID syndrome. Our results have confirmed that the lead AS-siRNA, S7, targeted to the mutant *GJB2* allele in a potent and specific manner while maintaining expression of the WT allele and its protein function, providing strong basis for future translation of the AS-siRNA.

In human keratinocytes, Cx26 forms heteromeric and heterotypic channels with other compatible types of connexins (Di et al., 2001). These heterogenous channels have biophysical properties differing from their homogenous counterparts, providing dynamic regulation in response to different stimuli. Recent studies proposed that aberrant interaction with Cx43 is an emerging mechanism by which certain Cx26 mutants can cause diseases through heteromeric channels (Garcia et al., 2015, Shuja et al., 2016). We performed double immunofluorescence staining in our patient skin tissues and cultured KID-KCs, and the results did not show clear colocalization between Cx26 and Cx43 (data not shown). As this is our preliminary data, further investigation is required in the future.

The low endogenous expression of Cx26 in human keratinocytes (Richard et al., 2002, Di et al., 2001) posted a challenge in our initial attempts of immunoblotting to detect Cx26, which showed multiple bands. Issues regarding the presence of multiple bands were also reported by others (Gassmann et al., 2009), and were considered to result from oligomers and protein aggregates of Cx26. Our optimized immunoprecipitation/immunoblotting approach allowed enrichment of low-abundant Cx26 in cultured patient keratinocytes, leading to successful quantification of siRNA-medicated Cx26 knockdown.

Our work provides proof-of-concept for the use of AS-siRNA in targeted therapy for KID syndrome. In the context of patient skin, the AS-siRNA-mediated reversal of connexin channel function may possibly improve the disturbed epidermal Ca^{2+} gradient that is contributed by homomeric or heteromeric channels formed by mutant Cx26 (Bosen et al., 2015), thereby leading to improved hyperkeratotic phenotype. Also, since enhanced hemichannel activity has been linked to release of inflammatory cytokines when exposing c.148G>A-expressing keratinocytes to peptidoglycans from an opportunistic pathogen, *Staphylococcus aureus* (Donnelly et al., 2012),

AS-siRNA is also likely to contribute towards control of skin infection and inflammation. Furthermore, the c.148G>A mutation has been found in the majority of KID syndrome patients. Thus, the mutation-targeted AS-siRNA would serve as potentially effective and safe therapeutic intervention for KID syndrome, the debilitating condition that has no effective specific treatment options at present. Although *in vivo* delivery of siRNA remains challenging, strategies including nanoparticles (Zheng et al., 2012), penetration enhancers (Hegde et al., 2014), microneedles (Chong et al., 2013) and electroporation (Broderick et al., 2012) have shown promise in topical siRNA delivery into the skin in a non- or minimally-invasive manner, causing silencing of target genes. We are currently optimizing a topical delivery platform and the therapeutic efficacy of the AS-siRNA will be tested in our *in vivo* human-murine chimeric skin graft model generated using immortalized KID-KCs. If successful, our strategy could potentially be adapted to other skin conditions with dominant mutations.

MATERIALS AND METHODS

KID syndrome patient-derived keratinocytes

3-mm punch biopsies from a KID syndrome patient with the heterozygous c.148G>A mutation, and a healthy volunteer donor, were obtained under a protocol approved by the local ethics committee (12/LO/1522) with informed written consent. The epidermis was isolated freshly from the biopsies as described previously (Di et al., 2011). The primary keratinocytes were immortalized by transduction with a second-generation, replication-deficient, self-inactivating HIV-1 lentiviral vector (Yanez-Munoz et al., 2006) constructed with human papilloma virus type 16 E6/E7 cDNA (**Supplementary Figure S3**). Immortalized cells were established following serial propagation and thereafter were cultured in the keratinocyte culture medium without feeder cells.

Statistical analysis

All data were expressed as the mean ± standard error of the mean (SEM). Comparisons of data from qRT-PCR, patch clamp, neurobiotin uptake and SLDT experiments were made by Student's t-test using GraphPad Prism v6.01 (GraphPad Software, San Diego, CA, USA). Differences with a p-value less than 0.05 were considered statistically significant. *$p < 0.05$; **$p < 0.01$; and ***$p < 0.001$.

Detailed methods for immunostaining, siRNA design, qRT-PCR, immunoprecipitation and immunoblotting, patch clamp, neurobiotin uptake, SLDT, RNA-Seq and *in vivo* skin graft experiments are described in **Supplementary Materials**.

DATA AVAILABILITY STATEMENT

Datasets related to this article can be found at https://www.ncbi.nlm.nih.gov/geo/query/acc.cgi?acc=GSE131709, an open-source online data repository hosted at Gene Expression Omnibus (GEO).

CONFLICT OF INTEREST

The authors declared no conflict of interest.

ACKNOWLEDGMENTS

We gratefully acknowledge the participation of all patients and families in this study, as well as the National Institute for Health Research (NIHR) Biomedical Research Centre based at Great Ormond Street Hospital for Children NHS Foundation Trust and UCL Institute of Child Health. The views expressed are those of the author(s) and not necessarily those of the NHS, the NIHR or the Department of Health. This work was also supported by Newlife Foundation for Disabled Children and the UCL Bogue Fellowship. We are indebted to Dr. Ayad Eddaoudi and Dr. Dale Moulding (ICH Core Facility) for their expertise in flow cytometry and image analysis. WLD is a Great Ormond Street Hospital Children's Charity Senior Lecturer. TWW is funded by the National Institutes of Health (grant numbers EY013163 and EY026911). VAK is funded by the Wellcome Trust (grant number WT104076MA).

REFERENCES

Arita K, Akiyama M, Aizawa T, Umetsu Y, Segawa I, Goto M, et al. A novel N14Y mutation in Connexin26 in keratitis-ichthyosis-deafness syndrome: analyses of altered gap junctional communication and molecular structure of N terminus of mutated Connexin26. Am J Pathol 2006; 169, 416-23.

Becker DL, Thrasivoulou C, Phillips AR. Connexins in wound healing; perspectives in diabetic patients. Biochim Biophys Acta 2012; 1818: 2068-75.

Bosen F, Celli A, Crumrine D, Vom Dorp K, Ebel P, Jastrow H, et al. Altered epidermal lipid processing and calcium distribution in the KID syndrome mouse model Cx26S17F. FEBS Lett 2015; 589: 1904-10.

Broderick KE, Chan A, Lin F, Shen X, Kichaev G, Khan AS, et al. Optimized in vivo transfer of small interfering RNA targeting dermal tissue using in vivo surface electroporation. Mol Ther Nucleic Acids 2012; 1, e11.

Burns FS. A case of generalized congenital keratoderma with unusual involvement of eyes, ears and nasal and buccal mucous membranes. J Cutan Dis 1915; 33: 255-60.

Caceres-Rios H, Tamayo-Sanchez L, Duran-Mckinster C, De La Luz Orozco M, Ruiz-Maldonado R. Keratitis, ichthyosis, and deafness (KID syndrome): review of the literature and proposal of a new terminology. Pediatr Dermatol 1996; 13: 105-13.

Choi M, Park M, Lee S, Lee JW, Cho MC, Noh M, et al. Establishment of Immortalized Primary Human Foreskin Keratinocytes and Their Application to Toxicity Assessment and Three Dimensional Skin Culture Construction. Biomol Ther (Seoul) 2017; 25, 296-307.

Chong RH, Gonzalez-Gonzalez E, Lara MF, Speaker TJ, Contag CH, Kaspar RL, et al. Gene silencing following siRNA delivery to skin via coated steel microneedles: In vitro and in vivo proof-of-concept. J Control Release 2013; 166, 211-9.

Churko JM. and Laird DW. Gap Junction Remodeling in Skin Repair Following Wounding and

Disease. Physiology 2013; 28, 190-198.

Coggshall K, Farsani T, Ruben B, Mccalmont TH, Berger TG, Fox LP, et al. Keratitis, ichthyosis, and deafness syndrome: a review of infectious and neoplastic complications. J Am Acad Dermatol 2013; 69: 127-34.

Di WL, Gu Y, Common JE, Aasen T, O'toole EA, Kelsell DP, et al. Connexin interaction patterns in keratinocytes revealed morphologically and by FRET analysis. J Cell Sci 2005; 118: 1505-14.

Di WL, Larcher F, Semenova E, Talbot GE, Harper JI, Del Rio M, et al. Ex-vivo gene therapy restores LEKTI activity and corrects the architecture of Netherton syndrome-derived skin grafts. Mol Ther 2011; 19: 408-16.

Di WL, Rugg EL, Leigh IM, Kelsell DP. Multiple epidermal connexins are expressed in different keratinocyte subpopulations including connexin 31. J Invest Dermatol 2001; 117: 958-64.

Donnelly S, English G, de Zwart-Storm EA, Lang S, van Steensel MA, Martin PE. Differential susceptibility of Cx26 mutations associated with epidermal dysplasias to peptidoglycan derived from Staphylococcus aureus and Staphylococcus epidermidis. Exp Dermatol 2012; 21: 592-8.

Elfgang C, Eckert R, Lichtenberg-Frate H, Butterweck A, Traub O, Klein RA, et al. Specific permeability and selective formation of gap junction channels in connexin-transfected HeLa cells. J Cell Biol 1995; 129: 805-17.

Garcia IE, Bosen F, Mujica P, Pupo A, Flores-Munoz C, Jara O, et al. From hyperactive connexin26 hemichannels to impairments in epidermal calcium gradient and permeability barrier in the keratitis-ichthyosis-deafness syndrome. J Invest Dermatol 2016; 136: 574-83.

Garcia IE, Maripillan J, Jara O, Ceriani R, Palacios-Munoz A, Ramachandran J, et al. Keratitis-ichthyosis-deafness syndrome-associated Cx26 mutants produce nonfunctional gap junctions but hyperactive hemichannels when co-expressed with wild type Cx43. J Invest Dermatol 2015; 135: 1338-47.

Gassmann O, Kreir M, Ambrosi C, Pranskevich J, Oshima A, Roling C, et al. The M34A mutant of connexin26 reveals active conductance states in pore-suspending membranes. J Struct Biol 2009; 168: 168-76.

Hegde V, Hickerson RP, Nainamalai S, Campbell PA, Smith FJ, Mclean WH, et al. In vivo gene silencing following non-invasive siRNA delivery into the skin using a novel topical formulation. J Control Release 2014; 196, 355-62.

Jackson AL, Linsley PS. Recognizing and avoiding sirna off-target effects for target identification and therapeutic application. Nat Rev Drug Discov 2010; 9: 57-67.

Laird DW. Life cycle of connexins in health and disease. Biochem J 2006; 394: 527-43.

Lee JR, Derosa AM, White TW. Connexin mutations causing skin disease and deafness increase hemichannel activity and cell death when expressed in xenopus oocytes. J Invest Dermatol 2009; 129: 870-8.

Levit NA, Sellitto C, Wang HZ, Li L, Srinivas M, Brink PR, et al. Aberrant connexin26 hemichannels underlying keratitis-ichthyosis-deafness syndrome are potently inhibited by mefloquine. eInsights on the mechanisms of Ca2+ regulation of connexin26 hemichannels revealed by human pathogenic mutations (D50N/Y). J Gen Physiol 2013; 142: 23-35.

Martin PE, Easton JA, Hodgins MB, Wright CS. Connexins: sensors of epidermal integrity that are therapeutic targets. FEBS Lett 2014; 588, 1304-14.

Mazereeuw-Hautier J, Bitoun E, Chevrant-Breton J, Man SY, Bodemer C, Prins C, et al. Keratitis-ichthyosis-deafness syndrome: disease expression and spectrum of connexin 26 (GJB2) mutations in 14 patients. Br J Dermatol 2007; 156: 1015-9.

Mese G, Sellitto C, Li L, Wang HZ, Valiunas V, Richard G, et al. The Cx26-G45E mutation displays increased hemichannel activity in a mouse model of the lethal form of keratitis-ichthyosis-deafness syndrome. Mol Biol Cell 2011; 22: 4776-86.

Patel V, Sun G, Dickman M, Khuu P, Teng JM. Treatment of keratitis-ichthyosis- deafness (KID) syndrome in children: a case report and review of the literature. Dermatol Ther 2015; 28:

89-93.

Press ER, Shao Q, Kelly JJ, Chin K, Alaga A, Laird DW. Induction of cell death and gain-of-function properties of connexin26 mutants predict severity of skin disorders and hearing loss. J Biol Chem 2017; 292: 9721-32.

Richard G, Rouan F, Willoughby CE, Brown N, Chung P, Ryynanen M, et al. Missense mutations in GJB2 encoding connexin-26 cause the ectodermal dysplasia keratitis-ichthyosis-deafness syndrome. Am J Hum Genet 2002; 70: 1341-8.

Sanchez HA, Villone K, Srinivas M, Verselis VK. The D50N mutation and syndromic deafness: altered Cx26 hemichannel properties caused by effects on the pore and intersubunit interactions. J Gen Physiol 2013; 142: 3-22.

Shuja Z, Li L, Gupta S, Mese G, White TW. Connexin26 Mutations Causing Palmoplantar Keratoderma and Deafness Interact with Connexin43, Modifying Gap Junction and Hemichannel Properties. J Invest Dermatol 2016; 136, 225-35.

Shurman DL, Glazewski L, Gumpert A, Zieske JD, Richard G. In vivo and in vitro expression of connexins in the human corneal epithelium. Invest Ophthalmol Vis Sci 2005; 46: 1957-65.

Trochet D, Prudhon B, Beuvin M, Peccate C, Lorain S, Julien L, et al. Allele-specific silencing therapy for dynamin 2-related dominant centronuclear myopathy. EMBO Mol Med 2018; 10: 239-253.

Trochet D, Prudhon B, Vassilopoulos S, Bitoun M. Therapy for dominant inherited diseases by allele-specific RNA interference: successes and pitfalls. Curr Gene Ther 2015; 15: 503-10.

van Steensel MA, van Geel M, Nahuys M, Smitt JH, Steijlen PM. A novel connexin 26 mutation in a patient diagnosed with keratitis-ichthyosis-deafness syndrome. J Invest Dermatol 2002; 118, 724-7.

Wang HJ, Chen TM, Cheng LF, Cheng TY, Tung YM. Human keratinocyte culture using porcine pituitary extract in serum-free medium. Burns 1995; 21, 503-6.

Xu L, Carrer A, Zonta F, Qu Z, Ma P, Li S, et al. Design and characterization of a human monoclonal antibody that modulates mutant connexin 26 hemichannels implicated in deafness and skin disorders. Front Mol Neurosci 2017; 10: 298.

Yanez-Munoz RJ, Balaggan KS, Macneil A, Howe SJ, Schmidt M, Smith AJ, et al. Effective gene therapy with nonintegrating lentiviral vectors. Nat Med 2006; 12, 348-53.

Yilmazel B, Hu Y, Sigoillot F, Smith JA, Shamu CE, Perrimon N, et al. Online GESS: prediction of miRNA-like off-target effects in large-scale rnai screen data by seed region analysis. BMC Bioinformatics 2014; 15: 192.

Yum SW, Zhang J, Valiunas V, Kanaporis G, Brink PR, White TW, et al. Human connexin26 and connexin30 form functional heteromeric and heterotypic channels. Am J Physiol Cell Physiol 2007; 293, C1032-48.

Zheng D, Giljohann DA, Chen DL, Massich MD, Wang XQ, Iordanov H, et al. Topical delivery of siRNA-based spherical nucleic acid nanoparticle conjugates for gene regulation. Proc Natl Acad Sci U S A 2012 109, 11975-80.

TABLES

Table 1. Top five up- and downregulated genes from the RNA-Seq experiments

Top five upregulated genes (KID-KCs, S7 vs. untreated)			
Gene	Protein	Fold Change	*p-adj
MMP1	Matrix metalloproteinase-1	2.24, up	9.50E-22
MMP10	Matrix metalloproteinase-10	2.06, up	4.19E-30
MMP9	Matrix metalloproteinase-9	1.95, up	4.90E-65
ANGPTL4	Angiopoietin-like 4	1.93, up	3.57E-28
CXCL5	C-X-C motif chemokine 5	1.74, up	6.26E-45
Top five downregulated genes (KID-KCs, S7 vs. untreated)			
Gene	Protein	Fold Change	*p-adj
GLB1L2	Galactosidase Beta 1 Like 2	2.31, down	2.17E-14
NSA2	Ribosome biogenesis homolog	2.16, down	1.99E-68
AFAP1L1	Actin filament-associated protein 1-like 1	2.01, down	1.99E-27
GPR137	G protein-coupled receptor 137	2.00, down	3.96E-09
TMEM109	Transmembrane Protein 109	1.94, down	3.92E-47

*p-adj, adjusted p-value for multiple statistical testing (Benjamini-Hochberg method)

FIGURE LEGENDS

Figure 1. Genotype, morphology, *GJB2* expression and subcellular localization in keratinocytes

cDNA sequences of *GJB2* from the KID syndrome patient and healthy donor are shown in (a). The morphology of keratinocytes from healthy donor and KID patient at early passages (P1 or P5) and late passages (P35 or P45) is shown in (b). The mRNA expression of total *GJB2*, the wildtype (WT) allele and the mutant allele in healthy donor and KID patient keratinocytes determined by qRT-PCR are shown in (c). The total Cx26 protein (asterisk, at 26 kDa) expression was examined by immunoprecipitation and immunoblotting (d), which shows decreased Cx26 expression in patient cells. The expression of Cx26 detected by immunofluorescence staining is shown in (e), where gap junction plaques can be found at cell-cell junctions in normal keratinocyte (arrows), whereas Cx26 in KID patient keratinocytes was localized discretely in the cytoplasm (arrowheads). E-cadherin (E-Cad) was stained in green color. Cx26 expression in the skin is shown in (f), where punctate staining of Cx26 was observed (arrows). The dotted lines show dermal-epidermal junction. Bar = 100 μm (b) and 40 μm (e, f). KID: KID patient-derived keratinocytes; Cont: keratinocytes derived from the healthy donor; N.S: not significant; ***$p < 0.001$.

Figure 2. Abnormal gap junction and hemichannel behavior in KID-KCs

The gap junction intercellular communication in KID-KCs (KID) or control-KCs (Cont) was examined by the SLDT assay, and the hemichannel activity was examined by whole-cell patch clamp and neurobiotin uptake. Representative images of SLDT in the keratinocytes using neurobiotin tracer (red) is shown in (a). Data analysis (b) shows that KID-KCs had impaired ability to transfer neurobiotin to adjacent cells. Representative patch clamp records from single

keratinocytes in response to the voltage step protocol from -110 mV to +110 mV in 20 mV increments are shown in (c). The plot of current density against membrane voltage reveals aberrantly enhanced hemichannel activity in KID-KCs (d). Representative images of neurobiotin uptake (NB, red) are shown (e), with the nuclei stained with DAPI (blue). Data analysis shows increased uptake of NB in KID-KCs (f). All data are presented as the mean ± SEM. *$p < 0.05$; ***$p < 0.001$. Bar = 200 μm.

Figure 3. Epidermal morphology of grafted skin in human-murine chimeric skin graft model

Primary fibroblasts and immortalized keratinocytes derived from the KID syndrome patient harboring heterozygous *GJB2* c.148G>A mutation or a healthy donor were used to generate bio-engineered skin sheets, which were grafted onto NOD-severe combined immunodeficiency mice (NSG mice). Eight weeks post-grafting, regenerated skin grafts were harvested. Macroscopic examination showed fine, dry scales in the graft generated from patient cells (d) compared to that generated from control cells (a). Histological examination showed hyperkeratosis and spongiosis in the patient skin graft (f), resembling that seen in the patient skin (c). The skin architecture of the control skin graft (e) was also similar to healthy donor skin (b). Bar = 100 μM.

Figure 4. Allele-specific GJB2 knockdown by S7

The mRNA expression of total *GJB2*, wildtype (WT) and the mutant (MUT) *GJB2* alleles in control-KCs (Control) and KID-KC (KID) treated with AS-siRNA S7 was examined by qRT-PCR and compared to untreated cells (UT) (a). Total Cx26 protein expression in S7-treated cells from three independent immunoprecipitation(IP)/immunoblotting(IB) experiments (b). The expression was quantified using densitometry (c). β-actin was used as a loading control and HeLa cells were

used as a negative control. A reduction in total Cx26 expression was detected in KID-KCs after S7 treatment, but such a change was not detected in control-KCs. N.S, not significant; **$p < 0.01$

Figure 5. S7 treatment corrected abnormal gap junction and hemichannel functions in KID-KCs

SLDT was performed in siRNA-treated KID-KCs (KID) and control-KCs (Cont) to assess GJ activity (a, b). The analysis of neurobiotin transfer (red) is shown (c, d). Each dot in panels c and d represents the average neurobiotin transfer from a single image. Three independent experiments were carried out and at least ten images were analyzed from each experiment. Restoration of GJ activity was detected in KID-KCs following S7 treatment. Whole-cell patch clamp (e-h) and neurobiotin uptake (i, j) were carried out to examine hemichannel activity. Records of currents from single cells under the voltage step protocol (e) are shown (f, g). The plot of current density against membrane voltage shows correction of hyperactive hemichannels in KID-KCs after S7 treatment (h). Representative neurobiotin (NB, red) uptake images are shown in (i). The nuclei were stained with DAPI (blue). Data analysis shows reversal of aberrantly enhanced NB uptake in KID-KCs (j). Data are presented as the mean ± SEM. N.S, not significant; *$p < 0.05$; **$p < 0.01$; ***$p < 0.001$. Bar = 200 μm.

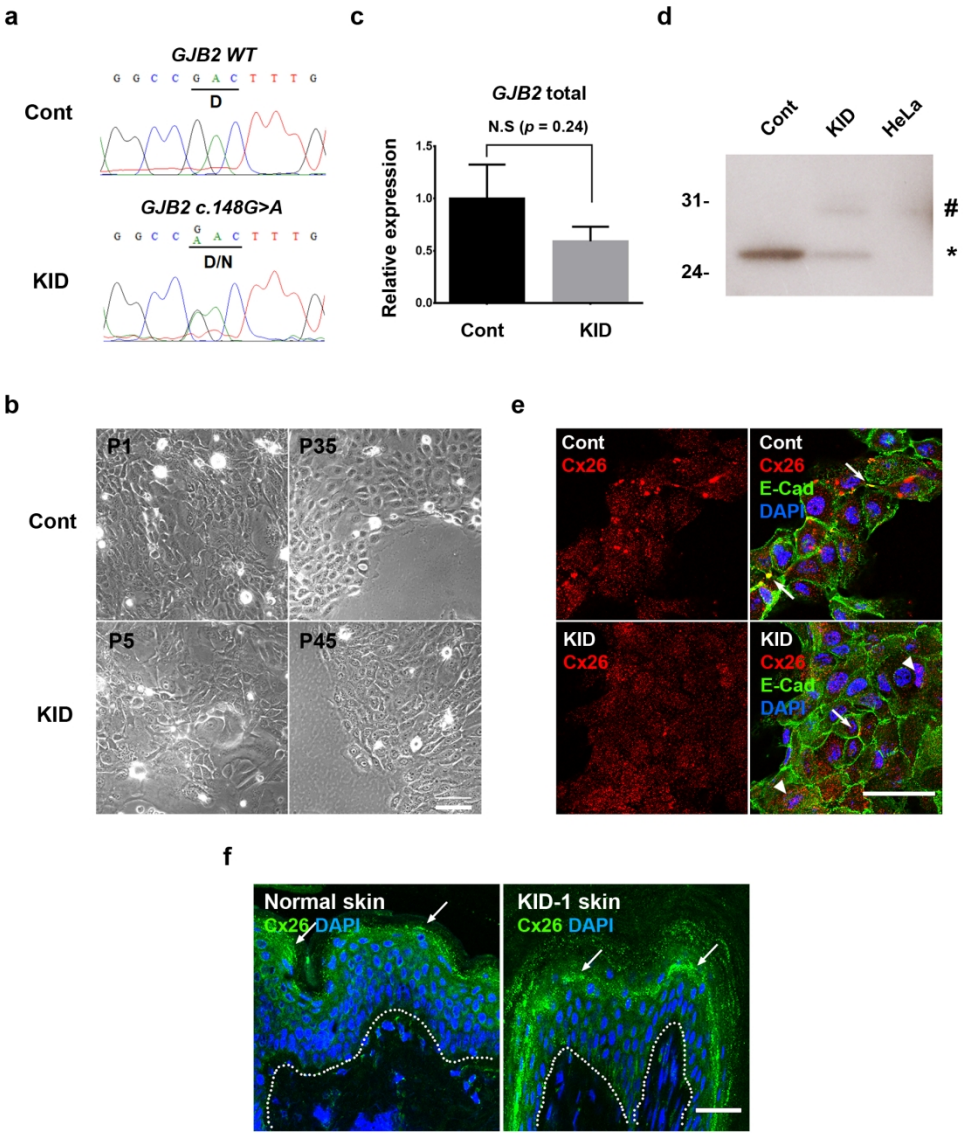

Genotype, morphology, GJB2 expression and subcellular localization in keratinocytes

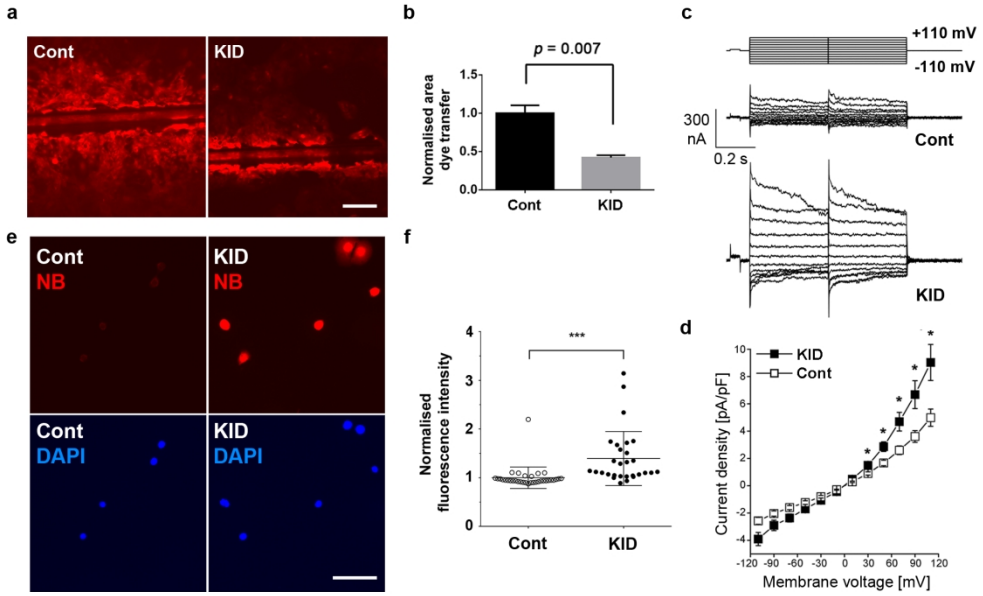

Abnormal gap junction and hemichannel behavior in KID-KCs

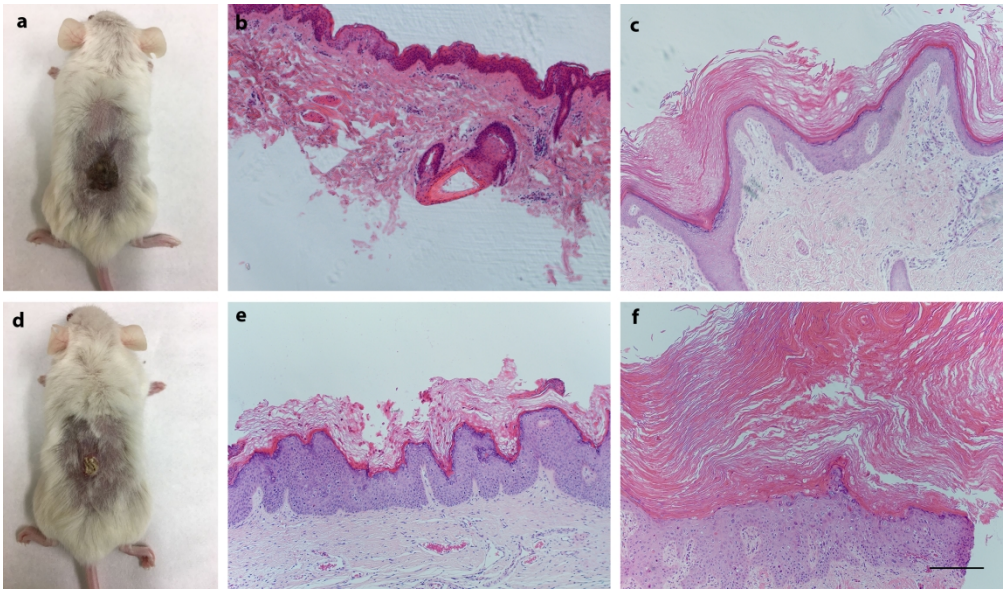

Epidermal morphology of grafted skin in human-murine chimeric skin graft model

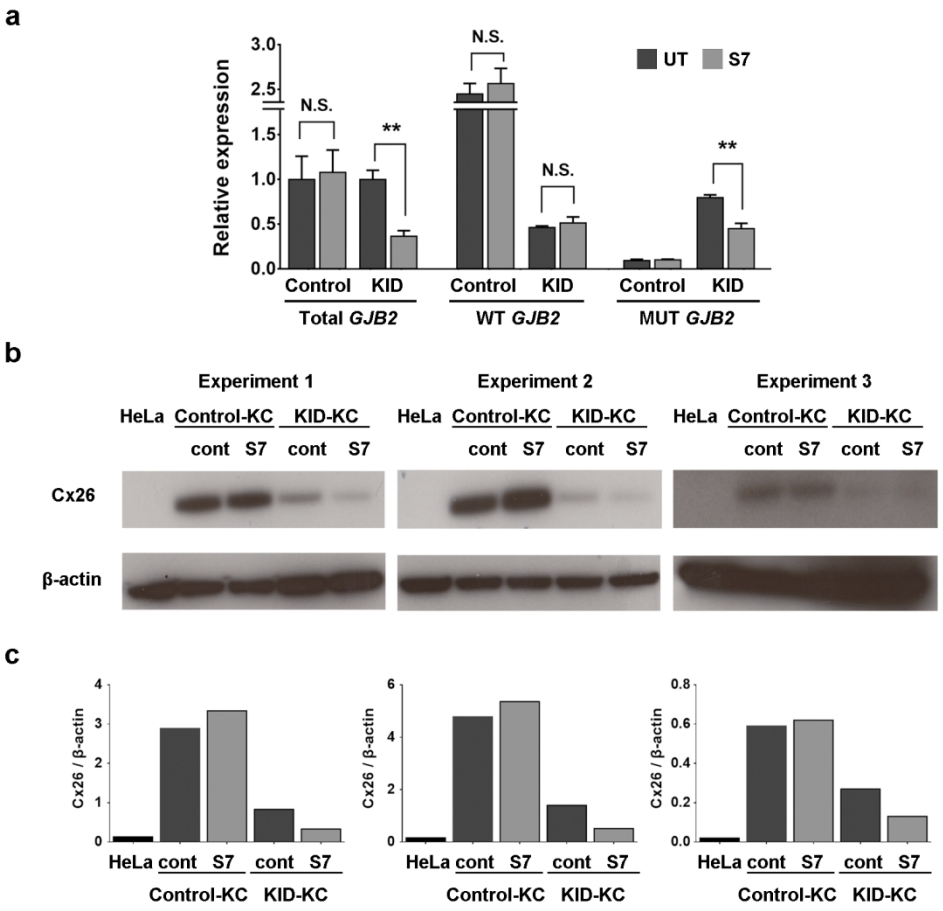

Allele-specific GJB2 knockdown by S7

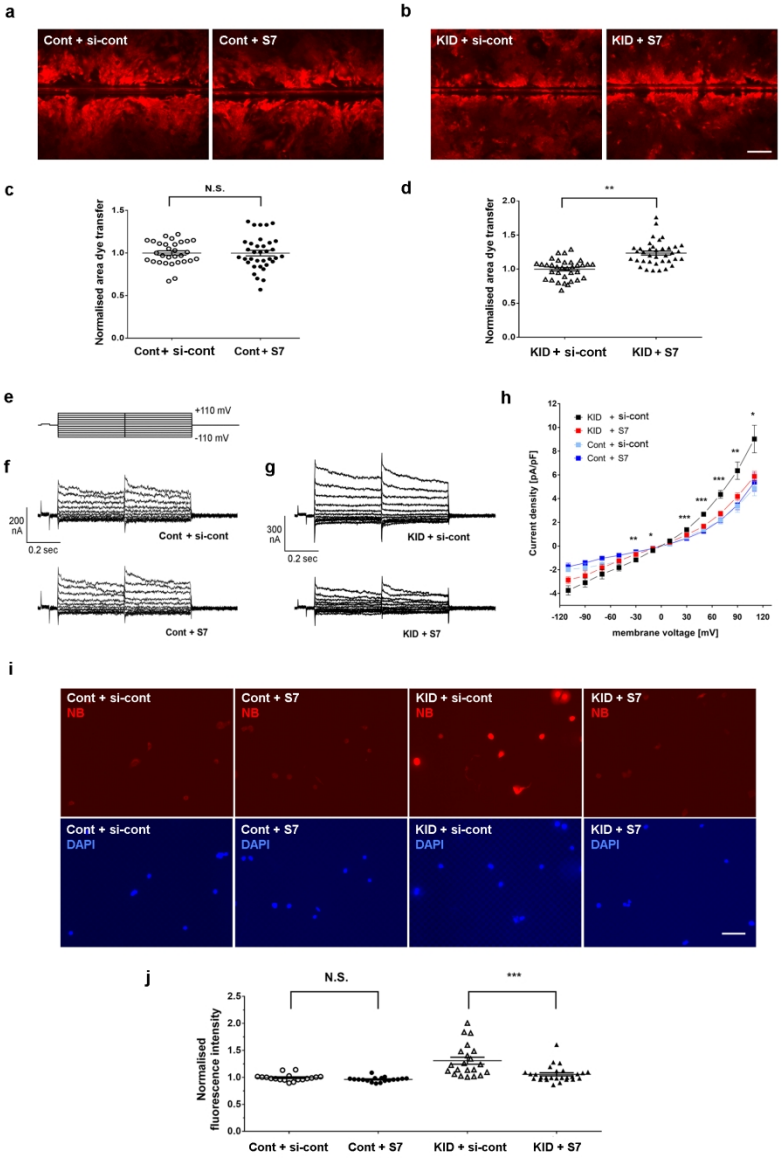

S7 treatment corrected abnormal gap junction and hemichannel functions in KID-KCs

Supplementary Materials

Supplementary Methods

Immunostaining

Frozen tissue sections (6 μm) or paraformaldehyde-fixed cultured cells were incubated in PBS containing 3% fetal bovine serum and 0.3% Triton X-100 for 20 min at room temperature, and then incubated overnight at 4°C with a monoclonal Cx26 antibody (1:50; Thermo Fisher Scientific; Cat. #13-8100). Following several rinses with PBS, samples were incubated with a biotinylated secondary antibody (1:100; Vector Laboratories, Peterborough, UK) for 1 hr prior to visualization using an Alexa-Fluor 488- or 568-conjugated streptavidin (1:500; Invitrogen, Paisley, UK). Samples were counterstained with 5 μg/ml 4,6-diamino-2-phenylindole (DAPI, Vector Laboratories, Peterborough, UK), mounted using 10% Mowiol (Calbiochem, Nottingham, UK), and imaged using a Zeiss LSM 510 laser confocal microscope (Zeiss, Oberkochen, Germany). Images were recorded under the same settings (laser power, digital offset and gain) from three to seven continuous, non-overlapping fields on each slide, and analyzed using ImageJ v1.51n (NIH, Bethesda, MD, USA).

siRNAs

Nineteen candidate AS-siRNAs (S1−S19) were designed and synthesized (Sigma, Dorset, UK). In siRNA screening experiments, the Silencer™ siRNA against GFP (Thermo Fisher Scientific, Paisley, UK) was used as a positive control (i.e. indicator of transfection and knockdown efficiency) and the siRNA against human *HAS2* was used as a negative control (si-cont, Sigma, Dorset, UK).

The sequences of si-cont are: sense 5'-AUAUCGUCAUGGUCUUCAU[dT][dT]-3', and antisense 5'-AUGAAGACCAUGACGAUAU [dT][dT]-3'.

Screening of AS-siRNAs

A fluorescence-based screening system was generated using HeLa cells stably expressing ectopic *GJB2-WT* or *GJB2-c.148G>A* which was fused to *GFP* cDNA at the 3'-terminus, driven by the cytomegalovirus promoter (*CMV*) **(Supplementary Figure S4)**. We used the HIV-1 derived, self-inactivating lentiviral vector pLNT-SFFV-MCS, with the WT or mutant *CMV-GJB2-GFP* cDNA sequence subcloned in. Lentiviruses were packaged by co-transfecting HEK-293T cells with the WT or mutant lentiviral vector, together with a plasmid encoding the vesicular stomatitis virus envelope and a packaging plasmid pCMV8.74 coding for lentiviral *gag*, *pol* and accessory proteins, *tat* and *rev*. Infectious viruses were harvested 72 hrs post-transfection, filtered through a 0.45-μm pore cellulose acetate filter, and then ultra-centrifuged at 23,000 × g for 2 hrs. Concentrated viruses were resuspended in the Opti-MEM® medium and the lentivirus stocks were kept at -80°C until use. The viral titres assessed by GFP expression using flow cytometry were 8.8×10^7 infectious unit (IU)/ml for WT viruses and 4.9×10^6 IU/ml for mutant viruses. HeLa cells were transduced with either WT or mutant lentiviruses and, upon confluence being reached, fluorescence-activated cell sorting was carried out to obtain single GFP^+ cells using a Moflo XDP flow cytometer (Beckman Coulter, Luton, UK). These single cells were cultured until clonal expansion was observed.

GFP^+ clonal HeLa cells were seeded in a 24-well plate and, upon reaching a 70% confluence, were transiently transfected with each AS-siRNA at a concentration of 50 nM, using Lipofectamine™ RNAiMAX (Thermo Fisher Scientific, Paisley, UK). 24 hrs post-transfection, the level of *GJB2-GFP* expression was assessed using flow cytometry (FACSCalibur™, BD Biosciences, Oxon, UK).

Briefly, a non-fixed cell suspension was prepared in PBS containing 2% fetal bovine serum. 10,000 cells from each sample were acquired using the FL1 channel with a 530-nm emission filter. Data were analyzed using the FlowJo software v10 (Tree Star Inc., Oregon, USA) and knockdown efficiency was indicated by the decrease of mean GFP intensity (I) in transfected cells, calculated as: $[1- (I_{\text{allele-specific siRNA}} / I_{\text{control siRNA}})] \times 100\%$.

Quantitative reverse transcriptase-PCR (qRT-PCR)

Total RNA was extracted from cells using TRIzol® reagent (Thermo Fisher Scientific, Paisley, UK). Complementary DNAs (cDNAs) were generated using the GeneAmp® RNA PCR Core Kit (Applied Biosystems, Warrington, UK). qRT-PCR was carried out using iTaq™ universal SYBR Green Supermix (Bio-Rad, Watford, UK). All primers used (including the c.148G>A allele-specific primers) are listed in **Supplementary Table S1**. The reactions were performed in triplicate on a C1000™ Thermal Cycler (Bio-Rad, Watford, UK) with conditions as follows: initial denaturation at 95°C for 1 min, followed by 39 thermocycles of 95°C for 15 s and 60°C for 30 s. Individual levels were normalized to *GAPDH* expression. qRT-PCR data were collected and analyzed using CFX-3.1 (Bio-Rad, Watford, UK) and relative expression of *GJB2* was calculated using the $2^{-\Delta\Delta Ct}$ method.

Immunoprecipitation and immunoblotting

Cells were cultured in a 100-mm dish to confluence, washed twice in PBS, and lysed using an immunoprecipitation (IP) lysis buffer containing 10 mM Tris-HCl (pH 7.4), 150 mM NaCl, 1% Triton X-100, 0.5% NP-40, 1 mM EDTA, 1 mM EGTA, 1 mM PMSF supplemented with protease inhibitor cocktail. The lysates were incubated on ice for 15 min with occasional vortexing, and then

centrifuged at 12,000 × g at 4°C for 10 min. 1−1.5 mg protein from the supernatant was transferred to a fresh tube. 0.75 μg of a polyclonal Cx26 antibody (Thermo Fisher Scientific, Paisley, UK, Cat. #71-0500) was added to the lysate and incubated at 4°C for 2.5 hrs. Protein G-Sepharose beads (GE Healthcare, Buckinghamshire, UK) of a 50% slurry was added to the lysate and mixed overnight at 4°C. The beads were harvested by brief centrifugation and washed in IP lysis buffer without detergent. The final pellet was resuspended with a sample buffer containing 125 mM Tris-HCl (pH 6.8), 5% β-mercaptoethanol, 4% sodium dodecyl sulfate (SDS), 10% glycerol and 0.0004% bromophenol blue, and boiled at 95°C for 10 min with brief vortexing to dissociate antigen-antibody complexes from the beads. Samples were briefly centrifuged, and supernatants were analyzed immediately by immunoblotting (IB). The supernatant samples were separately by standard 12% SDS-PAGE in the NuPAGE™ MES SDS running buffer (Thermo Fisher Scientific, Paisley, UK). Membranes were blocked in 5% skimmed milk in PBS and then probed with a monoclonal Cx26 antibody at 1:1000 dilution (Merck Millipore, Watford, UK, Cat. #MABT198). An anti-mouse HRP-conjugated secondary antibody at 1:4000 dilution (GE Healthcare, Buckinghamshire, UK) was used. The target protein was detected using the ECL™ Prime Western Blotting Detection system (Amersham, Buckinghamshire UK). Densitometric analysis was performed on scanned images of blots.

Patch clamp for hemichannel activity

Whole-cell patch clamp was carried out at room temperature as previously described (Levit et al., 2015). Cells were seeded onto 12-mm glass coverslips, which were later transferred to an experimental chamber filled with Tyrode's bath solution containing (in mM): NaCl 137.7, KCl 5.4, NaOH 2.3, $MgCl_2$ 1, glucose 10, and HEPES 5 (pH 7.4). Patch pipettes were pulled from glass

capillaries to a resistance of 3 ─ 6 MΩ with a horizontal puller (P-87, Sutter Instruments, Novato, CA). Pipettes were filled with a solution containing (in mM): K-aspartate 120, HEPES 5, ethylene glycol tetraacetic acid 10, and NaATP 3 (pH 7.2). Solitary cells were measured for membrane capacitance (C_m) and membrane currents (I_m) invoked while the membrane potential was stepped from -110 mV to +110 mV in 20 mV increments. Voltage and current signals were recorded using an Axopatch-1D patch clamp amplifier coupled to a Digidata 1322A interface (Axon Instruments, Foster City, CA). Data were acquired and analyzed using Clampex 9.2 and Clampfit 10.2 software (Axon instruments), respectively. To control for variability in size of recorded cells, membrane current density (I_m/C_m) was used as a direct measure of hemichannel activity. Comparison was made between current density at individual membrane voltages.

Neurobiotin uptake assay for hemichannel activity

The method was modified from a protocol described previously (Mese et al., 2011). Cells plated at a low density were gently washed twice with Ca^{2+}, Mg^{2+}-containing Hank's balanced salt solution (HBSS, Thermo Fisher Scientific, Paisley, UK), and then incubated in 0.1 mg/ml neurobiotin (Vector Laboratories, Peterborough, UK), a non-fluorescent tracer, in divalent-free HBSS at 37°C for 10 min to allow uptake of neurobiotin through open hemichannels. After two washes in Ca^{2+}, Mg^{2+}-containing HBSS, cells were fixed with 4% paraformaldehyde in PBS at 4°C, permeabilized with 0.3% Triton X-100 (Sigma, Dorset, UK) and then stained with Alexa Fluor 568-streptavidin conjugate at 1:400 dilution (Thermo Fisher Scientific, Paisley, UK) at room temperature. Labelled samples were imaged using an Olympus IX71 inverted fluorescence microscope (Olympus, Essex, UK) with the same exposure time applied to all samples. Five to ten neurobiotin uptake images

from each group were recorded and analyzed using ImageJ v1.51n (NIH, Bethesda, MD, USA), and hemichannel activity was determined by the intensity of intracellular neurobiotin.

SLDT assay for gap junction intercellular communication

The scrape loading dye transfer assay (SLDT) was performed as described previously with minor modifications (Yum et al., 2007). Confluent monolayer cell cultures (24- or 48 hrs post-seeding) were gently rinsed twice with Ca^{2+}, Mg^{2+}-containing HBSS, and then replaced with divalent-free HBSS containing 0.1 mg/ml neurobiotin. Multiple parallel scrape lines were made on the cultures using a sharp scalpel blade, followed by incubation at 37°C for 10 min. Cells were washed twice with Ca^{2+}, Mg^{2+}-containing HBSS, fixed with 4% paraformaldehyde in PBS, and stained as described in the neurobiotin uptake assay section. Stained samples were imaged using an Olympus IX71 inverted fluorescence microscope. At least six scrape-wounded images and three background (non-scrape-wounded) images were recorded from each group. Images were analyzed using ImageJ v1.51n. GJ intercellular communication was determined by the extent of dye transfer, quantified by the total area between the scrape line and the point at which the fluorescence level reduced to 1.5 × the background fluorescence level.

Bio-engineered skin and human-murine chimeric skin graft model

The methods for preparing and grafting bioengineered skin in immunodeficient mice have been described previously (Di et al., 2011). In brief, immortalised KID-KCs at passage 7 were seeded on top of a fibrin matrix populated with live primary fibroblasts (passage 3) isolated from the KID syndrome patient. After keratinocytes reached confluence, the bio-engineered skin constructs were grafted onto the dorsum of 22-week-old NOD-severe combined immunodeficiency mice (NOD scid

gamma [or NSG] mice, Charles River, UK). Three months post-grafting, mice were anesthetized and skin samples from graft area were taken post-mortem, embedded in paraffin and sectioned for histological examination.

RNA sequencing (RNA-Seq) and data analysis

Cultured KID-KCs treated in triplicate with AS-siRNA were subject to RNA-Seq experiments 24 hrs post-treatment and untreated cells were used as a control. RNA was extracted using TRIzol® reagent (Thermo Fisher Scientific, Paisley, UK) and RNA quality was measured using an Agilent Bioanalyser. All samples had an RNA integrity number greater than 9.8. cDNA libraries were prepared using the KAPA mRNA HyperPrep Kit (KAPA Biosystems) according to manufacturers' instructions. The libraries were sequenced with a 43-bp paired-end run using a NextSeq 500 instrument (Illumina, San Diego, US). The sequence reads are available at GEO accession GSE131709.

Data were first demultiplexed and converted to fastq files using bcl2fastq Conversion (v2.19, Illumina). Fastq files were then pre-processed to remove adapter contamination and poor-quality base calls (Q20 or below) using a 5' to 3' sliding window approach. The remaining read data were mapped to the hg38 reference genome using the gapped aligner, RNA-STAR (v2.5b). Read data were counted per transcript by FeatureCounts (v1.4.6p5). Normalization, modelling and differential expression analysis were carried out using the SARTools package (v1.3.2, BioConductor). All reference genomes and annotation were obtained from the Illumina iGenomes repository. Differentially expressed genes were determined using a threshold of p-adj < 0.05 and $|\log_2$ fold change$| \geq 1$ (Speranza et al., 2017).

Supplementary Tables

Supplementary Table S1. Primers

Target	Forward primers (5'-3')	Reverse primers (5'-3')
Total *GJB2*	CTCCCGACGCAGAGCAAA	GGTTGCCTCATCCCTCTCAT
GJB2 WT	CTCCCGACGCAGAGCAAA	GGCTGCAGGGTGTTGCAGACAATGTC
GJB2 mutant	CTCCCGACGCAGAGCAAA	GGCTGCAGGGTGTTGCAGACAATGTT
GAPDH	CCCATCACCATCTTCCAGGA	CCAGTGAGCTTCCCGTTCAGC
MMP1	AAAGGGAATAAGTACTGGGC	CAGTGTTTTCCTCAGAAAGAG
MMP9	AGCTGGCAGAGGAATAC	CCCCAGAGATTTCGACTC
MMP10	ACCAATTTATTCCTCGTTGC	GTCCGTAGAGAGACTGAATG
ANGPTL4	AGGCAGAGTGGACTATTTG	CCTCCATCTGAGGTCATC
CXCL5	ATTTGTCTTGATCCAGAAGC	TCAGTTTTCCTTGTTTCCAC
TMEM109	CTTATCCTCCTCCACTCAG	GACGAAGACTCTGACACC
GPR137	AACCTCTACTTTGCCCAG	GTTCACCAGCAGAAAGAG
AFAP1L1	GGAATGGGAAATGAAGAAGAC	CATATCCCCTAAAATCATGCAG
NSA2	GTAAAGAAGAATCCCTCATCC	GGTAACCTCCCCATATTTTC
GLB1L2	ACTTCAGAATCTATAGCCTGG	CAAGCTACCCAAGAAGAAAG

Supplementary Table S2. List of 180 genes predicted to have seed sequence match with S7

ABCA1	*CRB2*	*IFT88*	*MED13L*	*PLXNB1*	*SLC6A8*
ABCC3	*CREBBP*	*IGF2R*	*MED17*	*PPP4R1*	*SMCR7*
ADAMTS7	*CSPG4*	*IGSF9B*	*MEGF8*	*PPRC1*	*SON*
ADCK4	*CTNNA1*	*INTS10*	*MST1R*	*PRKCQ*	*SPEN*
ADCY1	*CUL9*	*IQGAP3*	*MTF2*	*PRR14L*	*STRBP*
ADCY10	*CYP2S1*	*KANSL2*	*MYO16*	*PRSS21*	*SVIL*
ADH4	*DAGLA*	*KANSL3*	*NAT10*	*PRX*	*SYNE2*
AFP	*DMBT1*	*KAT5*	*NAV3*	*PSD3*	*SZT2*
AGBL1	*DSG2*	*KCNH4*	*NBEAL2*	*PTPRB*	*TAF1*
ANKRD28	*DTNA*	*KCNH5*	*NCOA1*	*RAB11FIP5*	*TAF5L*
APOB	*DZANK1*	*KCNK16*	*NEURL4*	*REG1A*	*TBCD*
ARHGAP44	*EDC4*	*KDR*	*NLRC5*	*RINT1*	*TEK*
ASH1L	*ERN1*	*KIAA0556*	*NLRP8*	*RNF17*	*TENM1*
ATP13A1	*ESPL1*	*KIAA1671*	*NOD1*	*RREB1*	*TENM4*
BCAN	*FBXW2*	*KIAA1755*	*NOS2*	*RTTN*	*TEP1*
BIRC6	*FCGBP*	*KIDINS220*	*OCA2*	*RYR3*	*TLE2*
BPIFB4	*FLT1*	*KNTC1*	*OR51E1*	*SCN2A*	*TLR8*
C12orf55	*FOCAD*	*LAMA1*	*PCDH19*	*SCN3A*	*TMPRSS4*
C12orf63	*FRAS1*	*LAP3*	*PCDHB13*	*SEC23A*	*TRAK2*
C16orf62	*GALNT8*	*LIM2*	*PCDHB16*	*SEC31B*	*TRIM60*
C5	*GJA10*	*LLGL2*	*PCDHGA6*	*SEMA4A*	*TTC3*
C6orf132	*GNRHR*	*LOC101929274*	*PCNXL3*	*SLC12A1*	*TUBGCP6*
CACNA1B	*GPR112*	*LOC400499*	*PI4KA*	*SLC26A6*	*UNC13A*
CAND2	***GPR137***	*LRP1B*	*PIGV*	*SLC30A5*	*URB1*
CDS2	*GRM3*	*LTBP4*	*PIWIL2*	*SLC35B1*	*UTRN*
CNOT1	*GRM8*	*LTN1*	*PKD1*	*SLC37A2*	*VPS13D*
COL15A1	*GSG2*	*LY75*	*PKHD1*	*SLC44A3*	*VWF*
COL20A1	*GTPBP2*	*LY75-CD302*	*PLCB3*	*SLC45A3*	*WNK2*
COL4A2	*HLCS*	*MAGEL2*	*PLEKHG2*	*SLC4A4*	*WRN*
COPA	*HLTF*	*MAP7*	*PLEKHM2*	*SLC5A9*	*ZSWIM8*

*Among the 180 genes, only *GPR137* (underlined, bolded) was found in the top five up- or downregulated genes in KID-KCs treated by S7

Supplementary Figures

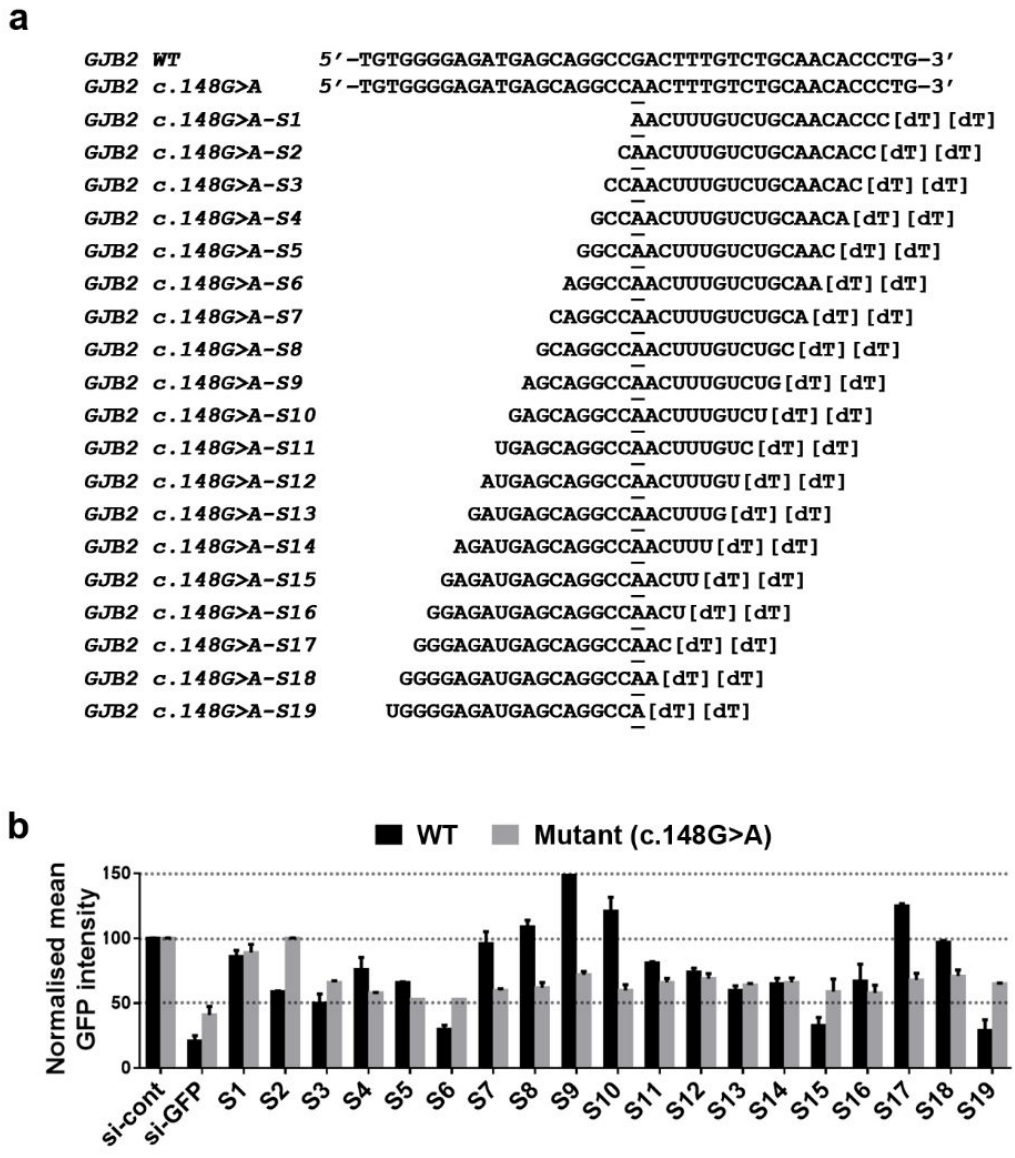

Supplementary Figure S1. AS-siRNAs: design and screening

19 AS-siRNAs (with a 19-nt targeting sequence plus a deoxythymidine dinucleotide) were designed and designated *GJB2* c.148G>A_S1−S19 (or S1−S19 in short form). WT and mutant *GJB2* sequences are shown and aligned with the siRNAs, with c.148G>A mutation underlined (a). Fluorescence-based screening results of the 19 AS-siRNAs in HeLa cells expressing WT or mutant

GJB2-GFP fusion transgene are shown (b). The GFP siRNA (si-GFP) and the irrelevant siRNA (si-cont) were used as positive and negative controls, respectively. The *GJB2* knockdown efficiency of the AS-siRNAs was determined by the decrease in GFP intensity detected by flow cytometry (n = 3). The lead AS-siRNA, S7, inhibited the mutant *GJB2* potently and specifically, but did not inhibit the WT *GJB2*. Data are normalized to the levels from cells treated with si-cont and shown as mean ± SEM.

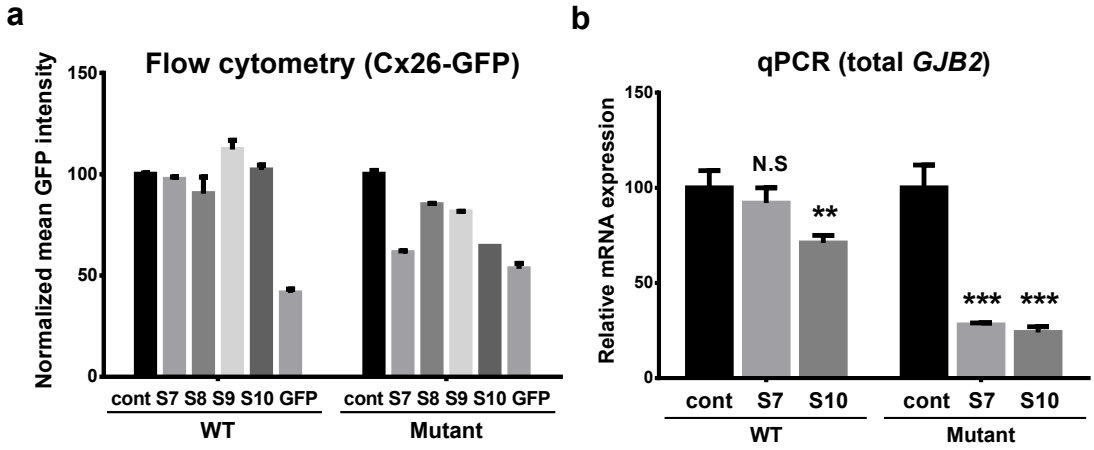

Supplementary Figure S2. Validation of AS-siRNA screening suggested potent and mutation-specific inhibitory activity of S7

HeLa cells treated with 50 nM AS-siRNA (S7-S10), si-cont (cont), or si-GFP (GFP) were examined for Cx26-GFP protein expression using flow cytometry (a) and for total *GJB2* mRNA using qRT-PCR (b). Mutant-specific inhibition was achieved by S7 and S10 (a). These two siRNAs were further tested at mRNA level and non-specific inhibition of wildtype (WT) *GJB2* was detected in cells treated with S10, but not in those treated with S7 (b). N.S, not significant; $^{**}p < 0.01$; $^{*}p < 0.001$.

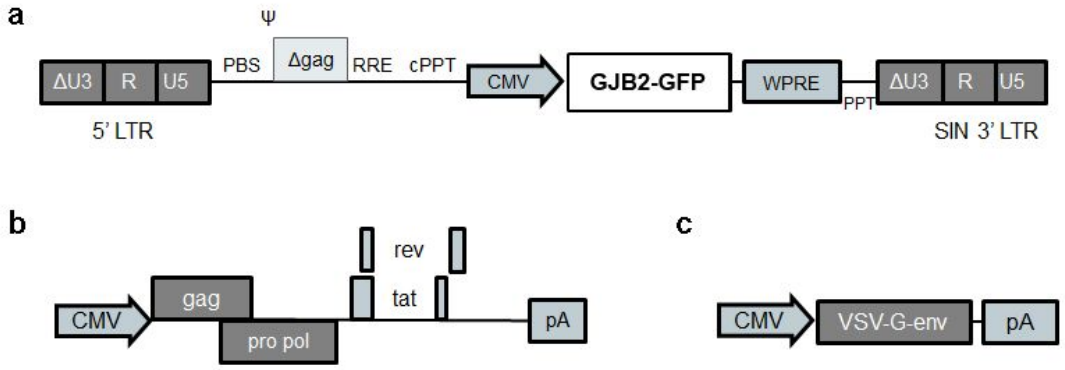

Supplementary Figure S3. Schematic of the LNT-*CMV-GJB2-GFP* lentiviral vectors

Panel a shows the self-inactivating, HIV-1-based vector with the transgene cloned in, which encodes the wildtype or c.148G>A mutant *GJB2* cDNA fused to *GFP* reporter cDNA at the 3' terminus driven by the cytomegalovirus promoter (*CMV*). Panel b shows the packaging plasmid containing *gag*, *pol*, *rev* and *tat* genes and panel c shows the envelope plasmid. LTR, long terminal repeat. PBS, tRNA primer binding site. RRE, rev response elements. VSV-G env, envelope pseudotyped with the G glycoprotein of vesicular stomatitis virus. cPPT, central polypurine tract. WPRE, woodchuck hepatitis virus post-transcriptional regulatory element.

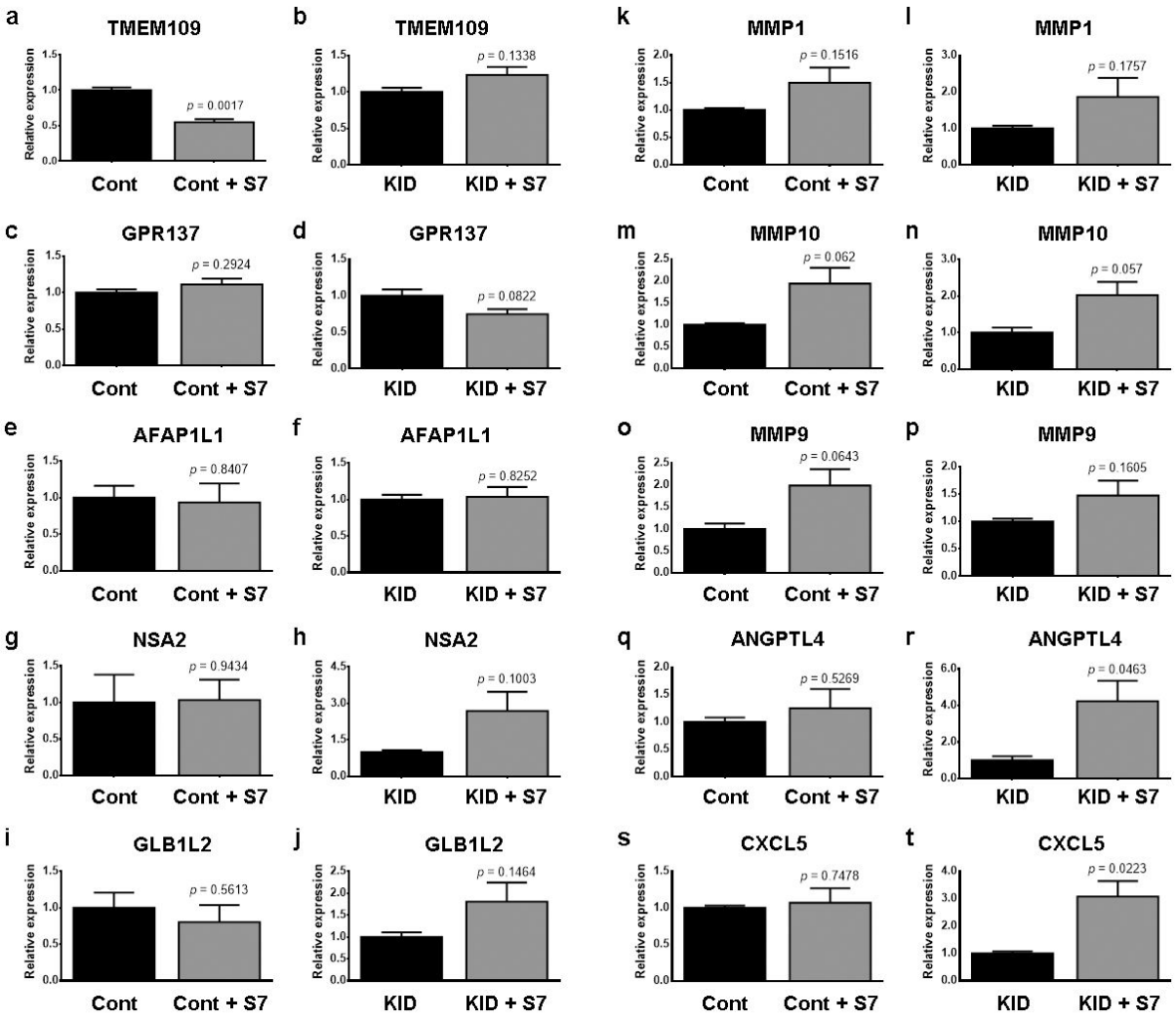

Supplementary Figure S4. Validation of the RNA-Seq data using qRT-PCR

RNA extracted from Control-KCs (Cont) and KID-KCs (KID) with or without treated S7 treatment were subjected to qRT-PCR using primers specific to the top 5 upregulated and 5 downregulated genes from the RNA-Seq analysis. The expression levels were calibrated by the internal control *GAPDH* gene. Data are represented as mean ± SEM and analyzed statistically using Student's *t*-test (n = 3).

REFERENCES

Di WL, Larcher F, Semenova E, Talbot GE, Harper JI, Del Rio M, et al. Ex-vivo gene therapy restores LEKTI activity and corrects the architecture of Netherton syndrome-derived skin grafts. Mol Ther 2011; 19: 408-16.

Levit NA, Sellitto C, Wang HZ, Li L, Srinivas M, Brink PR, et al. Aberrant connexin26 hemichannels underlying keratitis-ichthyosis-deafness syndrome are potently inhibited by mefloquine. J Invest Dermatol 2015; 135: 1033-42.

Mese G, Sellitto C, Li L, Wang HZ, Valiunas V, Richard G, et al. The Cx26-G45E mutation displays increased hemichannel activity in a mouse model of the lethal form of keratitis-ichthyosis-deafness syndrome. Mol Biol Cell 2011; 22: 4776-86.

Speranza E, Altamura LA, Kulcsar K, Bixler SL, Rossi CA, Schoepp RJ, et al. Comparison of transcriptomic platforms for analysis of whole blood from Ebola-infected cynomolgus macaques. Sci Rep 2017; 7: 14756.

Yum SW, Zhang J, Valiunas V, Kanaporis G, Brink PR, White TW. Human connexin26 and connexin30 form functional heteromeric and heterotypic channels. Am J Physiol Cell Physiol 2007; 293: C1032-48.

Supplementary Methods

Immunostaining

Frozen tissue sections (6 μm) or paraformaldehyde-fixed cultured cells were incubated in PBS containing 3% fetal bovine serum and 0.3% Triton X-100 for 20 min at room temperature, and then incubated overnight at 4°C with a monoclonal Cx26 antibody (1:50; Thermo Fisher Scientific; Cat. #13-8100). Following several rinses with PBS, samples were incubated with a biotinylated secondary antibody (1:100; Vector Laboratories, Peterborough, UK) for 1 hr prior to visualization using an Alexa-Fluor 488- or 568-conjugated streptavidin (1:500; Invitrogen, Paisley, UK). Samples were counterstained with 5 μg/ml 4,6-diamino-2-phenylindole (DAPI, Vector Laboratories, Peterborough, UK), mounted using 10% Mowiol (Calbiochem, Nottingham, UK), and imaged using a Zeiss LSM 510 laser confocal microscope (Zeiss, Oberkochen, Germany). Images were recorded under the same settings (laser power, digital offset and gain) from three to seven continuous, non-overlapping fields on each slide, and analyzed using ImageJ v1.51n (NIH, Bethesda, MD, USA).

siRNAs

Nineteen candidate AS-siRNAs (S1−S19) were designed and synthesized (Sigma, Dorset, UK). In siRNA screening experiments, the Silencer™ siRNA against GFP (Thermo Fisher Scientific, Paisley, UK) was used as a positive control (i.e. indicator of transfection and knockdown efficiency) and the siRNA against human *HAS2* was used as a negative control (si-cont, Sigma, Dorset, UK). The sequences of si-cont are: sense 5'-AUAUCGUCAUGGUCUUCAU[dT][dT]-3', and antisense 5'-AUGAAGACCAUGACGAUAU [dT][dT]-3'.

Screening of AS-siRNAs

A fluorescence-based screening system was generated using HeLa cells stably expressing ectopic *GJB2-WT* or *GJB2-c.148G>A* which was fused to *GFP* cDNA at the 3'-terminus, driven by the cytomegalovirus promoter (*CMV*) **(Supplementary Figure S4)**. We used the HIV-1 derived, self-inactivating lentiviral vector pLNT-SFFV-MCS, with the WT or mutant *CMV-GJB2-GFP* cDNA sequence subcloned in. Lentiviruses were packaged by co-transfecting HEK-293T cells with the WT or mutant lentiviral vector, together with a plasmid encoding the vesicular stomatitis virus envelope and a packaging plasmid pCMV8.74 coding for lentiviral *gag*, *pol* and accessory proteins, *tat* and *rev*. Infectious viruses were harvested 72 hrs post-transfection, filtered through a 0.45-μm pore cellulose acetate filter, and then ultra-centrifuged at 23,000 × g for 2 hrs. Concentrated viruses were resuspended in the Opti-MEM® medium and the lentivirus stocks were kept at -80°C until use. The viral titres assessed by GFP expression using flow cytometry were 8.8×10^7 infectious unit (IU)/ml for WT viruses and 4.9×10^6 IU/ml for mutant viruses. HeLa cells were transduced with either WT or mutant lentiviruses and, upon confluence being reached, fluorescence-activated cell sorting was carried out to obtain single GFP^+ cells using a Moflo XDP flow cytometer (Beckman Coulter, Luton, UK). These single cells were cultured until clonal expansion was observed.

GFP^+ clonal HeLa cells were seeded in a 24-well plate and, upon reaching a 70% confluence, were transiently transfected with each AS-siRNA at a concentration of 50 nM, using Lipofectamine™ RNAiMAX (Thermo Fisher Scientific, Paisley, UK). 24 hrs post-transfection, the level of *GJB2-GFP* expression was assessed using flow cytometry (FACSCalibur™, BD Biosciences, Oxon, UK). Briefly, a non-fixed cell suspension was prepared in PBS containing 2% fetal bovine serum. 10,000 cells from each sample were acquired using the FL1 channel with a 530-nm emission filter. Data were analyzed using the FlowJo software v10 (Tree Star Inc., Oregon, USA) and knockdown

efficiency was indicated by the decrease of mean GFP intensity (I) in transfected cells, calculated as: $[1- (I_{\text{allele-specific siRNA}} / I_{\text{control siRNA}})] \times 100\%$.

Quantitative reverse transcriptase-PCR (qRT-PCR)

Total RNA was extracted from cells using TRIzol® reagent (Thermo Fisher Scientific, Paisley, UK). Complementary DNAs (cDNAs) were generated using the GeneAmp® RNA PCR Core Kit (Applied Biosystems, Warrington, UK). qRT-PCR was carried out using iTaq™ universal SYBR Green Supermix (Bio-Rad, Watford, UK). All primers used (including the c.148G>A allele-specific primers) are listed in **Supplementary Table S1**. The reactions were performed in triplicate on a C1000™ Thermal Cycler (Bio-Rad, Watford, UK) with conditions as follows: initial denaturation at 95°C for 1 min, followed by 39 thermocycles of 95°C for 15 s and 60°C for 30 s. Individual levels were normalized to *GAPDH* expression. qRT-PCR data were collected and analyzed using CFX-3.1 (Bio-Rad, Watford, UK) and relative expression of *GJB2* was calculated using the $2^{-\Delta\Delta Ct}$ method.

Immunoprecipitation and immunoblotting

Cells were cultured in a 100-mm dish to confluence, washed twice in PBS, and lysed using an immunoprecipitation (IP) lysis buffer containing 10 mM Tris-HCl (pH 7.4), 150 mM NaCl, 1% Triton X-100, 0.5% NP-40, 1 mM EDTA, 1 mM EGTA, 1 mM PMSF supplemented with protease inhibitor cocktail. The lysates were incubated on ice for 15 min with occasional vortexing, and then centrifuged at 12,000 × g at 4°C for 10 min. 1−1.5 mg protein from the supernatant was transferred to a fresh tube. 0.75 μg of a polyclonal Cx26 antibody (Thermo Fisher Scientific, Paisley, UK, Cat. #71-0500) was added to the lysate and incubated at 4°C for 2.5 hrs. Protein G-Sepharose beads (GE

Healthcare, Buckinghamshire, UK) of a 50% slurry was added to the lysate and mixed overnight at 4°C. The beads were harvested by brief centrifugation and washed in IP lysis buffer without detergent. The final pellet was resuspended with a sample buffer containing 125 mM Tris-HCl (pH 6.8), 5% β-mercaptoethanol, 4% sodium dodecyl sulfate (SDS), 10% glycerol and 0.0004% bromophenol blue, and boiled at 95°C for 10 min with brief vortexing to dissociate antigen-antibody complexes from the beads. Samples were briefly centrifuged, and supernatants were analyzed immediately by immunoblotting (IB). The supernatant samples were separately by standard 12% SDS-PAGE in the NuPAGE™ MES SDS running buffer (Thermo Fisher Scientific, Paisley, UK). Membranes were blocked in 5% skimmed milk in PBS and then probed with a monoclonal Cx26 antibody at 1:1000 dilution (Merck Millipore, Watford, UK, Cat. #MABT198). An anti-mouse HRP-conjugated secondary antibody at 1:4000 dilution (GE Healthcare, Buckinghamshire, UK) was used. The target protein was detected using the ECL™ Prime Western Blotting Detection system (Amersham, Buckinghamshire UK). Densitometric analysis was performed on scanned images of blots.

Patch clamp for hemichannel activity

Whole-cell patch clamp was carried out at room temperature as previously described (Levit et al., 2015). Cells were seeded onto 12-mm glass coverslips, which were later transferred to an experimental chamber filled with Tyrode's bath solution containing (in mM): NaCl 137.7, KCl 5.4, NaOH 2.3, $MgCl_2$ 1, glucose 10, and HEPES 5 (pH 7.4). Patch pipettes were pulled from glass capillaries to a resistance of 3 ─ 6 MΩ with a horizontal puller (P-87, Sutter Instruments, Novato, CA). Pipettes were filled with a solution containing (in mM): K-aspartate 120, HEPES 5, ethylene glycol tetraacetic acid 10, and NaATP 3 (pH 7.2). Solitary cells were measured for membrane

capacitance (C_m) and membrane currents (I_m) invoked while the membrane potential was stepped from -110 mV to +110 mV in 20 mV increments. Voltage and current signals were recorded using an Axopatch-1D patch clamp amplifier coupled to a Digidata 1322A interface (Axon Instruments, Foster City, CA). Data were acquired and analyzed using Clampex 9.2 and Clampfit 10.2 software (Axon instruments), respectively. To control for variability in size of recorded cells, membrane current density (I_m/C_m) was used as a direct measure of hemichannel activity. Comparison was made between current density at individual membrane voltages.

Neurobiotin uptake assay for hemichannel activity

The method was modified from a protocol described previously (Mese et al., 2011). Cells plated at a low density were gently washed twice with Ca^{2+}, Mg^{2+}-containing Hank's balanced salt solution (HBSS, Thermo Fisher Scientific, Paisley, UK), and then incubated in 0.1 mg/ml neurobiotin (Vector Laboratories, Peterborough, UK), a non-fluorescent tracer, in divalent-free HBSS at 37°C for 10 min to allow uptake of neurobiotin through open hemichannels. After two washes in Ca^{2+}, Mg^{2+}-containing HBSS, cells were fixed with 4% paraformaldehyde in PBS at 4°C, permeabilized with 0.3% Triton X-100 (Sigma, Dorset, UK) and then stained with Alexa Fluor 568-streptavidin conjugate at 1:400 dilution (Thermo Fisher Scientific, Paisley, UK) at room temperature. Labelled samples were imaged using an Olympus IX71 inverted fluorescence microscope (Olympus, Essex, UK) with the same exposure time applied to all samples. Five to ten neurobiotin uptake images from each group were recorded and analyzed using ImageJ v1.51n (NIH, Bethesda, MD, USA), and hemichannel activity was determined by the intensity of intracellular neurobiotin.

SLDT assay for gap junction intercellular communication

The scrape loading dye transfer assay (SLDT) was performed as described previously with minor modifications (Yum et al., 2007). Confluent monolayer cell cultures (24- or 48 hrs post-seeding) were gently rinsed twice with Ca^{2+}, Mg^{2+}-containing HBSS, and then replaced with divalent-free HBSS containing 0.1 mg/ml neurobiotin. Multiple parallel scrape lines were made on the cultures using a sharp scalpel blade, followed by incubation at 37°C for 10 min. Cells were washed twice with Ca^{2+}, Mg^{2+}-containing HBSS, fixed with 4% paraformaldehyde in PBS, and stained as described in the neurobiotin uptake assay section. Stained samples were imaged using an Olympus IX71 inverted fluorescence microscope. At least six scrape-wounded images and three background (non-scrape-wounded) images were recorded from each group. Images were analyzed using ImageJ v1.51n. GJ intercellular communication was determined by the extent of dye transfer, quantified by the total area between the scrape line and the point at which the fluorescence level reduced to 1.5 × the background fluorescence level.

Bio-engineered skin and human-murine chimeric skin graft model

The methods for preparing and grafting bioengineered skin in immunodeficient mice have been described previously (Di et al., 2011). In brief, immortalised KID-KCs at passage 7 were seeded on top of a fibrin matrix populated with live primary fibroblasts (passage 3) isolated from the KID syndrome patient. After keratinocytes reached confluence, the bio-engineered skin constructs were grafted onto the dorsum of 22-week-old NOD-severe combined immunodeficiency mice (NOD scid gamma [or NSG] mice, Charles River, UK). Three months post-grafting, mice were anesthetized and skin samples from graft area were taken post-mortem, embedded in paraffin and sectioned for histological examination.

RNA sequencing (RNA-Seq) and data analysis

Cultured KID-KCs treated in triplicate with AS-siRNA were subject to RNA-Seq experiments 24 hrs post-treatment and untreated cells were used as a control. RNA was extracted using TRIzol® reagent (Thermo Fisher Scientific, Paisley, UK) and RNA quality was measured using an Agilent Bioanalyser. All samples had an RNA integrity number greater than 9.8. cDNA libraries were prepared using the KAPA mRNA HyperPrep Kit (KAPA Biosystems) according to manufacturers' instructions. The libraries were sequenced with a 43-bp paired-end run using a NextSeq 500 instrument (Illumina, San Diego, US). The sequence reads are available at GEO accession GSE131709.

Data were first demultiplexed and converted to fastq files using bcl2fastq Conversion (v2.19, Illumina). Fastq files were then pre-processed to remove adapter contamination and poor-quality base calls (Q20 or below) using a 5' to 3' sliding window approach. The remaining read data were mapped to the hg38 reference genome using the gapped aligner, RNA-STAR (v2.5b). Read data were counted per transcript by FeatureCounts (v1.4.6p5). Normalization, modelling and differential expression analysis were carried out using the SARTools package (v1.3.2, BioConductor). All reference genomes and annotation were obtained from the Illumina iGenomes repository. Differentially expressed genes were determined using a threshold of p-adj < 0.05 and $|\log_2$ fold change$| \geq 1$ (Speranza et al., 2017).

REFERENCES

Di WL, Larcher F, Semenova E, Talbot GE, Harper JI, Del Rio M, et al. Ex-vivo gene therapy restores LEKTI activity and corrects the architecture of Netherton syndrome-derived skin grafts. Mol Ther 2011; 19: 408-16.

Levit NA, Sellitto C, Wang HZ, Li L, Srinivas M, Brink PR, et al. Aberrant connexin26 hemichannels underlying keratitis-ichthyosis-deafness syndrome are potently inhibited by mefloquine. J Invest Dermatol 2015; 135: 1033-42.

Mese G, Sellitto C, Li L, Wang HZ, Valiunas V, Richard G, et al. The Cx26-G45E mutation displays increased hemichannel activity in a mouse model of the lethal form of keratitis-ichthyosis-deafness syndrome. Mol Biol Cell 2011; 22: 4776-86.

Speranza E, Altamura LA, Kulcsar K, Bixler SL, Rossi CA, Schoepp RJ, et al. Comparison of transcriptomic platforms for analysis of whole blood from Ebola-infected cynomolgus macaques. Sci Rep 2017; 7: 14756.

Yum SW, Zhang J, Valiunas V, Kanaporis G, Brink PR, White TW. Human connexin26 and connexin30 form functional heteromeric and heterotypic channels. Am J Physiol Cell Physiol 2007; 293: C1032-48.

Supplementary Table S1. Primers

Target	Forward primers (5'-3')	Reverse primers (5'-3')
Total *GJB2*	CTCCCGACGCAGAGCAAA	GGTTGCCTCATCCCTCTCAT
GJB2 WT	CTCCCGACGCAGAGCAAA	GGCTGCAGGGTGTTGCAGACAATGTC
GJB2 mutant	CTCCCGACGCAGAGCAAA	GGCTGCAGGGTGTTGCAGACAATGTT
GAPDH	CCCATCACCATCTTCCAGGA	CCAGTGAGCTTCCCGTTCAGC
MMP1	AAAGGGAATAAGTACTGGGC	CAGTGTTTTCCTCAGAAAGAG
MMP9	AGCTGGCAGAGGAATAC	CCCCAGAGATTTCGACTC
MMP10	ACCAATTTATTCCTCGTTGC	GTCCGTAGAGAGACTGAATG
ANGPTL4	AGGCAGAGTGGACTATTTG	CCTCCATCTGAGGTCATC
CXCL5	ATTTGTCTTGATCCAGAAGC	TCAGTTTTCCTTGTTTCCAC
TMEM109	CTTATCCTCCTCCACTCAG	GACGAAGACTCTGACACC
GPR137	AACCTCTACTTTGCCCAG	GTTCACCAGCAGAAAGAG
AFAP1L1	GGAATGGGAAATGAAGAAGAC	CATATCCCCTAAAATCATGCAG
NSA2	GTAAAGAAGAATCCCTCATCC	GGTAACCTCCCCATATTTTC
GLB1L2	ACTTCAGAATCTATAGCCTGG	CAAGCTACCCAAGAAGAAAG

Supplementary Table S2. List of 180 genes predicted to have seed sequence match with S7

ABCA1	*CRB2*	*IFT88*	*MED13L*	*PLXNB1*	*SLC6A8*
ABCC3	*CREBBP*	*IGF2R*	*MED17*	*PPP4R1*	*SMCR7*
ADAMTS7	*CSPG4*	*IGSF9B*	*MEGF8*	*PPRC1*	*SON*
ADCK4	*CTNNA1*	*INTS10*	*MST1R*	*PRKCQ*	*SPEN*
ADCY1	*CUL9*	*IQGAP3*	*MTF2*	*PRR14L*	*STRBP*
ADCY10	*CYP2S1*	*KANSL2*	*MYO16*	*PRSS21*	*SVIL*
ADH4	*DAGLA*	*KANSL3*	*NAT10*	*PRX*	*SYNE2*
AFP	*DMBT1*	*KAT5*	*NAV3*	*PSD3*	*SZT2*
AGBL1	*DSG2*	*KCNH4*	*NBEAL2*	*PTPRB*	*TAF1*
ANKRD28	*DTNA*	*KCNH5*	*NCOA1*	*RAB11FIP5*	*TAF5L*
APOB	*DZANK1*	*KCNK16*	*NEURL4*	*REG1A*	*TBCD*
ARHGAP44	*EDC4*	*KDR*	*NLRC5*	*RINT1*	*TEK*
ASH1L	*ERN1*	*KIAA0556*	*NLRP8*	*RNF17*	*TENM1*
ATP13A1	*ESPL1*	*KIAA1671*	*NOD1*	*RREB1*	*TENM4*
BCAN	*FBXW2*	*KIAA1755*	*NOS2*	*RTTN*	*TEP1*
BIRC6	*FCGBP*	*KIDINS220*	*OCA2*	*RYR3*	*TLE2*
BPIFB4	*FLT1*	*KNTC1*	*OR51E1*	*SCN2A*	*TLR8*
C12orf55	*FOCAD*	*LAMA1*	*PCDH19*	*SCN3A*	*TMPRSS4*
C12orf63	*FRAS1*	*LAP3*	*PCDHB13*	*SEC23A*	*TRAK2*
C16orf62	*GALNT8*	*LIM2*	*PCDHB16*	*SEC31B*	*TRIM60*
C5	*GJA10*	*LLGL2*	*PCDHGA6*	*SEMA4A*	*TTC3*
C6orf132	*GNRHR*	*LOC101929274*	*PCNXL3*	*SLC12A1*	*TUBGCP6*
CACNA1B	*GPR112*	*LOC400499*	*PI4KA*	*SLC26A6*	*UNC13A*
CAND2	***GPR137***	*LRP1B*	*PIGV*	*SLC30A5*	*URB1*
CDS2	*GRM3*	*LTBP4*	*PIWIL2*	*SLC35B1*	*UTRN*
CNOT1	*GRM8*	*LTN1*	*PKD1*	*SLC37A2*	*VPS13D*
COL15A1	*GSG2*	*LY75*	*PKHD1*	*SLC44A3*	*VWF*
COL20A1	*GTPBP2*	*LY75-CD302*	*PLCB3*	*SLC45A3*	*WNK2*
COL4A2	*HLCS*	*MAGEL2*	*PLEKHG2*	*SLC4A4*	*WRN*
COPA	*HLTF*	*MAP7*	*PLEKHM2*	*SLC5A9*	*ZSWIM8*

*Among the 180 genes, only *GPR137* (underlined, bolded) was found in the top five up- or downregulated genes in KID-KCs treated by S7

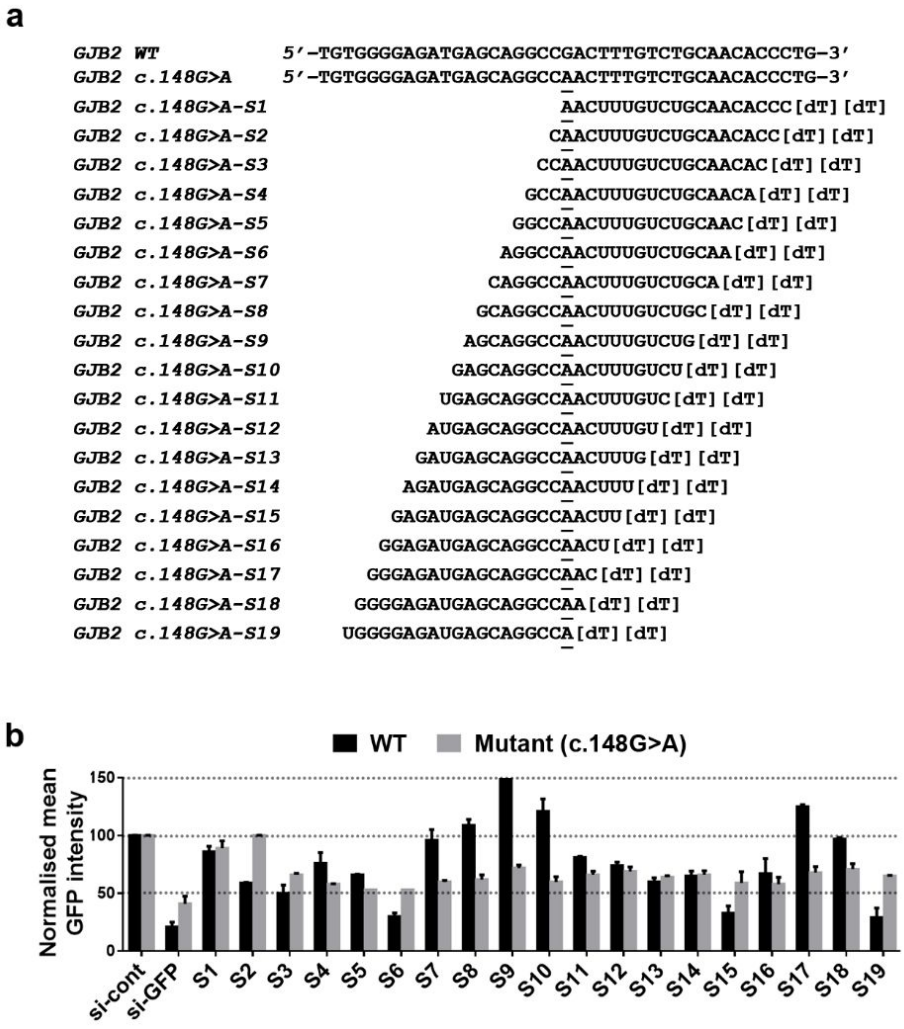

Supplementary Figure S1. AS-siRNAs: design and screening

19 AS-siRNAs (with a 19-nt targeting sequence plus a deoxythymidine dinucleotide) were designed and designated *GJB2* c.148G>A_S1−S19 (or S1−S19 in short form). WT and mutant *GJB2* sequences are shown and aligned with the siRNAs, with c.148G>A mutation underlined (a). Fluorescence-based screening results of the 19 AS-siRNAs in HeLa cells expressing WT or mutant *GJB2-GFP* fusion transgene are shown (b). The GFP siRNA (si-GFP) and the irrelevant siRNA (si-cont) were used as positive and negative controls, respectively. The *GJB2* knockdown efficiency of the AS-siRNAs was determined by the decrease in GFP intensity detected by flow cytometry (n = 3). The lead AS-siRNA, S7, inhibited the mutant *GJB2* potently and specifically, but did not inhibit the WT *GJB2*. Data are normalized to the levels from cells treated with si-cont and shown as mean ± SEM.

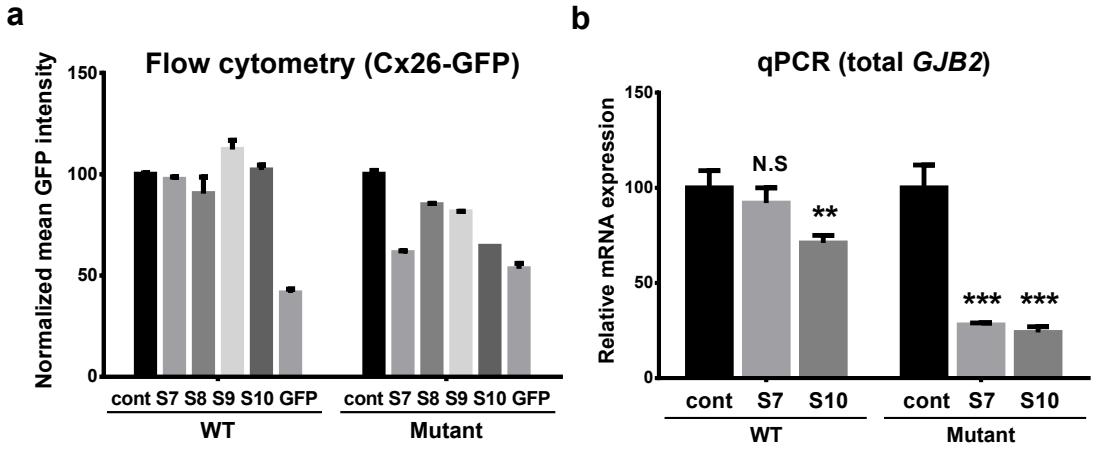

Supplementary Figure S2. Validation of AS-siRNA screening suggested potent and mutation-specific inhibitory activity of S7

HeLa cells treated with 50 nM AS-siRNA (S7-S10), si-cont (cont), or si-GFP (GFP) were examined for Cx26-GFP protein expression using flow cytometry (a) and for total *GJB2* mRNA using qRT-PCR (b). Mutant-specific inhibition was achieved by S7 and S10 (a). These two siRNAs were further tested at mRNA level and non-specific inhibition of wildtype (WT) *GJB2* was detected in cells treated with S10, but not in those treated with S7 (b). N.S, not significant; $^{**}p < 0.01$; $^{*}p < 0.001$.

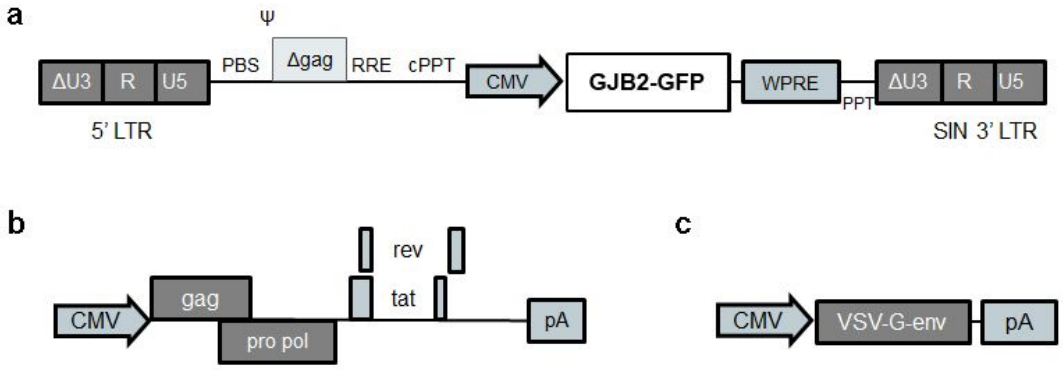

Supplementary Figure S3. Schematic of the LNT-*CMV-GJB2-GFP* lentiviral vectors

Panel a shows the self-inactivating, HIV-1-based vector with the transgene cloned in, which encodes the wildtype or c.148G>A mutant *GJB2* cDNA fused to *GFP* reporter cDNA at the 3' terminus driven by the cytomegalovirus promoter (*CMV*). Panel b shows the packaging plasmid containing *gag*, *pol*, *rev* and *tat* genes and panel c shows the envelope plasmid. LTR, long terminal repeat. PBS, tRNA primer binding site. RRE, rev response elements. VSV-G env, envelope pseudotyped with the G glycoprotein of vesicular stomatitis virus. cPPT, central polypurine tract. WPRE, woodchuck hepatitis virus post-transcriptional regulatory element.

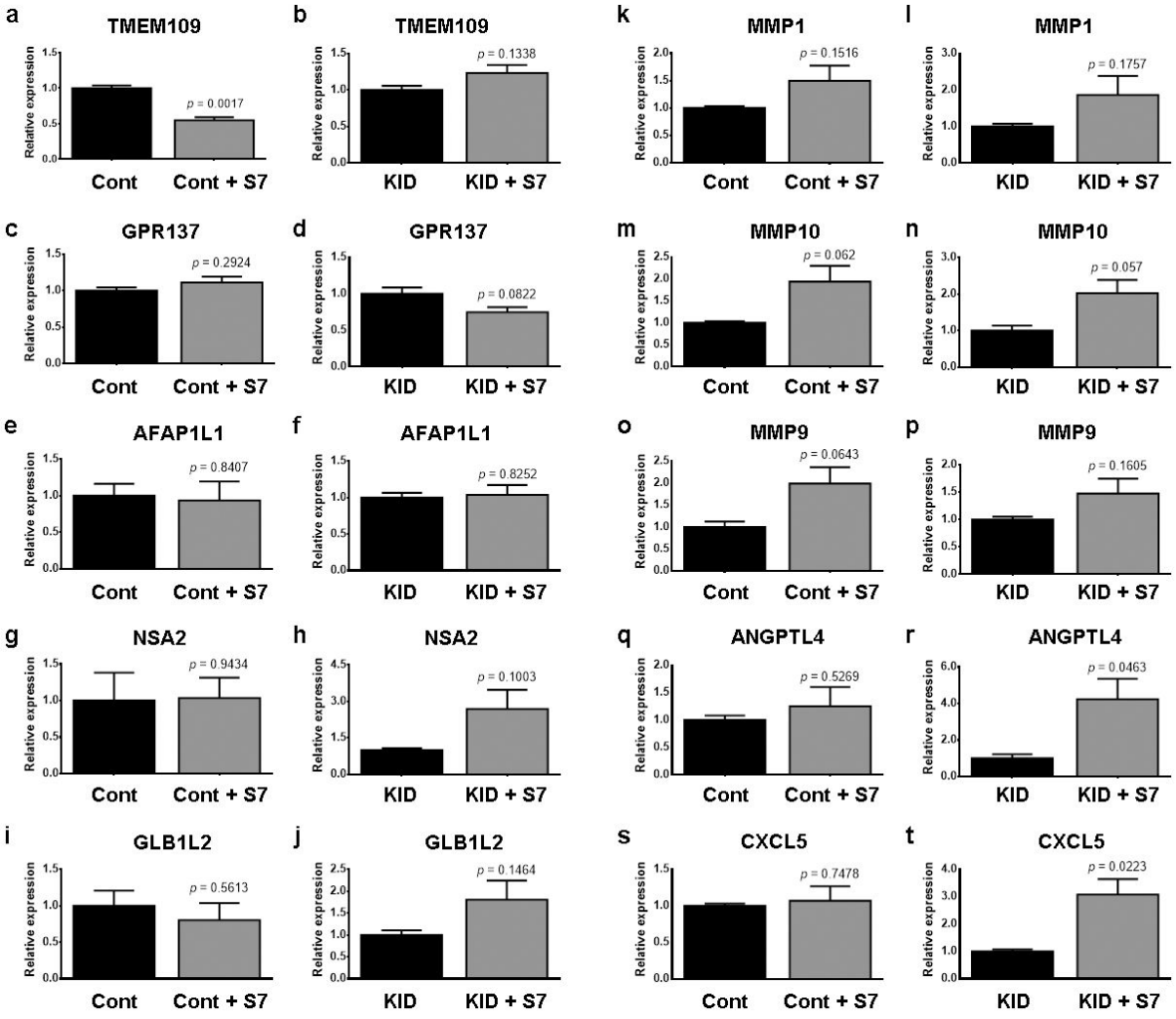

Supplementary Figure S4. Validation of the RNA-Seq data using qRT-PCR

RNA extracted from Control-KCs (Cont) and KID-KCs (KID) with or without treated S7 treatment were subjected to qRT-PCR using primers specific to the top 5 upregulated and 5 downregulated genes from the RNA-Seq analysis. The expression levels were calibrated by the internal control *GAPDH* gene. Data are represented as mean ± SEM and analyzed statistically using Student's *t*-test (n = 3).

ALLELE-SPECIFIC SIRNA CORRECTS ABERRANT CELLULAR PHENOTYPE IN KERATITIS-ICHTHYOSIS-DEAFNESS SYNDROME KERATINOCYTES

Ming Yang Lee[1], Hong-Zhan Wang[2], Thomas W. White[2], Tony Brooks[3], Alan Pittman[6,7], Heerni Halai[1], Anastasia Petrova[1], Diane Xu[1], Stephen L. Hart[4], Veronica A. Kinsler[4,5] and Wei-Li Di[1]

ORCiD:

Ming Yang Lee: 0000-0003-3135-3928

Hong-Zhan Wang: 0000-0002-3371-2309

Thomas W. White: 0000-0002-3285-7434

Tony Brooks: 0000-0002-3494-3045

Alan Pittman: 0000-0002-8112-2987

Heerni Halai: 0000-0003-1798-4600

Anastasia Petrova: 0000-0001-5294-399X

Diane Xu 0000-0002-1153-0352

Stephan L. Hart: 0000-0001-8254-376X

Veronica A. Kinsler: 0000-0001-6256-327X

Wei-Li Di: 0000-0002-4851-1649

1. Infection, Immunity and Inflammation Programme/Immunobiology Section, UCL Great Ormond Street Institute of Child Health, 30 Guilford St., London WC1N 1EH, United Kingdom
2. Department of Physiology and Biophysics, Basic Science Tower, T-5, Room 147, Stony Brook University, Stony Brook, NY, 11794-8661, USA

3. UCL Genomics, UCL Great Ormond Street Institute of Child Health, 30 Guilford St., London WC1N 1EH, United Kingdom
4. Department of Genetics and Genomic Medicine, UCL Great Ormond Street Institute of Child Health, 30 Guilford St., London WC1N 1EH, United Kingdom.
5. Paediatric Dermatology, Great Ormond Street Hospital for Children, London WC1N 3JH
6. Molecular Neuroscience, UCL Institute of Neurology, Queen Square, London WC1N 3BG, United Kingdom
7. Genetics Research Centre, St George's, University of London, Cranmer Terrace, London SW17 0RE, United Kingdom

Corresponding author:

Wei-Li Di

Infection, Immunity and Inflammation Programme/Immunobiology Section

UCL Great Ormond Street Institute of Child Health, 30 Guilford St., London WC1N 1EH, United Kingdom;

Tel: +44(0)2079052369;

email: w.di@ucl.ac.uk.

Short title:

Allele-specific siRNA for KID syndrome

Abbreviations:

KID: Keratitis-ichthyosis-deafness

KID-KC: KID syndrome patient-derived keratinocytes

control-KC: Healthy donor-derived keratinocytes

AS-siRNA: Allele-specific small interference RNA

SLDT: Scrape-loading dye transfer

RNA-Seq: RNA sequencing

GESS: Genome-wide enrichment of seed sequences

ABSTRACT

Keratitis-ichthyosis-deafness (KID) syndrome is a severe, untreatable condition characterized by ocular, auditory and cutaneous abnormalities, with major complications of infection and skin cancer. 86% of cases are caused by a heterozygous missense mutation (c.148G>A, p.D50N) in the *GJB2* gene, encoding gap junction protein connexin 26 (Cx26), which alters gating properties of Cx26 channels in a dominant manner. We hypothesized that a mutant-allele-specific siRNA (AS-siRNA) could rescue the cellular phenotype in patient keratinocytes. A KID syndrome cell line (KID-KC) was established from primary patient keratinocytes with a heterozygous p.D50N mutation. This displayed impaired gap junction communication and hyperactive hemichannels, confirmed by dye transfer, patch clamp and neurobiotin uptake assays. A human-murine chimeric skin graft model constructed with KID-KC mimicked patient skin *in vivo,* further confirming the validity of these cells as a model. *In vitro* treatment with AS-siRNA led to robust inhibition of the mutant *GJB2* allele without altering expression of the wildtype. This corrected both gap junction and hemichannel activity. Notably, AS-siRNA treatment caused only low-level off-target effects in KID-KC, as detected by genome-wide RNA sequencing. Our data provide an important proof-of-concept and model system for the potential use of AS-siRNA in treating KID syndrome, and other dominant genetic conditions.

INTRODUCTION

Keratitis-Ichthyosis-Deafness syndrome (KID syndrome, [MIM 148210]) is a rare, autosomal-dominant condition characterized by ocular and auditory impairment and hyperkeratotic skin lesions (Burns, 1915). Ocular involvement includes photophobia and neovascularization, progressively reducing visual acuity (Caceres-Rios et al., 1996), and auditory impairment features sensorineural hearing loss (Patel et al., 2015). Skin involvement consists of erythrokeratodermic or verrucous plaques, and palmoplantar keratoderma with alopecia and/or onychodystrophy (Caceres-Rios et al., 1996, Coggshall et al., 2013). Moreover, KID syndrome is frequently complicated with chronic, opportunistic cutaneous infection, resulting in failure to thrive and, in severe cases, septicemia (Coggshall et al., 2013). Patients are at increased risk of developing skin malignancies, particularly squamous cell carcinoma (Coggshall et al., 2013). These complications can have a significant impact on life expectancy. Current cutaneous treatment is limited to symptomatic management, including retinoids to attempt to improve the skin barrier, antifungal and antibacterial agents for infection control (Coggshall et al., 2013). There is an unmet need for targeted treatment of this condition.

The cause of KID syndrome was identified as heterozygous missense mutations in the *GJB2* gene (van Steensel et al., 2002, Richard et al., 2002), which encodes a transmembrane, gap junction (GJ) channel-forming protein, connexin 26 (Cx26). GJs are clustered intercellular structures found in virtually all contacting cell types, enabling direct cell-cell communication via the exchange of ions, nutrients and signaling molecules with a molecular weight < 1 kDa (Levit et al., 2015, Elfgang et al., 1995). Connexin proteins, the constituents of GJs, can oligomerize to form hexameric structure known as connexons. On the plasma membrane, connexons can either function alone as hemichannels, or ‘dock’ with a compatible connexon from the adjacent cell membrane to form a

GJ (Laird, 2006). Undocked hemichannels serve as a conduit between the cytoplasm and the extracellular space of the cell, while GJs couple the cytoplasm of adjacent cells electrically and biochemically (Garcia et al., 2016).

To date, twelve missense *GJB2* mutations have been reported in KID syndrome, among which the mutation c.148G>A, resulting in the substitution of aspartic acid for asparagine at codon 50 (p.D50N), is by far the most common mutation, accounting for 86% of cases in the largest European cohort (Mazereeuw-Hautier et al., 2007). At least 10 out of the 12 identified mutations, including p.D50N, have been associated with aberrant hemichannel behavior (Lee et al., 2009, Garcia et al., 2016, Donnelly et al., 2012, Mese et al., 2011), presented as elevated membrane currents (Lee et al., 2009), enhanced permeability to small-molecule tracers (Mese et al., 2011), and/or enhanced ATP release in response to a specific stimuli (Garcia et al., 2016, Donnelly et al., 2012). Therefore, hemichannels have been considered a potential therapeutic target when developing new KID syndrome treatment (Levit et al., 2015, Xu et al., 2017). Recent work has shown that mefloquine, an FDA-approved anti-malarial drug, potently suppresses aberrant hemichannels in primary keratinocytes from a transgenic mouse model with heterozygous p.G45E mutation in *GJB2* (Levit et al., 2015). Very recently, the monoclonal antibody abEC1.1 was developed, which specifically suppressed hemichannels formed by Cx26-wildtype (WT), p.G45E or p.D50N mutants (Xu et al., 2017). However, it is unclear whether those strategies can discriminate mutant *GJB2* allele from the WT. This concern is particularly important given the context that most KID syndrome mutants exert dominant effects on co-expressed WT connexins (Di et al., 2005, Garcia et al., 2015). In the last decade, allele-specific small interference RNA (AS-siRNA) technology has shown strong therapeutic potential in treatment of dominant genetic

disorders and brought clinical benefits to a patient with pachyonychia congenita (Trochet et al., 2015).

We present a specific and effective AS-siRNA against the *GJB2* c.148G>A (p.D50N) mutation, which successfully rescues the abnormal cellular phenotype in patient-derived keratinocytes. Our approach could potentially be a novel future therapy for this debilitating and life-limiting condition.

RESULTS

Patient-derived keratinocytes with heterozygous c.148G>A (p.D50N) mutation had aberrant gap junction and hemichannel behavior and caused hyperkeratotic skin morphology

Previous studies on mutant *GJB2* expression, distribution and function have largely relied on ectopic expression of homozygous *GJB2* mutations in *Xenopus* oocytes (Lopez et al., 2013) and HeLa cells (Press et al., 2017b). These models, however, do not accurately represent the genetic state in KID syndrome patients who are heterozygotes for *GJB2* mutations, and therefore have limitations when used in preclinical evaluation for new therapeutic strategies. To overcome this, primary keratinocytes isolated from a fresh skin biopsy of the KID syndrome patient heterozygous for c.148G>A (p.D50N) mutation in *GJB2* were immortalized using the lentiviral vector encoding HPV type 16 E6/E7 cDNA.

The mutation *GJB2* c.148G>A was confirmed in the immortalized cells (KID-KCs) **(Figure 1a)**. Keratinocytes obtained from a healthy donor and immortalized with the same protocol were used as a control (control-KCs). Both immortalized cell lines showed polygonal morphology with various sizes in early passages but were more uniformly shaped in later passages **(Figure 1b)**. The cell morphology and genotype were monitored over a propagation period up to 45 passages. There was no apparent change in morphology and the mutation in KID-KCs was expressed stably. The

expression of endogenous *GJB2* mRNA in KID-KCs and control-KCs was examined by quantitative reverse transcriptase-PCR (qRT-PCR) using specific primers for total *GJB2*. A reduction of 44% in total *GJB2* mRNA in KID-KCs was seen compared to that in control-KCs (n = 4, $p = 0.24$) **(Figure 1c)**. The PCR amplicon of KID-KCs was sequenced, and the chromatogram exhibited a 1:1 ratio for WT : mutant allele peaks at c.148 locus **(Figure 1a)**, suggesting similar mRNA expression levels for both WT and mutant alleles in KID-KCs.

The expression of the Cx26 protein was also examined by immunoblotting. Several anti-Cx26 antibodies have been used in immunoblotting previously (Yum et al., 2007, Press et al., 2017a), but the majority was used to detect Cx26 in rodent cells or tissues or in HeLa cells ectopically expressing Cx26, and only few were able to detect endogenous Cx26 in cultured human keratinocytes. This is possibly due to low endogenous Cx26 level or a lack of anti-Cx26 antibodies with sufficient affinity/specificity. We tested six antibodies and found that the pair of a rabbit polyclonal antibody (Thermo Fisher Scientific, 13-8100) and a mouse monoclonal antibody (Merck Millipore, MABT198) gave a clear band at 26 kDa when used for immunoprecipitation experiments **(Figure 1d)**. Immunoprecipitation using these pair of antibodies showed a reduction in Cx26 protein expression in KID-KCs compared to control-KCs, which was consistent with the qRT-PCR results.

The distribution of Cx26 in the cells was determined using immunostaining. In control-KCs, punctate or plaque-like Cx26 staining was observed at cell-cell contact sites **(Figure 1e)**, which were indicated by membranous staining of E-cadherin, suggesting that WT Cx26 was able to traffic to the plasma membrane and formed GJ plaques. By contrast, Cx26 in KID-KCs failed to accumulate at membrane regions but showed a primarily discrete punctate staining pattern in the cytoplasm **(Figure 1e)**. Although a small portion of GJ plaques overlaid with E-cadherin at the

plasma membrane, they were smaller in size compared to those observed in control-KCs. Interestingly, the immunostaining pattern of the patient skin did not show striking reduction or mis-localization of Cx26 expression **(Figure 1f)**. This could be, in part, explained by the *in vitro* culture condition which rendered keratinocytes more proliferative and less differentiative, given that Cx26 is predominantly expressed in differentiated keratinocytes (Churko and Laird, 2013, Martin et al., 2014).

The function of GJ intercellular communication in KID-KCs was assessed by scrape-loading dye transfer (SLDT) using the neurobiotin tracer and compared to control-KCs. Neurobiotin diffused extensively from initially scrape-loaded cells to neighboring cells in control-KCs **(Figure 2a)**. In contrast, the diffusion of neurobiotin in KID-KCs reduced markedly and was almost confined to the first line of the scrape-wounded cells. Quantification of the images revealed a reduction of 58% in diffusion area in KID-KCs, compared to that in control-KCs (n = 3 each, $p < 0.01$), suggesting that the GJ channels formed in KID-KCs were defective **(Figure 2b)**.

Next, the activity of hemichannels in KID-KCs was measured using whole-cell patch clamp and neurobiotin uptake assay. Moderate membrane currents were recorded from control-KCs at both depolarizing and hyperpolarizing membrane voltages, whereas large currents were elicited from KID-KCs at all tested membrane voltages, more prominently at depolarizing voltages between +30 mV and +110 mV **(Figure 2c)**. The maximum current density recorded from KID-KCs was 80% greater than that in control-KCs (9.0 ± 1.3 pA/pF, n = 21 cells vs. 5.0 ± 0.6 pA/pF, n = 14 cells, measured at +110 mV, $p < 0.05$) **(Figure 2d)**. Consistent with the patch clamp results, KID-KCs showed a marked increase in uptake of neurobiotin tracer compared to control-KCs (n = 29 and 34 cells, respectively, $p < 0.001$) **(Figure 2e)**. These results suggested enhanced membrane conductivity and neurobiotin permeability in KID-KCs, indicating hyperactive hemichannel

behavior conferred by the mutation. Our *in vitro* findings indicated that, despite expressing Cx26 at a relatively low level in culture, the KID-KCs displayed an aberrant cellular phenotype that has been reported previously in other KID syndrome disease models (Arita et al., 2006, Lee et al., 2009, Garcia et al., 2016).

To confirm that the immortalized KID-KCs remained capable of proliferation and differentiation, i.e. characteristics of primary keratinocytes *in vivo*, these cells were tested in a human-murine chimeric skin graft model (Di et al., 2011). Histological examination of the skin graft regenerated from immortalized KID-KCs showed similar features seen in the KID syndrome patient skin, including hyperkeratosis and spongiosis **(Figure 3)**. Collectively, the immortalized KID-KCs are a suitable model for evaluating therapeutic efficacy of AS-siRNA for KID syndrome.

AS-siRNA selectively inhibited the c.148G>A mutation in KID-KCs

Nineteen candidate AS-siRNAs with a targeting sequence complementary to the c.148G>A mutation (S1−S19) were screened at a concentration of 50 nM in Hela cell lines stably expressing WT or mutant *GJB2* fused with the *GFP* reporter gene. Both cell lines were transfected with each of 19 AS-siRNAs, followed by flow cytometry analysis for reduction of GFP intensity **(Supplementary Figure S1b)**. The knockdown efficiency of S7 and S10 in cells expressing the mutant *GJB2-GFP* was approximately 50%. Since S7 inhibited mutant *GJB2* specifically and reproducibly from three independent screening experiments **(Supplementary Figure S2)**, this siRNA was selected for further study.

The allele-specific action of S7 at 50 nM was tested in the KID-KCs harboring the heterozygous mutation. KID-KCs and control-KCs were treated with S7 and the mRNA expression of *GJB2* in treated cells was examined 24 hrs post-treatment by qRT-PCR. The treatment resulted in a

significant decrease of 63% in total *GJB2* mRNA in KID-KCs compared to untreated cells (n = 3, $p = 0.0065$), but the decrease was not detected in control-KCs with the same treatment (n = 3, $p = 0.84$) **(Figure 4a)**. Further investigation using allele-specific primers showed no difference in mRNA expression of the WT allele between untreated and S7-treated cells (n = 3, $p = 0.51$ for KID-KCs and $p = 0.60$ for control-KCs), whereas mRNA expression of the mutant allele in KID-KCs was significantly inhibited by 43% following S7 treatment (n = 3, $p = 0.0065$). At protein level, Cx26 expression showed an average decrease of 56% (range 52−64%, n = 3) in total endogenous Cx26 expression in KID-KCs following S7 treatment, compared to those treated with an irrelevant siRNA, si-cont **(Figure 4b-c)**. This change was not detected in S7-treated control-KCs, which showed a slight increase in Cx26 expression (range 5−16%, n = 3). All these results indicated that S7 had strong selectivity for the mutant *GJB2* c.148G>A allele over the WT allele in the patient keratinocytes, and it had little effect on the normal keratinocytes where only the WT allele was present.

AS-siRNA treatment reversed aberrant gap junction and hemichannel functions in KID-KCs

KID-KCs treated with S7 or si-cont at 50 nM were further analyzed for GJ intercellular communication and hemichannel activity. GJ-mediated intercellular diffusion of neurobiotin tracer was analyzed 24 hrs post-treatment using the SLDT assay. The results showed a 24% increase in neurobiotin diffusion in KID-KCs treated with S7 compared to those treated with si-cont (n = 34 and 37 images, respectively, $p < 0.01$) **(Figure 5b, d)**, whereas no significant difference in neurobiotin transfer was observed in control-KCs treated with either S7 or si-cont (n = 30 and 35 images, respectively, $p > 0.05$) **(Figure 5a, c)**. The hemichannel activity in the treated cells was assessed by whole-cell patch clamp. The results showed a decrease of 35% in membrane current

density in KID-KCs treated with S7, compared to those treated with si-cont (9.02 ± 1.16 pA/pF, n = 20 cells vs. 5.86 ± 0.43 pA/pF, n = 22 cells, measured at +110 mV, $p < 0.05$), while no statistical differences were found in control-KCs following S7 or si-cont treatment (n =10 cells each group, $p > 0.05$) **(Figure 5f-h)**. Notably, the current density level in S7-treated KID-KCs was comparable to that in control-KCs**.** The activity of hemichannels was further examined by neurobiotin uptake assay, which showed a significant decrease in neurobiotin uptake in KID-KCs after S7 treatment (n = 21 and 27 images, $p < 0.001$), in line with the patch clamp results **(Figure 5i-j)**.

These findings suggested functional recovery following the inhibition of mutant *GJB2* allele by S7, namely improvement of the defective GJ-mediated cell coupling and reversal of the aberrant non-junctional hemichannel behavior, including electrical conduction and permeability.

Low-level off-target effects of AS-siRNA, S7

Despite promising efficacy data obtained from S7, a general concern in preclinical AS-siRNA studies is off-target effects that may cause unintended alteration in unrelated gene expression (Trochet et al., 2018). To explore comprehensively the specificity of S7, RNA-Seq was carried out S7-treated or non-treated KID-KCs. 26485 genes from the libraries were mapped to the reference human genome (with 15,802 null- or low-expressed genes), among which only 6 genes were found to be differentially expressed in S7-treated KID-KCs compared to the non-treated cells (range of fold change: 2.01−2.32), indicating that S7 resulted in mild global effects on the KID-KC transcriptome. To validate the results, the top 5 upregulated (*MMP1*, *MMP10*, *MMP9*, *ANGPTL4*, *CXCL5*) and downregulated genes (*GLB1L2*, *NSA2*, *AFAP1L1*, *GPR137*, *TMEM109*) were further analyzed by qRT-PCR **(Table 1)**. Control-KCs with or without S7 treatment were run in parallel as additional controls. The results confirmed the upregulation of the *MMPs* and the downregulation

of *GPR137* in KID-KCs with comparable levels of fold change **(Supplementary Figure S4)**; however, the *MMPs* were also found upregulated in S7-treated control-KCs.

A common cause of siRNA-mediated gene alteration is sequence matching between the seed region of siRNA and the target mRNA (Yilmazel et al., 2014, Jackson and Linsley, 2010). To investigate whether this was an underlying mechanism for the differential expression of the above genes, we employed the online tool, genome-wide enrichment of seed sequences (GESS), to analyze the sequence of S7. A total of 180 genes were found to have sequence match(es) with S7 **(Supplementary Table S2)**, among which only *GPR137* was found, with its 3'-untranslated region and coding sequence complementary to the seed region of either of the S7 strands. This implied that downregulation of *GPR137* may have resulted from seed region-dependent off-target effects. The mechanism of alteration of the other genes remains to be clarified.

DISCUSSION

We study AS-siRNA using KID-KC, an immortalized, patient-derived keratinocyte cell line which harbors a heterozygous c.148G>A mutation, representing the genetic state in KID syndrome patients. Although use of primary keratinocytes from patient skin biopsy would have been ideal for this study, these cells have a limited lifespan which restricts us from performing multiple experiments. To bypass the restrictions, we used immortalized patient keratinocytes due to their indefinite lifespan and capability of proliferation and differentiation, i.e. features of primary keratinocytes (Choi et al., 2017). This was further confirmed in our *in vivo* skin graft experiments, where regenerated skin grafts from immortalized KID-KCs recapitulated the epidermal architecture of the KID syndrome patient skin.

Our immunostaining found lower Cx26 expression level in cultured immortalized cells compared to that in skin tissues. This is not surprising, as monolayer culture contains a dominating proportion of proliferating keratinocytes with low-level Cx26 expression (Martin et al., 2014). Despite the lower expression, we were able to show aberrant hemichannel and GJ behavior in KID-KCs, which is in line with data generated from previous *in vitro* models such as *Xenopus* oocytes (Lee et al., 2009, Sanchez et al., 2013), HeLa cells (Di et al., 2005) and corneal epithelial cells (Shurman et al., 2005) ectopically expressing the c.148G>A mutant. This suggested that the reduced Cx26 expression *in vitro* is unlikely to influence the interpretation of our results. Collectively, the immortalized, patient-derived model, which recapitulates the genetics, cellular and histological phenotypes of the condition, has significant advantages over the previous models and hence can serve as a good preclinical model for translational development of new therapeutic approaches.

The action of previously reported approaches to inhibit connexins, including monoclonal antibodies (Xu et al., 2017) and synthetic peptide mimetics (Becker et al., 2012), is mediated by either altering the biophysical property of target connexin channels or modulating interaction between target connexins and their binding partners. In contrast to those approaches, AS-siRNA silences target gene expression by degrading mRNA based on perfect sequence matching, thereby blocking the translation of target protein (Jackson and Linsley, 2010). As AS-siRNA is able to discriminate mutant and WT mRNA sequences differing by even a single base, we harness this technology to develop a targeted therapy for KID syndrome. Our results have confirmed that the lead AS-siRNA, S7, targeted to the mutant *GJB2* allele in a potent and specific manner while maintaining expression of the WT allele and its protein function, providing strong basis for future translation of the AS-siRNA.

In human keratinocytes, Cx26 forms heteromeric and heterotypic channels with other compatible types of connexins (Di et al., 2001). These heterogenous channels have biophysical properties differing from their homogenous counterparts, providing dynamic regulation in response to different stimuli. Recent studies proposed that aberrant interaction with Cx43 is an emerging mechanism by which certain Cx26 mutants can cause diseases through heteromeric channels (Garcia et al., 2015, Shuja et al., 2016). We performed double immunofluorescence staining in our patient skin tissues and cultured KID-KCs, and the results did not show clear colocalization between Cx26 and Cx43 (data not shown). As this is our preliminary data, further investigation is required in the future.

The low endogenous expression of Cx26 in human keratinocytes (Richard et al., 2002, Di et al., 2001) posted a challenge in our initial attempts of immunoblotting to detect Cx26, which showed multiple bands. Issues regarding the presence of multiple bands were also reported by others (Gassmann et al., 2009), and were considered to result from oligomers and protein aggregates of Cx26. Our optimized immunoprecipitation/immunoblotting approach allowed enrichment of low-abundant Cx26 in cultured patient keratinocytes, leading to successful quantification of siRNA-medicated Cx26 knockdown.

Our work provides proof-of-concept for the use of AS-siRNA in targeted therapy for KID syndrome. In the context of patient skin, the AS-siRNA-mediated reversal of connexin channel function may possibly improve the disturbed epidermal Ca^{2+} gradient that is contributed by homomeric or heteromeric channels formed by mutant Cx26 (Bosen et al., 2015), thereby leading to improved hyperkeratotic phenotype. Also, since enhanced hemichannel activity has been linked to release of inflammatory cytokines when exposing c.148G>A-expressing keratinocytes to peptidoglycans from an opportunistic pathogen, *Staphylococcus aureus* (Donnelly et al., 2012),

AS-siRNA is also likely to contribute towards control of skin infection and inflammation. Furthermore, the c.148G>A mutation has been found in the majority of KID syndrome patients. Thus, the mutation-targeted AS-siRNA would serve as potentially effective and safe therapeutic intervention for KID syndrome, the debilitating condition that has no effective specific treatment options at present. Although *in vivo* delivery of siRNA remains challenging, strategies including nanoparticles (Zheng et al., 2012), penetration enhancers (Hegde et al., 2014), microneedles (Chong et al., 2013) and electroporation (Broderick et al., 2012) have shown promise in topical siRNA delivery into the skin in a non- or minimally-invasive manner, causing silencing of target genes. We are currently optimizing a topical delivery platform and the therapeutic efficacy of the AS-siRNA will be tested in our *in vivo* human-murine chimeric skin graft model generated using immortalized KID-KCs. If successful, our strategy could potentially be adapted to other skin conditions with dominant mutations.

MATERIALS AND METHODS

KID syndrome patient-derived keratinocytes

3-mm punch biopsies from a KID syndrome patient with the heterozygous c.148G>A mutation, and a healthy volunteer donor, were obtained under a protocol approved by the local ethics committee (12/LO/1522) with informed written consent. The epidermis was isolated freshly from the biopsies as described previously (Di et al., 2011). The primary keratinocytes were immortalized by transduction with a second-generation, replication-deficient, self-inactivating HIV-1 lentiviral vector (Yanez-Munoz et al., 2006) constructed with human papilloma virus type 16 E6/E7 cDNA (**Supplementary Figure S3**). Immortalized cells were established following serial propagation and thereafter were cultured in the keratinocyte culture medium without feeder cells.

Statistical analysis

All data were expressed as the mean ± standard error of the mean (SEM). Comparisons of data from qRT-PCR, patch clamp, neurobiotin uptake and SLDT experiments were made by Student's t-test using GraphPad Prism v6.01 (GraphPad Software, San Diego, CA, USA). Differences with a p-value less than 0.05 were considered statistically significant. *$p < 0.05$; **$p < 0.01$; and ***$p < 0.001$.

Detailed methods for immunostaining, siRNA design, qRT-PCR, immunoprecipitation and immunoblotting, patch clamp, neurobiotin uptake, SLDT, RNA-Seq and *in vivo* skin graft experiments are described in **Supplementary Materials**.

DATA AVAILABILITY STATEMENT

Datasets related to this article can be found at https://www.ncbi.nlm.nih.gov/geo/query/acc.cgi?acc=GSE131709, an open-source online data repository hosted at Gene Expression Omnibus (GEO).

CONFLICT OF INTEREST

The authors declared no conflict of interest.

ACKNOWLEDGMENTS

We gratefully acknowledge the participation of all patients and families in this study, as well as the National Institute for Health Research (NIHR) Biomedical Research Centre based at Great Ormond Street Hospital for Children NHS Foundation Trust and UCL Institute of Child Health. The views expressed are those of the author(s) and not necessarily those of the NHS, the NIHR or the Department of Health. This work was also supported by Newlife Foundation for Disabled Children and the UCL Bogue Fellowship. We are indebted to Dr. Ayad Eddaoudi and Dr. Dale Moulding (ICH Core Facility) for their expertise in flow cytometry and image analysis. WLD is a Great Ormond Street Hospital Children's Charity Senior Lecturer. TWW is funded by the National Institutes of Health (grant numbers EY013163 and EY026911). VAK is funded by the Wellcome Trust (grant number WT104076MA).

AUTHOR CONTRIBUTIONS

Conceptualization: SLH, VAK, WLD; Formal Analysis: MYL, HZW, TWW, TB, AP[6,7], HH, DX, WLD; Funding Acquisition: MYL, SLH, VAK, WLD; Investigation: MYL, HZW, TWW, HH,

AP[1], WLD; Methodology: MYL, HZW, TWW, SLH, VAK, WLD; Resources: TWW, VAK, WLD; Supervision: TWW, SLH, VAK, WLD; Writing− Original Draft: MYL, VAK, WLD; Writing− Review and Editing: MYL, TWW, TB, AP[1], SLH, VAK, WLD.

REFERENCES

Arita K, Akiyama M, Aizawa T, Umetsu Y, Segawa I, Goto M, et al. A novel N14Y mutation in Connexin26 in keratitis-ichthyosis-deafness syndrome: analyses of altered gap junctional communication and molecular structure of N terminus of mutated Connexin26. Am J Pathol 2006; 169, 416-23.

Becker DL, Thrasivoulou C, Phillips AR. Connexins in wound healing; perspectives in diabetic patients. Biochim Biophys Acta 2012; 1818: 2068-75.

Bosen F, Celli A, Crumrine D, Vom Dorp K, Ebel P, Jastrow H, et al. Altered epidermal lipid processing and calcium distribution in the KID syndrome mouse model Cx26S17F. FEBS Lett 2015; 589: 1904-10.

Broderick KE, Chan A, Lin F, Shen X, Kichaev G, Khan AS, et al. Optimized in vivo transfer of small interfering RNA targeting dermal tissue using in vivo surface electroporation. Mol Ther Nucleic Acids 2012; 1, e11.

Burns FS. A case of generalized congenital keratoderma with unusual involvement of eyes, ears and nasal and buccal mucous membranes. J Cutan Dis 1915; 33: 255-60.

Caceres-Rios H, Tamayo-Sanchez L, Duran-Mckinster C, De La Luz Orozco M, Ruiz-Maldonado R. Keratitis, ichthyosis, and deafness (KID syndrome): review of the literature and proposal of a new terminology. Pediatr Dermatol 1996; 13: 105-13.

Choi M, Park M, Lee S, Lee JW, Cho MC, Noh M, et al. Establishment of Immortalized Primary Human Foreskin Keratinocytes and Their Application to Toxicity Assessment and Three Dimensional Skin Culture Construction. Biomol Ther (Seoul) 2017; 25, 296-307.

Chong RH, Gonzalez-Gonzalez E, Lara MF, Speaker TJ, Contag CH, Kaspar RL, et al. Gene silencing following siRNA delivery to skin via coated steel microneedles: In vitro and in vivo proof-of-concept. J Control Release 2013; 166, 211-9.

Churko JM. and Laird DW. Gap Junction Remodeling in Skin Repair Following Wounding and

Disease. Physiology 2013; 28, 190-198.

Coggshall K, Farsani T, Ruben B, Mccalmont TH, Berger TG, Fox LP, et al. Keratitis, ichthyosis, and deafness syndrome: a review of infectious and neoplastic complications. J Am Acad Dermatol 2013; 69: 127-34.

Di WL, Gu Y, Common JE, Aasen T, O'toole EA, Kelsell DP, et al. Connexin interaction patterns in keratinocytes revealed morphologically and by FRET analysis. J Cell Sci 2005; 118: 1505-14.

Di WL, Larcher F, Semenova E, Talbot GE, Harper JI, Del Rio M, et al. Ex-vivo gene therapy restores LEKTI activity and corrects the architecture of Netherton syndrome-derived skin grafts. Mol Ther 2011; 19: 408-16.

Di WL, Rugg EL, Leigh IM, Kelsell DP. Multiple epidermal connexins are expressed in different keratinocyte subpopulations including connexin 31. J Invest Dermatol 2001; 117: 958-64.

Donnelly S, English G, de Zwart-Storm EA, Lang S, van Steensel MA, Martin PE. Differential susceptibility of Cx26 mutations associated with epidermal dysplasias to peptidoglycan derived from Staphylococcus aureus and Staphylococcus epidermidis. Exp Dermatol 2012; 21: 592-8.

Elfgang C, Eckert R, Lichtenberg-Frate H, Butterweck A, Traub O, Klein RA, et al. Specific permeability and selective formation of gap junction channels in connexin-transfected HeLa cells. J Cell Biol 1995; 129: 805-17.

Garcia IE, Bosen F, Mujica P, Pupo A, Flores-Munoz C, Jara O, et al. From hyperactive connexin26 hemichannels to impairments in epidermal calcium gradient and permeability barrier in the keratitis-ichthyosis-deafness syndrome. J Invest Dermatol 2016; 136: 574-83.

Garcia IE, Maripillan J, Jara O, Ceriani R, Palacios-Munoz A, Ramachandran J, et al. Keratitis-ichthyosis-deafness syndrome-associated Cx26 mutants produce nonfunctional gap junctions but hyperactive hemichannels when co-expressed with wild type Cx43. J Invest Dermatol 2015; 135: 1338-47.

Gassmann O, Kreir M, Ambrosi C, Pranskevich J, Oshima A, Roling C, et al. The M34A mutant of connexin26 reveals active conductance states in pore-suspending membranes. J Struct Biol 2009; 168: 168-76.

Hegde V, Hickerson RP, Nainamalai S, Campbell PA, Smith FJ, Mclean WH, et al. In vivo gene silencing following non-invasive siRNA delivery into the skin using a novel topical formulation. J Control Release 2014; 196, 355-62.

Jackson AL, Linsley PS. Recognizing and avoiding sirna off-target effects for target identification and therapeutic application. Nat Rev Drug Discov 2010; 9: 57-67.

Laird DW. Life cycle of connexins in health and disease. Biochem J 2006; 394: 527-43.

Lee JR, Derosa AM, White TW. Connexin mutations causing skin disease and deafness increase hemichannel activity and cell death when expressed in xenopus oocytes. J Invest Dermatol 2009; 129: 870-8.

Levit NA, Sellitto C, Wang HZ, Li L, Srinivas M, Brink PR, et al. Aberrant connexin26 hemichannels underlying keratitis-ichthyosis-deafness syndrome are potently inhibited by mefloquine. eInsights on the mechanisms of Ca2+ regulation of connexin26 hemichannels revealed by human pathogenic mutations (D50N/Y). J Gen Physiol 2013; 142: 23-35.

Martin PE, Easton JA, Hodgins MB, Wright CS. Connexins: sensors of epidermal integrity that are therapeutic targets. FEBS Lett 2014; 588, 1304-14.

Mazereeuw-Hautier J, Bitoun E, Chevrant-Breton J, Man SY, Bodemer C, Prins C, et al. Keratitis-ichthyosis-deafness syndrome: disease expression and spectrum of connexin 26 (GJB2) mutations in 14 patients. Br J Dermatol 2007; 156: 1015-9.

Mese G, Sellitto C, Li L, Wang HZ, Valiunas V, Richard G, et al. The Cx26-G45E mutation displays increased hemichannel activity in a mouse model of the lethal form of keratitis-ichthyosis-deafness syndrome. Mol Biol Cell 2011; 22: 4776-86.

Patel V, Sun G, Dickman M, Khuu P, Teng JM. Treatment of keratitis-ichthyosis- deafness (KID) syndrome in children: a case report and review of the literature. Dermatol Ther 2015; 28:

89-93.

Press ER, Shao Q, Kelly JJ, Chin K, Alaga A, Laird DW. Induction of cell death and gain-of-function properties of connexin26 mutants predict severity of skin disorders and hearing loss. J Biol Chem 2017; 292: 9721-32.

Richard G, Rouan F, Willoughby CE, Brown N, Chung P, Ryynanen M, et al. Missense mutations in GJB2 encoding connexin-26 cause the ectodermal dysplasia keratitis-ichthyosis-deafness syndrome. Am J Hum Genet 2002; 70: 1341-8.

Sanchez HA, Villone K, Srinivas M, Verselis VK. The D50N mutation and syndromic deafness: altered Cx26 hemichannel properties caused by effects on the pore and intersubunit interactions. J Gen Physiol 2013; 142: 3-22.

Shuja Z, Li L, Gupta S, Mese G, White TW. Connexin26 Mutations Causing Palmoplantar Keratoderma and Deafness Interact with Connexin43, Modifying Gap Junction and Hemichannel Properties. J Invest Dermatol 2016; 136, 225-35.

Shurman DL, Glazewski L, Gumpert A, Zieske JD, Richard G. In vivo and in vitro expression of connexins in the human corneal epithelium. Invest Ophthalmol Vis Sci 2005; 46: 1957-65.

Trochet D, Prudhon B, Beuvin M, Peccate C, Lorain S, Julien L, et al. Allele-specific silencing therapy for dynamin 2-related dominant centronuclear myopathy. EMBO Mol Med 2018; 10: 239-253.

Trochet D, Prudhon B, Vassilopoulos S, Bitoun M. Therapy for dominant inherited diseases by allele-specific RNA interference: successes and pitfalls. Curr Gene Ther 2015; 15: 503-10.

van Steensel MA, van Geel M, Nahuys M, Smitt JH, Steijlen PM. A novel connexin 26 mutation in a patient diagnosed with keratitis-ichthyosis-deafness syndrome. J Invest Dermatol 2002; 118, 724-7.

Wang HJ, Chen TM, Cheng LF, Cheng TY, Tung YM. Human keratinocyte culture using porcine pituitary extract in serum-free medium. Burns 1995; 21, 503-6.

Xu L, Carrer A, Zonta F, Qu Z, Ma P, Li S, et al. Design and characterization of a human monoclonal antibody that modulates mutant connexin 26 hemichannels implicated in deafness and skin disorders. Front Mol Neurosci 2017; 10: 298.

Yanez-Munoz RJ, Balaggan KS, Macneil A, Howe SJ, Schmidt M, Smith AJ, et al. Effective gene therapy with nonintegrating lentiviral vectors. Nat Med 2006; 12, 348-53.

Yilmazel B, Hu Y, Sigoillot F, Smith JA, Shamu CE, Perrimon N, et al. Online GESS: prediction of miRNA-like off-target effects in large-scale rnai screen data by seed region analysis. BMC Bioinformatics 2014; 15: 192.

Yum SW, Zhang J, Valiunas V, Kanaporis G, Brink PR, White TW, et al. Human connexin26 and connexin30 form functional heteromeric and heterotypic channels. Am J Physiol Cell Physiol 2007; 293, C1032-48.

Zheng D, Giljohann DA, Chen DL, Massich MD, Wang XQ, Iordanov H, et al. Topical delivery of siRNA-based spherical nucleic acid nanoparticle conjugates for gene regulation. Proc Natl Acad Sci U S A 2012 109, 11975-80.

TABLES

Table 1. Top five up- and downregulated genes from the RNA-Seq experiments

Top five upregulated genes (KID-KCs, S7 vs. untreated)			
Gene	Protein	Fold Change	*p-adj
MMP1	Matrix metalloproteinase-1	2.24, up	9.50E-22
MMP10	Matrix metalloproteinase-10	2.06, up	4.19E-30
MMP9	Matrix metalloproteinase-9	1.95, up	4.90E-65
ANGPTL4	Angiopoietin-like 4	1.93, up	3.57E-28
CXCL5	C-X-C motif chemokine 5	1.74, up	6.26E-45
Top five downregulated genes (KID-KCs, S7 vs. untreated)			
Gene	Protein	Fold Change	*p-adj
GLB1L2	Galactosidase Beta 1 Like 2	2.31, down	2.17E-14
NSA2	Ribosome biogenesis homolog	2.16, down	1.99E-68
AFAP1L1	Actin filament-associated protein 1-like 1	2.01, down	1.99E-27
GPR137	G protein-coupled receptor 137	2.00, down	3.96E-09
TMEM109	Transmembrane Protein 109	1.94, down	3.92E-47

*p-adj, adjusted p-value for multiple statistical testing (Benjamini-Hochberg method)

FIGURE LEGENDS

Figure 1. Genotype, morphology, *GJB2* expression and subcellular localization in keratinocytes

cDNA sequences of *GJB2* from the KID syndrome patient and healthy donor are shown in (a). The morphology of keratinocytes from healthy donor and KID patient at early passages (P1 or P5) and late passages (P35 or P45) is shown in (b). The mRNA expression of total *GJB2*, the wildtype (WT) allele and the mutant allele in healthy donor and KID patient keratinocytes determined by qRT-PCR are shown in (c). The total Cx26 protein (asterisk, at 26 kDa) expression was examined by immunoprecipitation and immunoblotting (d), which shows decreased Cx26 expression in patient cells. The expression of Cx26 detected by immunofluorescence staining is shown in (e), where gap junction plaques can be found at cell-cell junctions in normal keratinocyte (arrows), whereas Cx26 in KID patient keratinocytes was localized discretely in the cytoplasm (arrowheads). E-cadherin (E-Cad) was stained in green color. Cx26 expression in the skin is shown in (f), where punctate staining of Cx26 was observed (arrows). The dotted lines show dermal-epidermal junction. Bar = 100 μm (b) and 40 μm (e, f). KID: KID patient-derived keratinocytes; Cont: keratinocytes derived from the healthy donor; N.S: not significant; ***$p < 0.001$.

Figure 2. Abnormal gap junction and hemichannel behavior in KID-KCs

The gap junction intercellular communication in KID-KCs (KID) or control-KCs (Cont) was examined by the SLDT assay, and the hemichannel activity was examined by whole-cell patch clamp and neurobiotin uptake. Representative images of SLDT in the keratinocytes using neurobiotin tracer (red) is shown in (a). Data analysis (b) shows that KID-KCs had impaired ability to transfer neurobiotin to adjacent cells. Representative patch clamp records from single

keratinocytes in response to the voltage step protocol from -110 mV to +110 mV in 20 mV increments are shown in (c). The plot of current density against membrane voltage reveals aberrantly enhanced hemichannel activity in KID-KCs (d). Representative images of neurobiotin uptake (NB, red) are shown (e), with the nuclei stained with DAPI (blue). Data analysis shows increased uptake of NB in KID-KCs (f). All data are presented as the mean ± SEM. *$p < 0.05$; ***$p < 0.001$. Bar = 200 μm.

Figure 3. Epidermal morphology of grafted skin in human-murine chimeric skin graft model

Primary fibroblasts and immortalized keratinocytes derived from the KID syndrome patient harboring heterozygous *GJB2* c.148G>A mutation or a healthy donor were used to generate bio-engineered skin sheets, which were grafted onto NOD-severe combined immunodeficiency mice (NSG mice). Eight weeks post-grafting, regenerated skin grafts were harvested. Macroscopic examination showed fine, dry scales in the graft generated from patient cells (d) compared to that generated from control cells (a). Histological examination showed hyperkeratosis and spongiosis in the patient skin graft (f), resembling that seen in the patient skin (c). The skin architecture of the control skin graft (e) was also similar to healthy donor skin (b). Bar = 100 μM.

Figure 4. Allele-specific GJB2 knockdown by S7

The mRNA expression of total *GJB2*, wildtype (WT) and the mutant (MUT) *GJB2* alleles in control-KCs (Control) and KID-KC (KID) treated with AS-siRNA S7 was examined by qRT-PCR and compared to untreated cells (UT) (a). Total Cx26 protein expression in S7-treated cells from three independent immunoprecipitation(IP)/immunoblotting(IB) experiments (b). The expression was quantified using densitometry (c). β-actin was used as a loading control and HeLa cells were

used as a negative control. A reduction in total Cx26 expression was detected in KID-KCs after S7 treatment, but such a change was not detected in control-KCs. N.S, not significant; **$p < 0.01$

Figure 5. S7 treatment corrected abnormal gap junction and hemichannel functions in KID-KCs

SLDT was performed in siRNA-treated KID-KCs (KID) and control-KCs (Cont) to assess GJ activity (a, b). The analysis of neurobiotin transfer (red) is shown (c, d). Each dot in panels c and d represents the average neurobiotin transfer from a single image. Three independent experiments were carried out and at least ten images were analyzed from each experiment. Restoration of GJ activity was detected in KID-KCs following S7 treatment. Whole-cell patch clamp (e-h) and neurobiotin uptake (i, j) were carried out to examine hemichannel activity. Records of currents from single cells under the voltage step protocol (e) are shown (f, g). The plot of current density against membrane voltage shows correction of hyperactive hemichannels in KID-KCs after S7 treatment (h). Representative neurobiotin (NB, red) uptake images are shown in (i). The nuclei were stained with DAPI (blue). Data analysis shows reversal of aberrantly enhanced NB uptake in KID-KCs (j). Data are presented as the mean ± SEM. N.S, not significant; *$p < 0.05$; **$p < 0.01$; ***$p < 0.001$. Bar = 200 μm.

Supplementary Materials

Supplementary Methods

Immunostaining

Frozen tissue sections (6 μm) or paraformaldehyde-fixed cultured cells were incubated in PBS containing 3% fetal bovine serum and 0.3% Triton X-100 for 20 min at room temperature, and then incubated overnight at 4°C with a monoclonal Cx26 antibody (1:50; Thermo Fisher Scientific; Cat. #13-8100). Following several rinses with PBS, samples were incubated with a biotinylated secondary antibody (1:100; Vector Laboratories, Peterborough, UK) for 1 hr prior to visualization using an Alexa-Fluor 488- or 568-conjugated streptavidin (1:500; Invitrogen, Paisley, UK). Samples were counterstained with 5 μg/ml 4,6-diamino-2-phenylindole (DAPI, Vector Laboratories, Peterborough, UK), mounted using 10% Mowiol (Calbiochem, Nottingham, UK), and imaged using a Zeiss LSM 510 laser confocal microscope (Zeiss, Oberkochen, Germany). Images were recorded under the same settings (laser power, digital offset and gain) from three to seven continuous, non-overlapping fields on each slide, and analyzed using ImageJ v1.51n (NIH, Bethesda, MD, USA).

siRNAs

Nineteen candidate AS-siRNAs (S1−S19) were designed and synthesized (Sigma, Dorset, UK). In siRNA screening experiments, the Silencer™ siRNA against GFP (Thermo Fisher Scientific, Paisley, UK) was used as a positive control (i.e. indicator of transfection and knockdown efficiency) and the siRNA against human *HAS2* was used as a negative control (si-cont, Sigma, Dorset, UK).

The sequences of si-cont are: sense 5'-AUAUCGUCAUGGUCUUCAU[dT][dT]-3', and antisense 5'-AUGAAGACCAUGACGAUAU [dT][dT]-3'.

Screening of AS-siRNAs

A fluorescence-based screening system was generated using HeLa cells stably expressing ectopic *GJB2-WT* or *GJB2-c.148G>A* which was fused to *GFP* cDNA at the 3'-terminus, driven by the cytomegalovirus promoter (*CMV*) **(Supplementary Figure S4)**. We used the HIV-1 derived, self-inactivating lentiviral vector pLNT-SFFV-MCS, with the WT or mutant *CMV-GJB2-GFP* cDNA sequence subcloned in. Lentiviruses were packaged by co-transfecting HEK-293T cells with the WT or mutant lentiviral vector, together with a plasmid encoding the vesicular stomatitis virus envelope and a packaging plasmid pCMV8.74 coding for lentiviral *gag*, *pol* and accessory proteins, *tat* and *rev*. Infectious viruses were harvested 72 hrs post-transfection, filtered through a 0.45-μm pore cellulose acetate filter, and then ultra-centrifuged at 23,000 × g for 2 hrs. Concentrated viruses were resuspended in the Opti-MEM® medium and the lentivirus stocks were kept at -80°C until use. The viral titres assessed by GFP expression using flow cytometry were 8.8×10^7 infectious unit (IU)/ml for WT viruses and 4.9×10^6 IU/ml for mutant viruses. HeLa cells were transduced with either WT or mutant lentiviruses and, upon confluence being reached, fluorescence-activated cell sorting was carried out to obtain single GFP^+ cells using a Moflo XDP flow cytometer (Beckman Coulter, Luton, UK). These single cells were cultured until clonal expansion was observed.

GFP^+ clonal HeLa cells were seeded in a 24-well plate and, upon reaching a 70% confluence, were transiently transfected with each AS-siRNA at a concentration of 50 nM, using Lipofectamine™ RNAiMAX (Thermo Fisher Scientific, Paisley, UK). 24 hrs post-transfection, the level of *GJB2-GFP* expression was assessed using flow cytometry (FACSCalibur™, BD Biosciences, Oxon, UK).

Briefly, a non-fixed cell suspension was prepared in PBS containing 2% fetal bovine serum. 10,000 cells from each sample were acquired using the FL1 channel with a 530-nm emission filter. Data were analyzed using the FlowJo software v10 (Tree Star Inc., Oregon, USA) and knockdown efficiency was indicated by the decrease of mean GFP intensity (I) in transfected cells, calculated as: $[1- (I_{\text{allele-specific siRNA}} / I_{\text{control siRNA}})] \times 100\%$.

Quantitative reverse transcriptase-PCR (qRT-PCR)

Total RNA was extracted from cells using TRIzol® reagent (Thermo Fisher Scientific, Paisley, UK). Complementary DNAs (cDNAs) were generated using the GeneAmp® RNA PCR Core Kit (Applied Biosystems, Warrington, UK). qRT-PCR was carried out using iTaq™ universal SYBR Green Supermix (Bio-Rad, Watford, UK). All primers used (including the c.148G>A allele-specific primers) are listed in **Supplementary Table S1**. The reactions were performed in triplicate on a C1000™ Thermal Cycler (Bio-Rad, Watford, UK) with conditions as follows: initial denaturation at 95°C for 1 min, followed by 39 thermocycles of 95°C for 15 s and 60°C for 30 s. Individual levels were normalized to *GAPDH* expression. qRT-PCR data were collected and analyzed using CFX-3.1 (Bio-Rad, Watford, UK) and relative expression of *GJB2* was calculated using the $2^{-\Delta\Delta Ct}$ method.

Immunoprecipitation and immunoblotting

Cells were cultured in a 100-mm dish to confluence, washed twice in PBS, and lysed using an immunoprecipitation (IP) lysis buffer containing 10 mM Tris-HCl (pH 7.4), 150 mM NaCl, 1% Triton X-100, 0.5% NP-40, 1 mM EDTA, 1 mM EGTA, 1 mM PMSF supplemented with protease inhibitor cocktail. The lysates were incubated on ice for 15 min with occasional vortexing, and then

centrifuged at 12,000 × g at 4°C for 10 min. 1−1.5 mg protein from the supernatant was transferred to a fresh tube. 0.75 μg of a polyclonal Cx26 antibody (Thermo Fisher Scientific, Paisley, UK, Cat. #71-0500) was added to the lysate and incubated at 4°C for 2.5 hrs. Protein G-Sepharose beads (GE Healthcare, Buckinghamshire, UK) of a 50% slurry was added to the lysate and mixed overnight at 4°C. The beads were harvested by brief centrifugation and washed in IP lysis buffer without detergent. The final pellet was resuspended with a sample buffer containing 125 mM Tris-HCl (pH 6.8), 5% β-mercaptoethanol, 4% sodium dodecyl sulfate (SDS), 10% glycerol and 0.0004% bromophenol blue, and boiled at 95°C for 10 min with brief vortexing to dissociate antigen-antibody complexes from the beads. Samples were briefly centrifuged, and supernatants were analyzed immediately by immunoblotting (IB). The supernatant samples were separately by standard 12% SDS-PAGE in the NuPAGE™ MES SDS running buffer (Thermo Fisher Scientific, Paisley, UK). Membranes were blocked in 5% skimmed milk in PBS and then probed with a monoclonal Cx26 antibody at 1:1000 dilution (Merck Millipore, Watford, UK, Cat. #MABT198). An anti-mouse HRP-conjugated secondary antibody at 1:4000 dilution (GE Healthcare, Buckinghamshire, UK) was used. The target protein was detected using the ECL™ Prime Western Blotting Detection system (Amersham, Buckinghamshire UK). Densitometric analysis was performed on scanned images of blots.

Patch clamp for hemichannel activity

Whole-cell patch clamp was carried out at room temperature as previously described (Levit et al., 2015). Cells were seeded onto 12-mm glass coverslips, which were later transferred to an experimental chamber filled with Tyrode's bath solution containing (in mM): NaCl 137.7, KCl 5.4, NaOH 2.3, $MgCl_2$ 1, glucose 10, and HEPES 5 (pH 7.4). Patch pipettes were pulled from glass

capillaries to a resistance of 3 ─ 6 MΩ with a horizontal puller (P-87, Sutter Instruments, Novato, CA). Pipettes were filled with a solution containing (in mM): K-aspartate 120, HEPES 5, ethylene glycol tetraacetic acid 10, and NaATP 3 (pH 7.2). Solitary cells were measured for membrane capacitance (C_m) and membrane currents (I_m) invoked while the membrane potential was stepped from -110 mV to +110 mV in 20 mV increments. Voltage and current signals were recorded using an Axopatch-1D patch clamp amplifier coupled to a Digidata 1322A interface (Axon Instruments, Foster City, CA). Data were acquired and analyzed using Clampex 9.2 and Clampfit 10.2 software (Axon instruments), respectively. To control for variability in size of recorded cells, membrane current density (I_m/C_m) was used as a direct measure of hemichannel activity. Comparison was made between current density at individual membrane voltages.

Neurobiotin uptake assay for hemichannel activity

The method was modified from a protocol described previously (Mese et al., 2011). Cells plated at a low density were gently washed twice with Ca^{2+}, Mg^{2+}-containing Hank's balanced salt solution (HBSS, Thermo Fisher Scientific, Paisley, UK), and then incubated in 0.1 mg/ml neurobiotin (Vector Laboratories, Peterborough, UK), a non-fluorescent tracer, in divalent-free HBSS at 37°C for 10 min to allow uptake of neurobiotin through open hemichannels. After two washes in Ca^{2+}, Mg^{2+}-containing HBSS, cells were fixed with 4% paraformaldehyde in PBS at 4°C, permeabilized with 0.3% Triton X-100 (Sigma, Dorset, UK) and then stained with Alexa Fluor 568-streptavidin conjugate at 1:400 dilution (Thermo Fisher Scientific, Paisley, UK) at room temperature. Labelled samples were imaged using an Olympus IX71 inverted fluorescence microscope (Olympus, Essex, UK) with the same exposure time applied to all samples. Five to ten neurobiotin uptake images

from each group were recorded and analyzed using ImageJ v1.51n (NIH, Bethesda, MD, USA), and hemichannel activity was determined by the intensity of intracellular neurobiotin.

SLDT assay for gap junction intercellular communication

The scrape loading dye transfer assay (SLDT) was performed as described previously with minor modifications (Yum et al., 2007). Confluent monolayer cell cultures (24- or 48 hrs post-seeding) were gently rinsed twice with Ca^{2+}, Mg^{2+}-containing HBSS, and then replaced with divalent-free HBSS containing 0.1 mg/ml neurobiotin. Multiple parallel scrape lines were made on the cultures using a sharp scalpel blade, followed by incubation at 37°C for 10 min. Cells were washed twice with Ca^{2+}, Mg^{2+}-containing HBSS, fixed with 4% paraformaldehyde in PBS, and stained as described in the neurobiotin uptake assay section. Stained samples were imaged using an Olympus IX71 inverted fluorescence microscope. At least six scrape-wounded images and three background (non-scrape-wounded) images were recorded from each group. Images were analyzed using ImageJ v1.51n. GJ intercellular communication was determined by the extent of dye transfer, quantified by the total area between the scrape line and the point at which the fluorescence level reduced to 1.5 × the background fluorescence level.

Bio-engineered skin and human-murine chimeric skin graft model

The methods for preparing and grafting bioengineered skin in immunodeficient mice have been described previously (Di et al., 2011). In brief, immortalized KID-KCs at passage 7 were seeded on top of a fibrin matrix populated with live primary fibroblasts (passage 3) isolated from the KID syndrome patient. After keratinocytes reached confluence, the bio-engineered skin constructs were grafted onto the dorsum of 22-week-old NOD-severe combined immunodeficiency mice (NOD scid

gamma [or NSG] mice, Charles River, UK). Three months post-grafting, mice were anesthetized and skin samples from graft area were taken post-mortem, embedded in paraffin and sectioned for histological examination.

RNA sequencing (RNA-Seq) and data analysis

Cultured KID-KCs treated in triplicate with AS-siRNA were subject to RNA-Seq experiments 24 hrs post-treatment and untreated cells were used as a control. RNA was extracted using TRIzol® reagent (Thermo Fisher Scientific, Paisley, UK) and RNA quality was measured using an Agilent Bioanalyser. All samples had an RNA integrity number greater than 9.8. cDNA libraries were prepared using the KAPA mRNA HyperPrep Kit (KAPA Biosystems) according to manufacturers' instructions. The libraries were sequenced with a 43-bp paired-end run using a NextSeq 500 instrument (Illumina, San Diego, US). The sequence reads are available at GEO accession GSE131709.

Data were first demultiplexed and converted to fastq files using bcl2fastq Conversion (v2.19, Illumina). Fastq files were then pre-processed to remove adapter contamination and poor-quality base calls (Q20 or below) using a 5' to 3' sliding window approach. The remaining read data were mapped to the hg38 reference genome using the gapped aligner, RNA-STAR (v2.5b). Read data were counted per transcript by FeatureCounts (v1.4.6p5). Normalization, modelling and differential expression analysis were carried out using the SARTools package (v1.3.2, BioConductor). All reference genomes and annotation were obtained from the Illumina iGenomes repository. Differentially expressed genes were determined using a threshold of p-adj < 0.05 and $|\log_2$ fold change$| \geq 1$ (Speranza et al., 2017).

Supplementary Tables

Supplementary Table S1. Primers

Target	Forward primers (5'-3')	Reverse primers (5'-3')
Total *GJB2*	CTCCCGACGCAGAGCAAA	GGTTGCCTCATCCCTCTCAT
GJB2 WT	CTCCCGACGCAGAGCAAA	GGCTGCAGGGTGTTGCAGACAATGTC
GJB2 mutant	CTCCCGACGCAGAGCAAA	GGCTGCAGGGTGTTGCAGACAATGTT
GAPDH	CCCATCACCATCTTCCAGGA	CCAGTGAGCTTCCCGTTCAGC
MMP1	AAAGGGAATAAGTACTGGGC	CAGTGTTTTCCTCAGAAAGAG
MMP9	AGCTGGCAGAGGAATAC	CCCCAGAGATTTCGACTC
MMP10	ACCAATTTATTCCTCGTTGC	GTCCGTAGAGAGACTGAATG
ANGPTL4	AGGCAGAGTGGACTATTTG	CCTCCATCTGAGGTCATC
CXCL5	ATTTGTCTTGATCCAGAAGC	TCAGTTTTCCTTGTTTCCAC
TMEM109	CTTATCCTCCTCCACTCAG	GACGAAGACTCTGACACC
GPR137	AACCTCTACTTTGCCCAG	GTTCACCAGCAGAAAGAG
AFAP1L1	GGAATGGGAAATGAAGAAGAC	CATATCCCCTAAAATCATGCAG
NSA2	GTAAAGAAGAATCCCTCATCC	GGTAACCTCCCCATATTTTC
GLB1L2	ACTTCAGAATCTATAGCCTGG	CAAGCTACCCAAGAAGAAAG

Supplementary Table S2. List of 180 genes predicted to have seed sequence match with S7

ABCA1	*CRB2*	*IFT88*	*MED13L*	*PLXNB1*	*SLC6A8*
ABCC3	*CREBBP*	*IGF2R*	*MED17*	*PPP4R1*	*SMCR7*
ADAMTS7	*CSPG4*	*IGSF9B*	*MEGF8*	*PPRC1*	*SON*
ADCK4	*CTNNA1*	*INTS10*	*MST1R*	*PRKCQ*	*SPEN*
ADCY1	*CUL9*	*IQGAP3*	*MTF2*	*PRR14L*	*STRBP*
ADCY10	*CYP2S1*	*KANSL2*	*MYO16*	*PRSS21*	*SVIL*
ADH4	*DAGLA*	*KANSL3*	*NAT10*	*PRX*	*SYNE2*
AFP	*DMBT1*	*KAT5*	*NAV3*	*PSD3*	*SZT2*
AGBL1	*DSG2*	*KCNH4*	*NBEAL2*	*PTPRB*	*TAF1*
ANKRD28	*DTNA*	*KCNH5*	*NCOA1*	*RAB11FIP5*	*TAF5L*
APOB	*DZANK1*	*KCNK16*	*NEURL4*	*REG1A*	*TBCD*
ARHGAP44	*EDC4*	*KDR*	*NLRC5*	*RINT1*	*TEK*
ASH1L	*ERN1*	*KIAA0556*	*NLRP8*	*RNF17*	*TENM1*
ATP13A1	*ESPL1*	*KIAA1671*	*NOD1*	*RREB1*	*TENM4*
BCAN	*FBXW2*	*KIAA1755*	*NOS2*	*RTTN*	*TEP1*
BIRC6	*FCGBP*	*KIDINS220*	*OCA2*	*RYR3*	*TLE2*
BPIFB4	*FLT1*	*KNTC1*	*OR51E1*	*SCN2A*	*TLR8*
C12orf55	*FOCAD*	*LAMA1*	*PCDH19*	*SCN3A*	*TMPRSS4*
C12orf63	*FRAS1*	*LAP3*	*PCDHB13*	*SEC23A*	*TRAK2*
C16orf62	*GALNT8*	*LIM2*	*PCDHB16*	*SEC31B*	*TRIM60*
C5	*GJA10*	*LLGL2*	*PCDHGA6*	*SEMA4A*	*TTC3*
C6orf132	*GNRHR*	*LOC101929274*	*PCNXL3*	*SLC12A1*	*TUBGCP6*
CACNA1B	*GPR112*	*LOC400499*	*PI4KA*	*SLC26A6*	*UNC13A*
CAND2	***GPR137***	*LRP1B*	*PIGV*	*SLC30A5*	*URB1*
CDS2	*GRM3*	*LTBP4*	*PIWIL2*	*SLC35B1*	*UTRN*
CNOT1	*GRM8*	*LTN1*	*PKD1*	*SLC37A2*	*VPS13D*
COL15A1	*GSG2*	*LY75*	*PKHD1*	*SLC44A3*	*VWF*
COL20A1	*GTPBP2*	*LY75-CD302*	*PLCB3*	*SLC45A3*	*WNK2*
COL4A2	*HLCS*	*MAGEL2*	*PLEKHG2*	*SLC4A4*	*WRN*
COPA	*HLTF*	*MAP7*	*PLEKHM2*	*SLC5A9*	*ZSWIM8*

*Among the 180 genes, only *GPR137* (underlined, bolded) was found in the top five up- or downregulated genes in KID-KCs treated by S7

Supplementary Figures

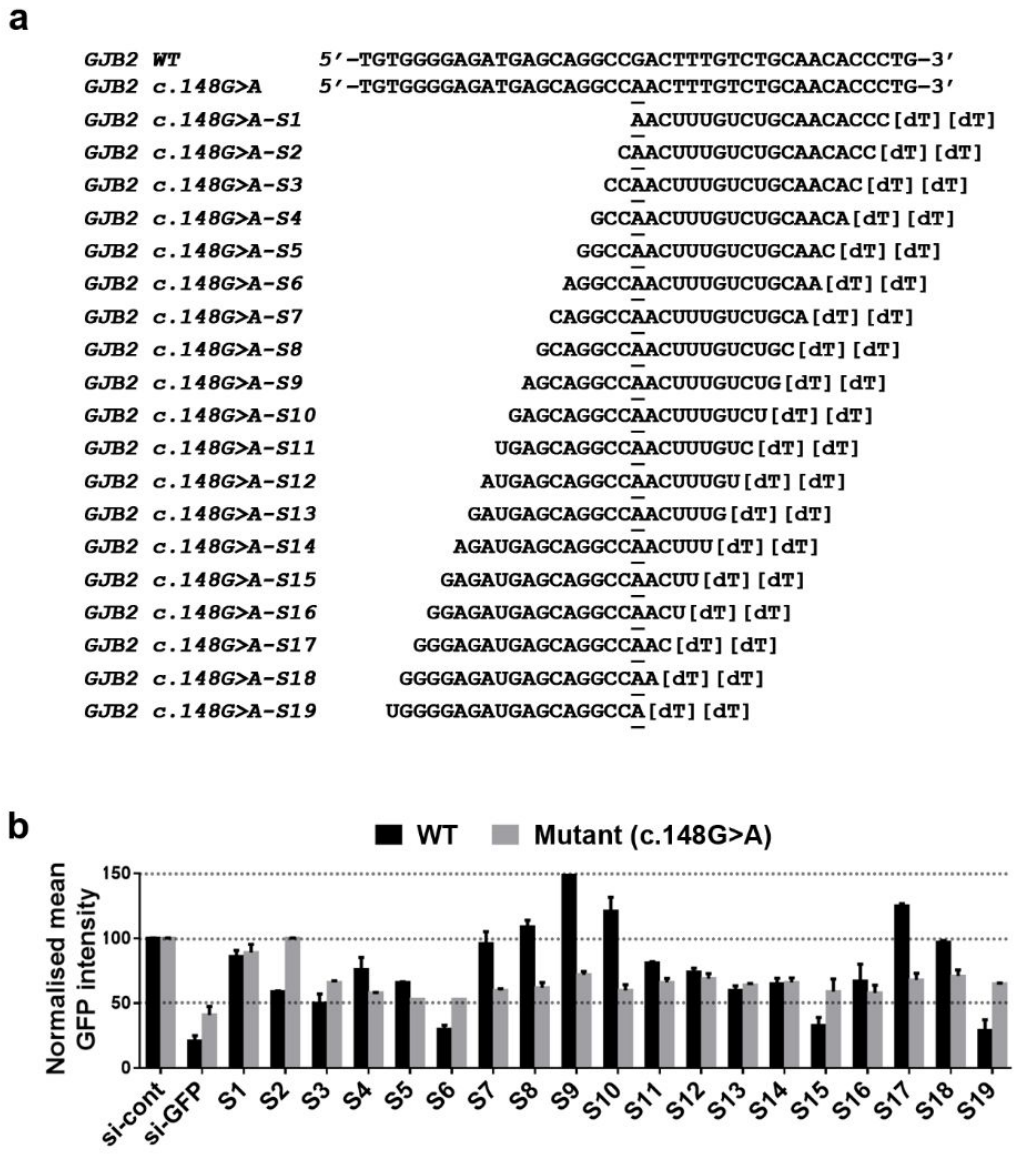

Supplementary Figure S1. AS-siRNAs: design and screening

19 AS-siRNAs (with a 19-nt targeting sequence plus a deoxythymidine dinucleotide) were designed and designated *GJB2* c.148G>A_S1−S19 (or S1−S19 in short form). WT and mutant *GJB2* sequences are shown and aligned with the siRNAs, with c.148G>A mutation underlined (a). Fluorescence-based screening results of the 19 AS-siRNAs in HeLa cells expressing WT or mutant

GJB2-GFP fusion transgene are shown (b). The GFP siRNA (si-GFP) and the irrelevant siRNA (si-cont) were used as positive and negative controls, respectively. The *GJB2* knockdown efficiency of the AS-siRNAs was determined by the decrease in GFP intensity detected by flow cytometry (n = 3). The lead AS-siRNA, S7, inhibited the mutant *GJB2* potently and specifically, but did not inhibit the WT *GJB2*. Data are normalized to the levels from cells treated with si-cont and shown as mean ± SEM.

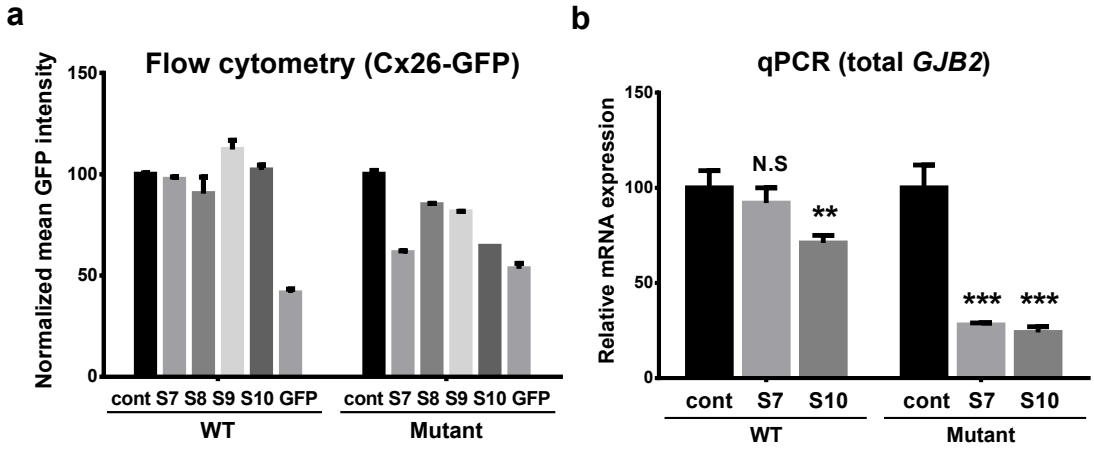

Supplementary Figure S2. Validation of AS-siRNA screening suggested potent and mutation-specific inhibitory activity of S7

HeLa cells treated with 50 nM AS-siRNA (S7-S10), si-cont (cont), or si-GFP (GFP) were examined for Cx26-GFP protein expression using flow cytometry (a) and for total *GJB2* mRNA using qRT-PCR (b). Mutant-specific inhibition was achieved by S7 and S10 (a). These two siRNAs were further tested at mRNA level and non-specific inhibition of wildtype (WT) *GJB2* was detected in cells treated with S10, but not in those treated with S7 (b). N.S, not significant; $^{**}p < 0.01$; $^{*}p < 0.001$.

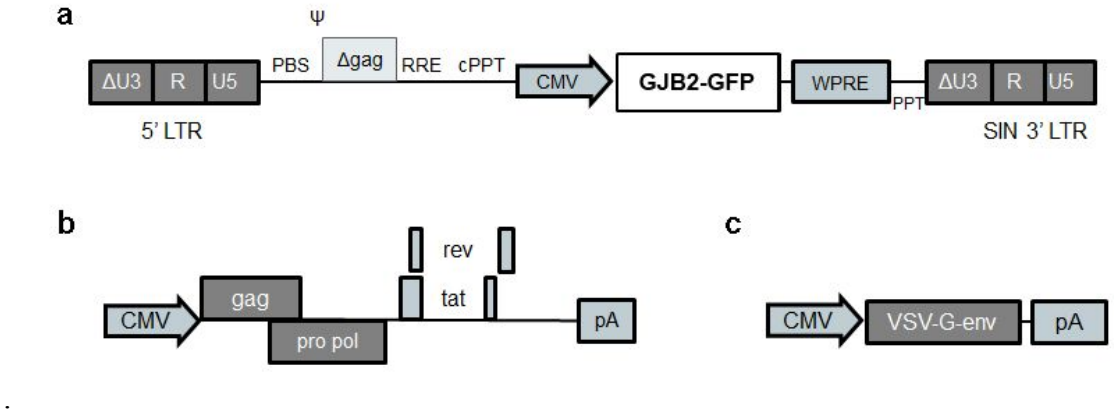

Supplementary Figure S3. Schematic of the LNT-*CMV-GJB2-GFP* lentiviral vectors

Panel a shows the self-inactivating, HIV-1-based vector with the transgene cloned in, which encodes the wildtype or c.148G>A mutant *GJB2* cDNA fused to *GFP* reporter cDNA at the 3' terminus driven by the cytomegalovirus promoter (*CMV*). Panel b shows the packaging plasmid containing *gag*, *pol*, *rev* and *tat* genes and panel c shows the envelope plasmid. LTR, long terminal repeat. PBS, tRNA primer binding site. RRE, rev response elements. VSV-G env, envelope pseudotyped with the G glycoprotein of vesicular stomatitis virus. cPPT, central polypurine tract. WPRE, woodchuck hepatitis virus post-transcriptional regulatory element.

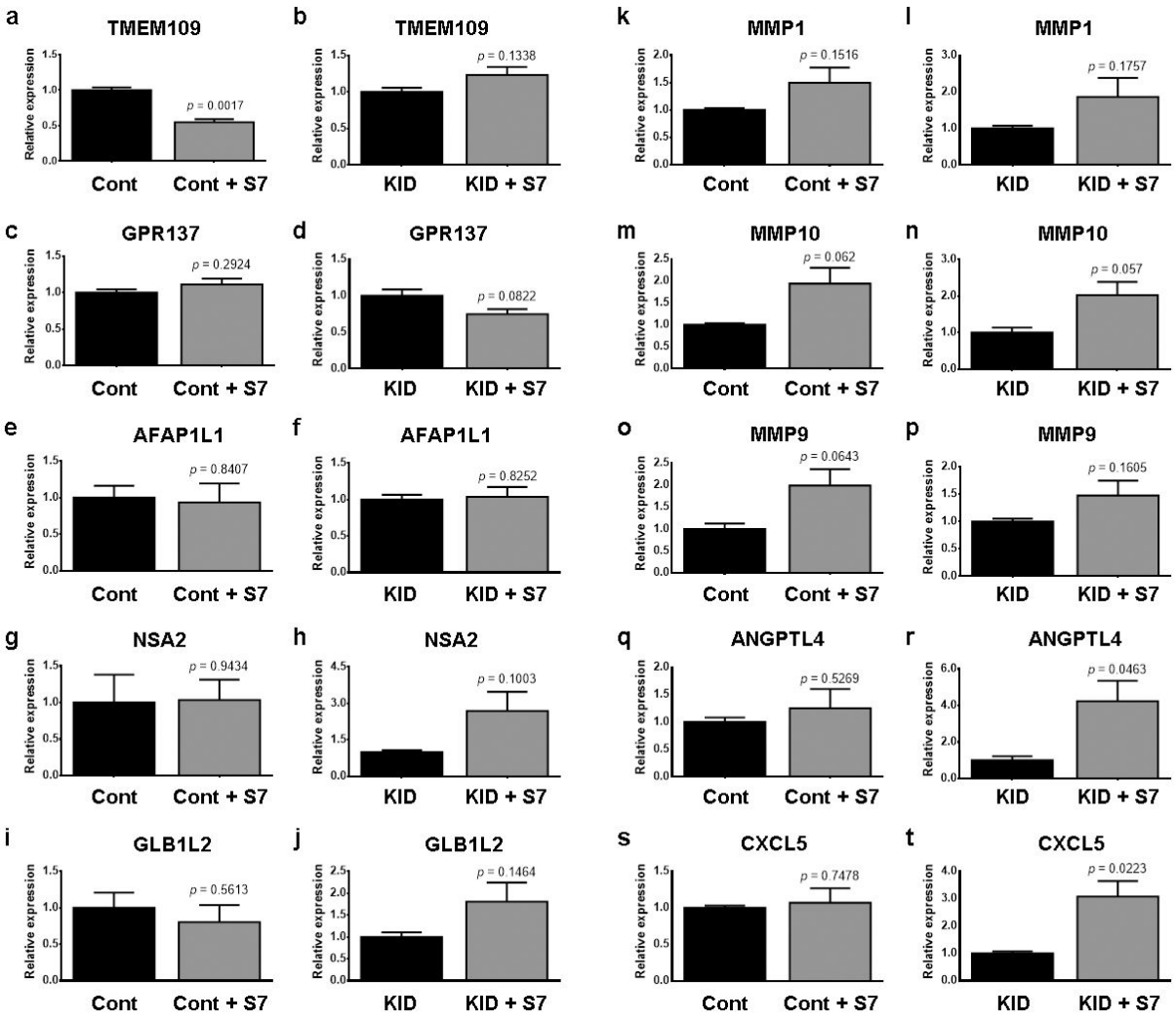

Supplementary Figure S4. Validation of the RNA-Seq data using qRT-PCR

RNA extracted from Control-KCs (Cont) and KID-KCs (KID) with or without treated S7 treatment were subjected to qRT-PCR using primers specific to the top 5 upregulated and 5 downregulated genes from the RNA-Seq analysis. The expression levels were calibrated by the internal control *GAPDH* gene. Data are represented as mean ± SEM and analyzed statistically using Student's *t*-test (n = 3).

REFERENCES

Di WL, Larcher F, Semenova E, Talbot GE, Harper JI, Del Rio M, et al. Ex-vivo gene therapy restores LEKTI activity and corrects the architecture of Netherton syndrome-derived skin grafts. Mol Ther 2011; 19: 408-16.

Levit NA, Sellitto C, Wang HZ, Li L, Srinivas M, Brink PR, et al. Aberrant connexin26 hemichannels underlying keratitis-ichthyosis-deafness syndrome are potently inhibited by mefloquine. J Invest Dermatol 2015; 135: 1033-42.

Mese G, Sellitto C, Li L, Wang HZ, Valiunas V, Richard G, et al. The Cx26-G45E mutation displays increased hemichannel activity in a mouse model of the lethal form of keratitis-ichthyosis-deafness syndrome. Mol Biol Cell 2011; 22: 4776-86.

Speranza E, Altamura LA, Kulcsar K, Bixler SL, Rossi CA, Schoepp RJ, et al. Comparison of transcriptomic platforms for analysis of whole blood from Ebola-infected cynomolgus macaques. Sci Rep 2017; 7: 14756.

Yum SW, Zhang J, Valiunas V, Kanaporis G, Brink PR, White TW. Human connexin26 and connexin30 form functional heteromeric and heterotypic channels. Am J Physiol Cell Physiol 2007; 293: C1032-48.

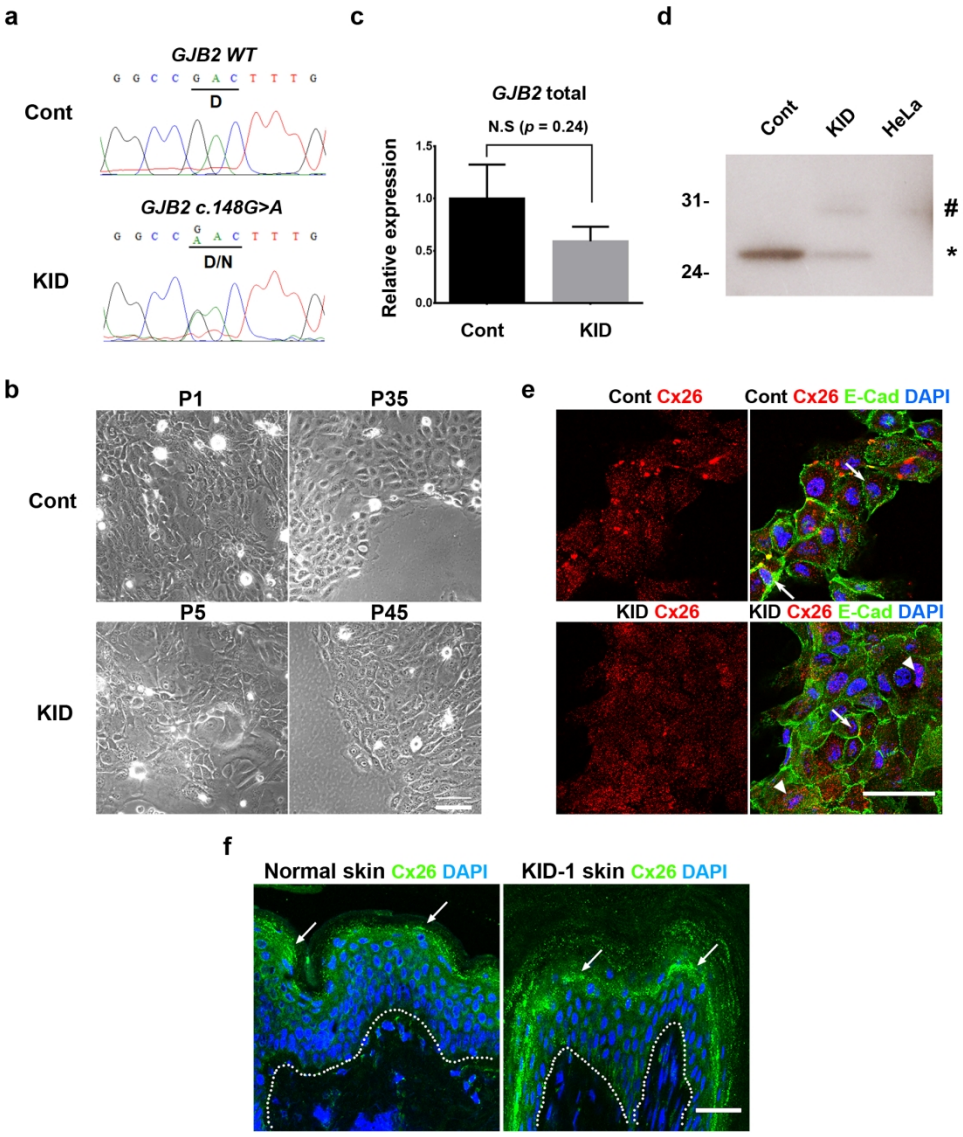

Genotype, morphology, GJB2 expression and subcellular localization in keratinocytes

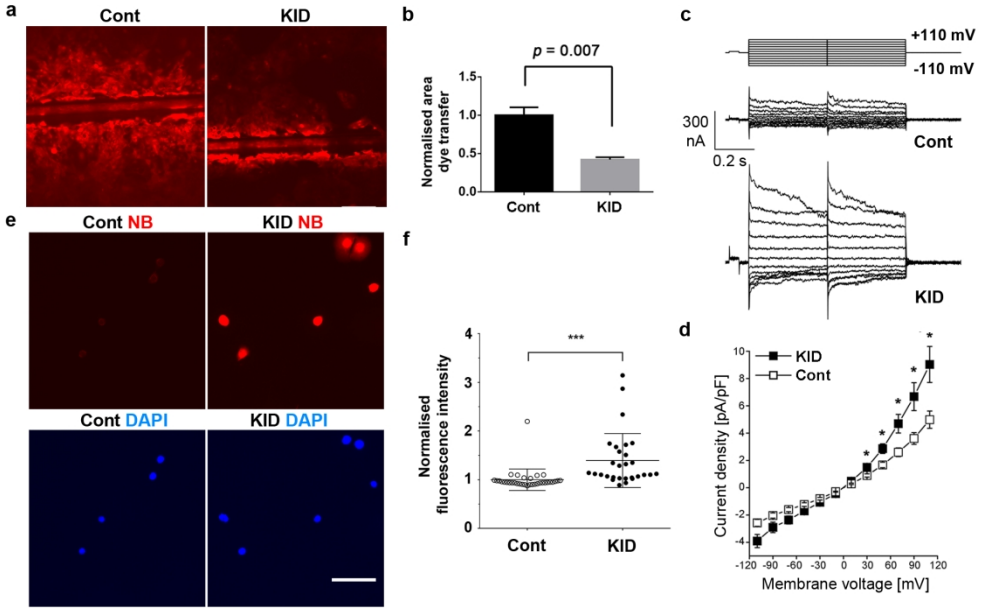

Abnormal gap junction and hemichannel behavior in KID-KCs

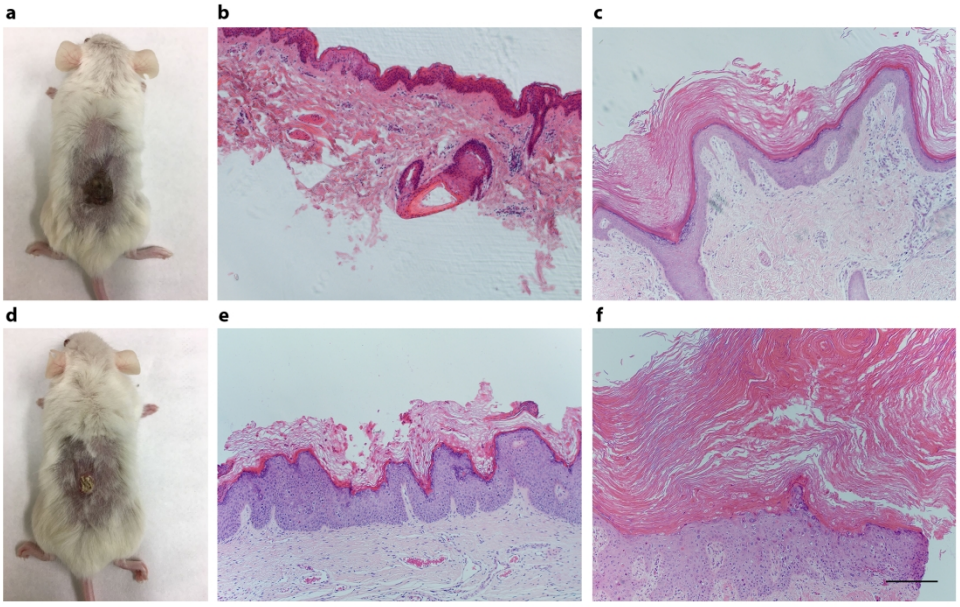

Epidermal morphology of grafted skin in human-murine chimeric skin graft model

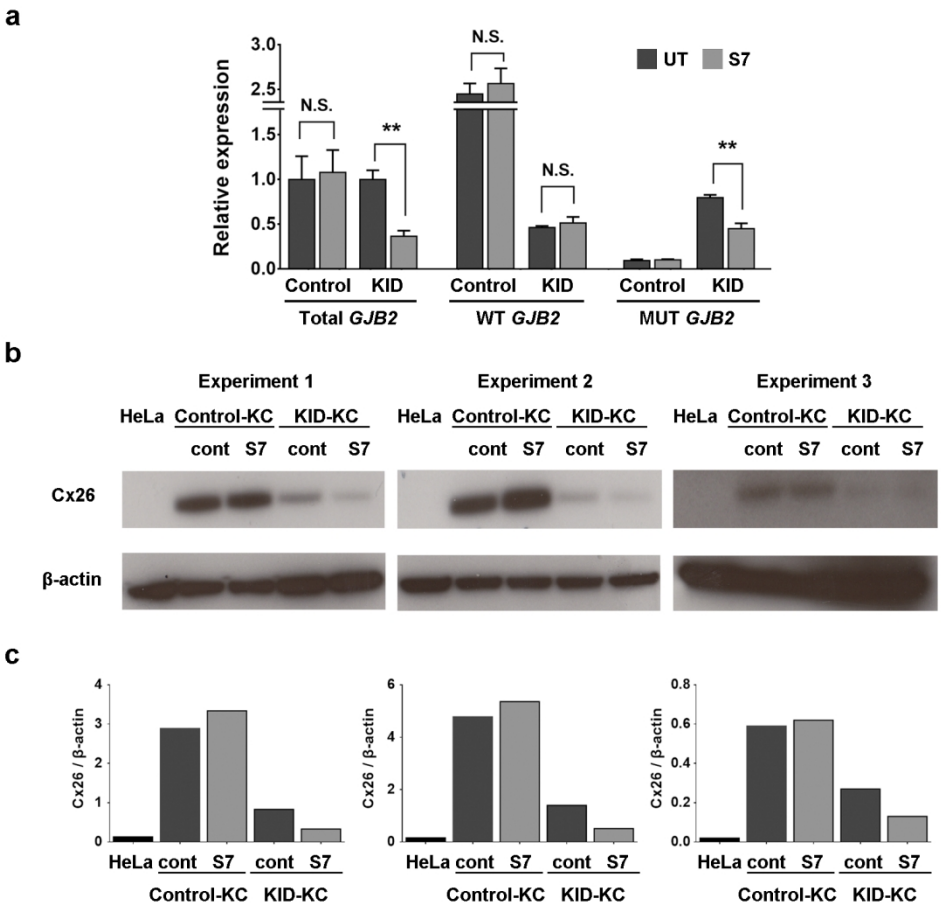

Allele-specific GJB2 knockdown by S7

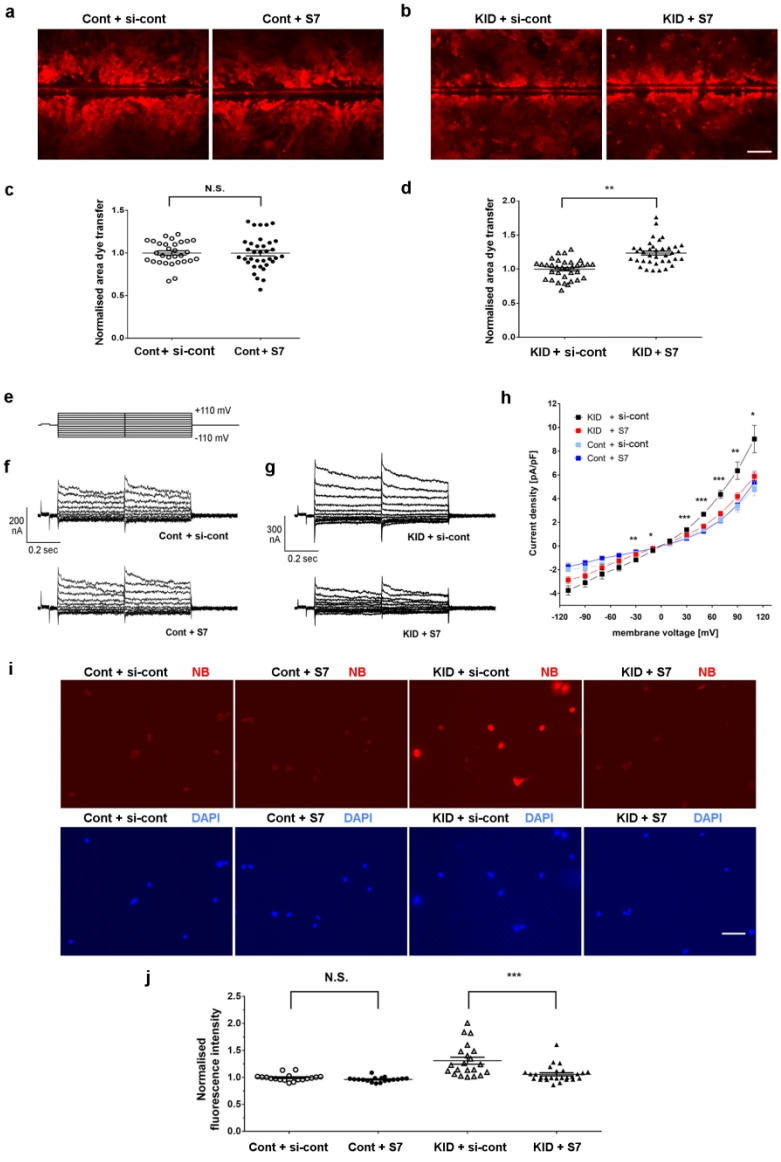

S7 treatment corrected abnormal gap junction and hemichannel functions in KID-KCs